

**DESIGN AND CONTROL OF AN
AUTONOMOUS SPIDER-LIKE ROBOT
FOR MOTION IN 2D TUNNELS
ENVIRONMENTS**

AMIR SHAPIRO

**DESIGN AND CONTROL OF AN
AUTONOMOUS SPIDER-LIKE ROBOT FOR
MOTION IN 2D TUNNELS ENVIRONMENTS**

RESEARCH THESIS

SUBMITTED IN PARTIAL FULFILLMENT OF THE
REQUIREMENTS
FOR THE DEGREE OF DOCTOR OF PHILOSOPHY

AMIR SHAPIRO

SUBMITTED TO THE SENATE OF THE TECHNION — ISRAEL INSTITUTE OF TECHNOLOGY

TISHREI, 5764

HAIFA

OCTOBER, 2003

THIS RESEARCH THESIS WAS SUPERVISED BY PROFESSOR ELON RIMON
UNDER THE AUSPICES OF THE MECHANICAL ENGINEERING
DEPARTMENT

ACKNOWLEDGMENT

I would like to express my sincere gratitude to Professor Elon Rimon for his support and dedicated guidance during this research.

I wish to express gratitude to Dr. Shraga Shoval for the great help and many good advices in developing the spider-robot prototype and conducting experiments. I would like to thank Yizhar Or for many fruitful discussions. Thanks to Zeev Hershkowitz who manufactured and assembeled the spider-robot parts in the Energy building workshop. Thanks to the workers in the manufacturing and robotics building workshop who manufactured the grasping arrangement for the grasping experiments.

Finally, I wish to thank my beloved family my parents David and Sylvie, my wife Haya and my three sons Elad Avihay and Uriel for their support and encouragement along the way.

THE GENEROUS FINANCIAL HELP OF THE TECHNION AND THE SALIM
AND RACHEL BENIN FOUNDATION IS GRATEFULLY ACKNOWLEDGED

Dedicated to my parents David and Sylvie Shapiro, to my wife Haya
and to my sons Elad Avihay and Uriel.

Contents

Abstract	1
List of Symbols	2
1 Introduction	7
1.1 Summary of Contributions	11
2 Force Closure Set	14
2.1 Introduction	14
2.2 Geometric Definition of Force Closure Grasps	16
2.2.1 Frictional Grasps Terminology	17
2.2.2 Review of Active Force Closure	18
2.2.3 Force Closure with Compliant Contacts	19
2.3 The Force Closure Set of Compliant Grasps	22
2.3.1 Characterization of The Force Closure Set	22
2.3.2 The Force Closure Set Under Linear Compliance Law	26
2.4 Global Stability Analysis	27
2.4.1 The Grasped Object Equilibria	27
2.4.2 Stability Characterization	29

2.4.3	Convergence Point Algorithm	38
2.5	Force Closure Set for Curved Fingers	39
2.5.1	Problem Statement and Mathematical Representation	40
2.5.2	Initial Equilibrium Point with Rolling	44
2.5.3	Rolling Stability of Equilibrium Point	46
2.6	Simulations and Experimental Results	49
2.6.1	Experiments Setup	49
2.6.2	Verifying the Force Closure Stability Set Experiment	50
2.6.3	The Effect of Preloading Forces on Stability	55
2.7	Conclusion	58
3	PCG: A Foothold Selection Algorithm	60
3.1	Introduction	60
3.2	The Feasible 3-Limb Postures	65
3.3	Convexity of the Feasible 3-Limb Postures	70
3.3.1	Convexity of the Feasible Postures	70
3.3.2	Convexity of the Cube Approximation Problem	72
3.4	The PCG Algorithm	75
3.5	Selection Number of Maximal Cubes	83
3.5.1	Connectivity Between Convex Sets	83
3.5.2	Selection of the Maximal Cubes Relative Configuration	84
3.5.3	An Algorithm to Oracle Number of Maximal Cubes	85
3.6	Simulation Results	86
3.6.1	Simulation of the PCG Algorithm	88
3.6.2	The Effect of Number of Maximal Cubes on Path Length	93

3.7	Conclusion	95
4	Control of Spider-Like Robot	98
4.1	Introduction	98
4.2	Compliant Contact Model	100
4.2.1	The Contact Stiffness Matrix	103
4.3	Control Law	107
4.3.1	The Dynamics of k -Limbed Spider Robot	107
4.3.2	The Control Law	109
4.3.3	Equilibrium Point of the Spider-Robot System	110
4.3.4	Linearization of Spider-Robot System About Equilibrium	113
4.4	Stability Analysis	114
4.4.1	Stability of 2^{nd} -Order Asymmetric Linear Systems	114
4.4.2	Equilibrium Stability of k -Limbed Spider-Robot	119
4.5	Conclusion	125
5	Experimental Results	127
5.1	Experiments Setup	127
5.2	Experimental Results	129
6	Conclusion	136
A	Additions for Force Closure Grasps	139
A.1	Conditions for Force Closure with Compliant Contacts	139
A.2	Computation of the Grasp Stiffness Matrix	140
B	Details of the PCG Algorithm	143

CONTENTS

vii

References

144

Hebrew Abstract

5

List of Figures

1.1	Two generations of a planar spider-robots. (a) 4-limb spider-robot capable of moving in frictionless tunnel environments, and (b) 3-limb spider robot capable of moving in frictional tunnel environments. . . .	9
2.1	(a) A multi-fingered hand grasping an object. (b) A multi-limbed robot bracing against tunnel walls.	15
2.2	Basic notation for frictional grasps.	18
2.3	Schematic view of rolling motion between the i^{th} finger and the object.	40
2.4	Schematic view of the forces applied on the i^{th} finger during roll motion.	49
2.5	The apparatus used for the two-fingered grasp experiments.	50
2.6	The springs calibration. The marked points show the measured points, and the line results from the linear regression.	51
2.7	Schematic view of the experiment setup that shows how the external forces are been applied to the grasped object.	52
2.8	(a) The feasible configurations set and (b) the force closure stability set of the first experiment.	52
2.9	For every angle of application the graph shows the maximum applied external force in the force closure stability set. Solid line represent analytic results and the dotted marks represent experimental results. .	53

2.10	The applied external wrenches shown in the wrench space.	54
2.11	Schematic view of the experiment setup that shows how the pure external torque is been applied to the grasped object.	55
2.12	The maximal allowable external torque vs. the preloading forces. In solid line is the computed maximal torque, and the marked dots are the experimental measurements.	56
2.13	The force closure stability set presented in the wrench space for different preloading forces.	57
3.1	Top view of a 3-limb spider robot moving in a planar tunnel environment.	64
3.2	(a) A 3-limb robot in a planar tunnel, and (b) the parametrization of its contact c-space.	66
3.3	(a) A gait feasible 3-limb posture, (b)-(c) contains two distinct 2-limb postures.	68
3.4	The minimal disc containing the three foothold positions when Δ is (a) an acute triangle, and (b) an obtuse triangle.	72
3.5	(a) Three cubes in contact c-space, and (b) their mutual partition into sub-cubes along the separating planes.	76
3.6	2D illustration of the effect of number of approximating cubes on the number of steps in the path	87
3.7	The 2-limb equilibrium postures in the (s_i, s_j) plane.	88
3.8	The collection of feasible 3-limb postures in contact c-space.	89
3.9	A five-cube approximation of the feasible 3-limb postures in the cell $I_1 \times I_6 \times I_1$	91

3.10	The collection of 270 maximal cubes approximating the feasible 3-limb postures.	91
3.11	The shortest path from S to T along the edges of the sub-cube graph in contact c -space.	92
3.12	The tunnel environment used in the simulations, and the sequence of footholds generated by the PCG algorithm.	94
4.1	The interpenetration of the spider-robot's footpad and the tunnel wall.	101
4.2	Schematic representation of the geometric relations in infinitesimal perturbations from the nominal penetration.	104
5.1	The tunnel environment used for the experiment, and the sequence of foothold positions generated by the PCG algorithm numbered from 1 to 10.	130
5.2	The shortest path from S to T along the edges of the sub-cube graph in contact c -space. In every node (step) along the path it is marked the foothold point on the tunnel of (limb 1, limb 2, limb 3).	131
5.3	Illustration that shows how net forward force is produced by the contact forces.	133
5.4	Measurements of the spider configuration parameters during the experiment. The desired path for every joint is indicated by dashed lines and the solid lines are the actual measurements.	134
5.5	Snapshots from the video showing the spider robot motion in the tunnel.	135

Abstract

In conventional motion planning a wheeled mobile robot navigates toward a goal configuration while avoiding collision with obstacles. However, many motion-planning problems are more suited for legged robots that interact with the environment in order to achieve stable locomotion. For example, surveillance of collapsed structures for survivors, inspection and testing of complex pipe systems, and maintenance of hazardous structures such as nuclear reactors, all require motion in congested, unstructured, and complex environments. In this work a second generation of planar spider-like robot for quasi-static motion in tunnel environments has been developed. A control method for this class of robots is introduced. The control method is based on new results in the fields of grasp theory, and control of asymmetric 2^{nd} -order linear systems. The control method ensures that when a spider-like mechanism bracing against the environment at equilibrium posture the naturally occurring compliance at the contacts stabilizes the mechanism as a single rigid body. Next an algorithm, named PCG, for selecting sequence of foothold positions along the tunnel has been developed. Finally, experimental results of the spider robot motion in tunnel environment verify the theories developed in this work.

List of Symbols

- \mathcal{A}_i : the i^{th} finger
 A_{ij} : the matrix $A_{ij} = JK_i P^{-1} K_j$
 $B(q, \dot{q})$: vector of Coriolis and centrifugal forces
 \mathcal{B} : a rigid object
 B_i : the matrix $B_i = JK_i$
 $\overline{B}(0, R)$: the closed 2D ball with radius R and centered in $(0, 0)$
 C : the maximal value of $f(x)$ for $x \in X_C$
 C_θ : the scalar $C_\theta = \sum_{i=1}^k (\rho_i^T K_i \rho_i - \rho_i^T K_i x_i^0 + \frac{1}{2} x_i^{0T} K_i x_i^0 - \rho_i^T F_i^0 + x_i^{0T} F_i^0) - W_t \theta$
 C_i : the vector $C_i = J(F_i^0 + K_i(x_i^0 - P^{-1} \sum_{j=1}^k \{F_j^0 + K_j x_j^0\}))$
 C_{ij} : the maximal value of $f(x)$ along the path $\Gamma_{ij}(t)$
 C_0 : the minimal value of $f(x)$
 C_L : the maximal value of $U(q)$ in for $q \in Q_L$
 C^* : is a scalar defined by $C > C^* > C_0$
 c : location for the robot's central-base
 c_i : in chapter 3 is the center point of the i^{th} maximal cube
 c_i : in chapter 4 is the parameter of Walton's loading path
 d : position of \mathcal{B} with respect to a fixed world frame

- \mathcal{E}_{ij}^{lm} : a set of two-limbed footholds equilibrium postures in contact configuration space
 F_i : the i^{th} contact force
 f_i : the i^{th} contact force
 F_i^0 : the i^{th} contact force at the initial equilibrium grasp
 FC_i : the i^{th} contact friction cone
 F_i^n, f_i^n : the normal component of F_i or f_i respectively
 F_i^t, f_i^t : the tangential component of F_i or f_i respectively
 \mathcal{F}_{ijk} : set of feasible 3-limb postures in the (i, j, k) cell
 \mathcal{FQ} : the set of \mathcal{B} 's configurations where the contact forces lie in their friction cones
 \mathbf{f}_i : a smooth function such that $\mathbf{f}_i(x_i) = 0$ when $x_i = x_i^0$
 G : the material shear modulus
 $g_i(s_i^{\mathcal{B}})$: a vector from the object origin to the boundary of \mathcal{B} near the i^{th} contact point
 $h_i(s_i^{\mathcal{A}})$: a vector from the i^{th} finger control point x_i^c to the boundary of \mathcal{A}_i near x_i
 h_i : in chapter 3 is the dimensions of the i^{th} maximal cube
 I_i : the segment in the contact configuration space corresponding to W_i
 J : $J = \begin{bmatrix} 0 & 1 \\ -1 & 0 \end{bmatrix}$
 J_i : the i^{th} contact Jacobian matrix
 K_i : the i^{th} contact stiffness matrix
 k : number of fingers or limbs
 L : total length of the tunnel walls
 $M(q)$: the spider-robot's inertia matrix
 m : in chapter 2 $m = 3$ for 2D and $m = 6$ for 3D spaces
 m : in chapter 3 is the number of optimization variables
 m : in chapter 4 is the number of free limbs
 N_i : the inward normal to the boundary of \mathcal{B} expressed in world coordinates
 n_i : the inward normal to the boundary of \mathcal{B} written in \mathcal{B} 's body coordinates
 \mathbf{n}_i : a unit vector normal to the i^{th} tunnel wall

n	: in chapter 3 is the number of tunnel segments
n	: in chapter 4 is the number of joints in each limb
$O(\cdot)$: order of
P	: in chapter 2 $P = \sum_{i=1}^k K_i$
P	: in chapter 4 is the controllers' proportional gain matrix
\mathcal{P}	: the set of configurations that satisfy the stability condition
$\mathcal{P}_{ij\times}$: set of 3-foothold positions that construct one 2-limbed equilibrium posture
PCG	: short for Partitioned Cubes Gaiting algorithm
p	: number of maximal cubes approximating a convex set
Q	: the spider-robot's damping matrix
Q_C	: sub level set of $U(q)$
Q_L	: a connected compact sub level set of $U(q)$ containing all critical pts. of $U(q)$
q	: vector of configuration parameters
\bar{q}	: the configuration of the joints in all limbs
q_0	: in chapter 2 is \mathcal{B} 's equilibrium configuration
q_0	: in chapter 4 is the central base configuration
q_i	: the i^{th} limb configuration
q^*	: in chapter 2 is an equilibrium point of the grasping system
q^*	: in chapter 4 is the spider's desired configuration
\hat{q}	: an equilibrium configuration of the entire robot
q^n	: normal traction
q^t	: tangential traction
\mathbb{R}^n	: n^{th} dimensional vector space of real numbers
$R(\theta) = \exp(\theta)$: rotation matrix of angle θ
R	: in chapter 3 is the robot reachability radius
R	: in chapter 4 is the footpad's radius
\mathcal{R}_{ijk}	: set of reachable 3-limb postures in the (i, j, k) cell

r	: the radial distance from the center of the contact area
$r_{min}(s_1, s_2, s_3)$: the radius of the minimal disc containing $x(s_1)$, $x(s_2)$, and $x(s_3)$
r_i	: the i^{th} contact point expressed in \mathcal{B} 's or central-base's body frame
r_i^0	: the coordinates of r_i at the initial grasp
S	: start node
\mathcal{S}	: a three-dimensional convex set
s_i	: in chapter 3 is parameterization of the i^{th} foothold position along the tunnel
s_i	: in chapter 2 is rolling parameter for the i^{th} finger motion relative to \mathcal{B}
$s_i^{\mathcal{B}}$: a length parameter to parameterize the object's boundary curve
$s_i^{\mathcal{A}}$: a length parameter to parameterize the finger boundary curve
T	: target node
$T(q, \dot{q})$: the robot's kinetic energy
t	: a parameter typically denotes the time
\mathbf{t}_i	: a unit vector tangential to the i^{th} tunnel wall
U_i	: elastic potential energy function of the i^{th} compliant contact
U	: $U(q) = \sum_{i=1}^k U_i(q)$
V_θ	: the vector $V_\theta^T = \sum_{i=1}^k (\rho_i^T K_i - x_i^{0T} K_i - F_i^{0T}) - W_f^T$
v_i^n	: the difference between \mathcal{B} 's and the i^{th} finger velocities in the normal direction
v_j	: a maximal cube vertex
W_i	: the i^{th} tunnel wall
\mathcal{W}_i	: the i^{th} feasible wrench cone
\mathbf{w}_i	: wrench generate by the i^{th} contact force
\mathbf{w}_{ext}	: external wrench acting on \mathcal{B}
\mathcal{W}	: the force closure set
\mathcal{W}_{global}	: the force closure stability set
w_f	: the torque part of w_{ext}

w_t	: the force part of w_{ext}
X_C	: $X_C = \{x : f(x) \leq C\}$ is a sub level set of $f(x)$
X_i	: a connected subset of X_C
x_i	: the i^{th} contact point expressed in a fixed world frame
\mathbf{x}_i	: the initial vertex of W_i
$x(s)$: a foothold position on tunnel wall correspond to s parameter in contact C-space
x_i^0	: the i^{th} contact points at the initial equilibrium grasp
x_i^m	: $x_i^m = \arg \min_{x \in X_i} f(x)$
x_i^c	: the i^{th} finger control point
z	: $z = \tan(\frac{1}{2}\theta)$
Γ_{ij}	: a continuous path connecting x_i^m to x_j^m
α_i	: the i^{th} finger orientation
$\delta = (\delta^n, \delta^t)$: the footpad's penetrations to the tunnel wall
δ^n	: the normal penetration
δ^t	: the tangential penetration
ϵ	: an arbitrarily small number
θ	: \mathcal{B} 's or the central-base's orientation
λ_{min}	: the minimal eigenvalue of a matrix
λ_{max}	: the maximal eigenvalue of a matrix
μ	: Coulomb's coefficient of friction
ν	: the material Poisson's ratio
ρ_i	: $\rho_i = R(\theta)r_i$
ϕ	: optimization target function
ψ	: a scalar constraint on the optimization process

Chapter 1

Introduction

In conventional motion planning a wheeled mobile robot navigates toward a goal configuration while avoiding collision with obstacles. However, many motion planning problems are more suited for legged robots that interact with the environment in order to achieve stable locomotion. For example, surveillance of collapsed structures for survivors [73], inspection and testing of complex pipe systems [55], and maintenance of hazardous structures such as nuclear reactors [62], all require motion in congested, unstructured, and complex environments. Our goal is to develop general purpose multi-limb mechanisms that uses quasi-static motion to navigate in such complex environments. In *quasi-static motion*, inertial effects due to moving parts of the robot are kept small relative to the forces and torques of interaction between the robot and the environment, and during this motion the robot maintains stable equilibrium with the environment.

A *spider-like robot* consists of k articulated limbs attached to a central body, such that each limb ends with a *footpad* (Figure 1.1). We assume that the robot moves quasistatically by exerting forces on the tunnel walls, while the robot is supported

against gravity by frictionless contacts mounted under the mechanism. In general, a spider-like robot must have at least *three* limbs in order to move quasistatically in planar tunnel environments. At every instant the spider braces against the tunnel walls in static equilibrium using two or three limbs. During a 2-limb posture the spider moves its free limb to the next foothold position. During a 3-limb posture the spider changes its internal geometry in preparation for the next limb lifting.

Spider-like and snake-like mechanisms are examples of robots that can move quasistatically in congested environments. Examples of spider-like robots are the pipe-crawling robots of Neubauer [51] and Pfeiffer et al. [60]. Other examples are the ladder-climbing robot of Dubowsky et al. [14, 40] and the nuclear-reactor servicing robot of Stone et al. [73]. Snake-like mechanisms are related to spider-like mechanisms, since both mechanisms brace against the environment while moving free parts toward a new position. Chrikjian and Burdick [9], Hirose and Morishima [23], and Shan and Koren [63] developed snake-like mechanisms that move by locking some of their links to the ground while allowing other links to move. Legged locomotion over a terrain is related to locomotion in congested environments. Examples of works in this area are by Boissonnat et al. [5], Hirose and Kunieda [22], Marhefka and Orin [41], McGeer [43], and Van-den-Doel and Pai [77]. However, we focus on locomotion in congested tunnel-like environments rather than legged locomotion over a terrain.

We make the following assumptions. First, we assume piecewise linear tunnel walls with known geometry. The tunnel can be discontinuous and can include holes or intersections. Second, each limb contacts the environment only through its footpad, which can only push against the environment. Third, each footpad contacts the tunnel walls through a frictional point contact, with a known lower bound on the coefficient of friction.

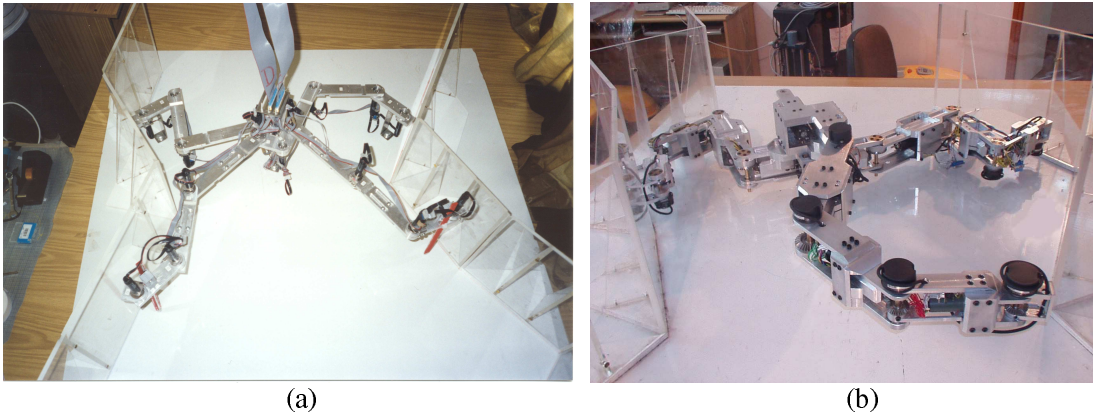


Figure 1.1: Two generations of a planar spider-robots. (a) 4-limb spider-robot capable of moving in frictionless tunnel environments, and (b) 3-limb spider robot capable of moving in frictional tunnel environments.

שני דורות של רובוט העכביש. (a) רובוט עכביש 4-רגלי המסוגל לנוע במנהרות ללא חיכוך, ו-(b) רובוט עכביש 3-רגלי המסוגל לנוע במנהרות עם חיכוך.

This work is a continuation of previous work on planar spider-robots moving in frictionless tunnel environments. In the previous work a first generation of the spider-robot has been developed (Figure 1.1 (a)) [64, 59, 58]. A potential function based and a PD control laws have been developed for this case [64, 65, 69]. A navigation algorithm for the motion of spider-robot in frictionless tunnel has been developed as well [19]. However, this navigation algorithm does not consider all possible foothold positions on the tunnel walls, rather it selects only one possible foothold position for every triplet of tunnel segments.

The design of the second generation spider shown in figure 1.1 (b) is strongly based on our experience with the first generation. We made two major changes in this version of the robot. First we use larger motors than in the first generation since we wish to use this robot for motion in gravitational force field (though it is not in the scope of this work). Therefore the motors should be powerful enough to support the entire robot's weight. The second change is by attaching the optical

encoders that measure each joint angle directly to the joint axle rather on the back of the motor. This way the controller has an accurate (8000 counts per revolution) measure of the joints angles and it can compensate for backlash in the gears. Since the mechanism apply forces on the tunnel walls the backlash is compensated (but dead zone still exist). Having unknown backlash is a major problem because it produces large amount of uncertainty in the footpads positions. Attaching the sensors directly on the joint axle overcome this problem.

Our goal is thus to develop a control and navigation algorithms for the motion of planar spider robot in tunnel environments. This work is divided to three independent work units. In the first part presented in chapter 2 we consider an object grasped by k compliant fingers. We analytically compute the conditions for it's stability and the set of external wrenches (i.e. forces and torques) that can be applied on object without destructing it's stability. This chapter on grasping is important and applicable for the control of spider-robot in a tunnel. When the spider-robot does not change it's internal configuration then from the tunnel point of view it can be seen as the tunnel walls grasp the mechanism. The second part presented in chapter 3 deals with optimal selection of sequence of foothold positions for the spider throughout the tunnel. The third part presented in chapter 4 introduces a decentralized PD control algorithm for the robot and provide conditions for it's stability based on the results from chapter 2 and based on new results on the stability of asymmetric second order linear systems. Experimental results of chapter 5 present full motion of the spider in the tunnel. In these experiments the foothold positions were selected by the algorithm of chapter 3 and the spider controller uses the control algorithm introduced in chapter 4.

1.1 Summary of Contributions

Here we summarize the contributions and the significance of the results presented in each chapter.

Contributions of chapter 2: In this chapter we introduce a class of grasps named *linearly controlled force closure grasps*, where a rigid object grasped by compliant fingers. The fingers obey linear force-displacement law, and contact the object through frictional contacts. The chapter makes four contributions. First, it provides necessary and sufficient conditions for force closure with compliant contacts. In particular, *the geometrical condition for active force closure is necessary but not sufficient for force closure with compliant contacts*. Second, the chapter characterizes the set of external wrenches that can be resisted by a given grasp. This set, called the *force closure set*, depends on the grasp geometry, the amount of friction at the contacts, the kinematics and dynamics of the grasping mechanism, as well as the preloading forces. Third, the chapter describes how to explicitly compute the force closure set for grasp arrangements where a compliant mechanism holds a rigid object. The chapter also presents global stability analysis, and computes the basin of attraction of the equilibrium point. Fourth, the chapter allows to compute the force closure set even for curved fingers where a rolling motion between the object and the fingers can occur. Finally, The force closure set has been verified in experiments. Part of this work was published in [67, 70].

Contributions of chapter 3: This chapter presents an algorithm, called *PCG*, (short for Partitioned Cubes Gaiting) for planning the foothold positions of spider-like robots in planar tunnels bounded by piecewise linear walls. we focus on 3-limb robots, but the algorithm generalizes to robots with a higher number of limbs. The input to

the PCG algorithm is a geometrical description of the tunnel, a lower bound on the amount of friction at the contacts, as well as start and target foothold positions. Using this knowledge, we established that the feasible 3-limb postures consist of a union of convex sets in contact c-space. Using efficient convex programming techniques, the algorithm approximates the possible foothold positions as a collection of cubes in contact c-space. Each cube represents a contact independent set of feasible 3-limb postures. A graph structure induced by the cubes has the property that its edges represent feasible motion between neighboring sets of 3-limb postures. This motion is realized by lifting one limb while the other two limbs brace the robot against the tunnel walls. A shortest-path search along the graph yields a 3-2-3 gait pattern that moves the robot from start to target using a minimum number of foothold exchanges. In practical environments the algorithm runs in $O(np^6 \log(np))$ time, where n is the number of tunnel walls and p is related to the cube approximation of contact c-space. Simulation results demonstrate the PCG algorithm in a tunnel environment, and experimental results present the spider-robot walking in a tunnel while selecting its foothold positions according to the PCG algorithm. This work has been partially published in [66].

Contributions of chapter 4: In this chapter we consider a k -limbed spider mechanism, such that each limb has n actuated degrees of freedom. The limbs are interconnected by a central base that has three *unactuated* degrees of freedom. A spider robot thus has $kn+3$ degrees of freedom, of which only kn degrees of freedom are actuated. If we regard the spider's configuration space as \mathbb{R}^{kn+3} , the control problem is how to induce forces and torques on the spider in order to bring it to a desired configuration in \mathbb{R}^{kn+3} . We present a control approach which is guaranteed to work

no matter what is the mass distribution of the spider or the geometry of the environment. Our approach exploits the natural compliance in the contacts to stabilize the mechanism using two three or even more footholds. Since we have frictional contacts we first derive the contact stiffness matrix. The contact stiffness matrix is not symmetric and we present the condition for it's symmetric part to be positive definite, which is a key property that we need in order to prove the stability of the mechanism. Next we present the spider-robot dynamic equations. We introduce a simple decentralized PD controller for the actuated joints of the robot. Then we find the equilibrium point of the closed-loop system. Following we analyze the stability of the system using linearization about the equilibrium. The linearized dynamics of the system is asymmetric. Therefore we develop new criteria for for the stability of second order asymmetric linear systems. These criteria are based on the fact that we consider system which it's symmetric part is stable, then a small enough asymmetric part should not destruct the stability of the system. In this chapter we introduce a computed lower bound on the stiffens of the PD controller the symmetric system is stable. Additionally an analytic criterion for the maximum allowed magnitude of the asymmetry of the system has been developed.

Contributions of chapter 5: This chapter presents experiments conducted with our 3-limbed spider robot. In these experiments the foothold positions were selected using the PCG algorithm and the entire mechanism was controlled with the control algorithm developed. The significance of these experiments is to show an application of the theories presents in this work. Moreover, it shows that it is possible to use these navigation and control theories in order to preform motion of real walking spider robot in tunnel environment.

Chapter 2

Force Closure Set

2.1 Introduction

The notion of *force closure* was originally formulated for multi-fingered robot hands [32, 61]. This notion should be called *active* force closure, since it requires that the fingers be able to actively balance any disturbing wrench (i.e. force and torque) acting on the grasped object. Active force closure requires sophisticated contact-force sensors and agile contact-force controllers whose action must be precisely coordinated. However, in applications such as fixturing the grasping elements are simple devices that are preloaded against an object with initial grasping forces [46]. Physical processes at the contacts, such as friction and compliance, provide passive stabilization of the object against external disturbances. Another important application concerns multi-fingered mechanisms that establish an initial grasp of an object. Using decoupled position-based controllers for the individual fingers, the effective compliance of the grasping mechanism together with friction at the contacts provide stabilization of the grasped object (Figure 2.1(a)). A related application is a multi-limbed robot

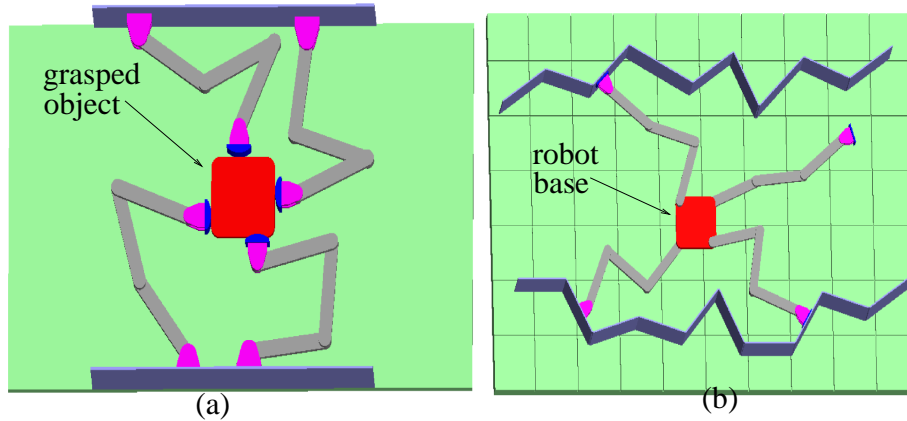


Figure 2.1: (a) A multi-fingered hand grasping an object. (b) A multi-limbed robot bracing against tunnel walls.

איור 2.1: (a) יד מרובת אצבעות אווזת אובייקט. (b) רובוט מרובה גפיים נאחז כנגד דפנות מנהרה.

bracing against a tunnel-like environment in static equilibrium (Figure 2.1(b)). Here the tunnel walls play the role of the grasped object, and the robot stabilizes itself by pushing against the walls using decentralized position-based controllers. In all of these examples stabilization is achieved without active control or coordination of the contact forces.

Consider a grasp arrangement where each finger or contacting body obeys its own force-displacement law. In particular, some fingers may apply a fixed force on the object. The grasp is *force closure* if for suitably selected initial grasping forces, the fingers or bodies contacting the object balance any external wrench in a neighborhood about the origin. The literature on active force closure is only partially relevant for studying force closure with compliant contacts. Examples of works on friction-based active force closure are [42, 53, 76]. Specifically, Jen Shoham and Longman [30] developed a force control law for the fingers to stabilize force-closure grasps. Examples of works that additionally consider the structure of the grasping

mechanism are [3, 20, 27, 39, 47].

This chapter makes four contributions. First, it provides necessary and sufficient conditions for force closure with compliant contacts. In particular, *the geometrical condition for active force closure is necessary but not sufficient for force closure with compliant contacts*. Second, the chapter characterizes the set of external wrenches that can be resisted by a given grasp. This set, called the *force closure set*, depends on the grasp geometry, the amount of friction at the contacts, the kinematics and dynamics of the grasping mechanism, as well as the preload forces. Third, the chapter describes how to explicitly compute the force closure set for grasp arrangements where a compliant mechanism holds a rigid object. Such grasp arrangements arise in multi-fingered hands and multi-limbed robots that interact with rigid objects using simple position-based controllers [13]. The chapter also present global stability analysis, and show analytical criterion for the global stability of the equilibrium point. Fourth, the chapter allow to compute the force closure set even for curved fingers where a rolling motion between the object and the fingers can occur. Finally, we compare the the passive closure set for 2-finger linearly compliant planar grasps with experiments. The experiments verify the force closure set and closely match the computed set.

2.2 Geometric Definition of Force Closure Grasps

In this section we review the notion of active force closure. Then we describe necessary and sufficient conditions for the existence of force closure with compliant contacts.

2.2.1 Frictional Grasps Terminology

We study 2D or 3D grasps, where a rigid object \mathcal{B} is held in frictional point contact by k rigid bodies $\mathcal{A}_1, \dots, \mathcal{A}_k$. The bodies $\mathcal{A}_1, \dots, \mathcal{A}_k$ represent fixturing elements or the fingertips of a multi-fingered hand. Although we use the language of grasping, these bodies can also represent the footpads of a multi-limbed robot. The contact point between \mathcal{A}_i and \mathcal{B} is denoted r_i when expressed in \mathcal{B} 's body frame, and x_i when expressed in a fixed world frame (Figure 2.2). The two representations of the i^{th} contact point are related by the rigid-body transformation: $x_i = Rr_i + d$, where d and R are the position and orientation of \mathcal{B} with respect to a fixed world frame. The orientation matrix R is parametrized by the exponential map, $R(\theta) = \exp(\theta)$, where $\theta \in \mathbb{R}$ in 2D and $\theta \in \mathbb{R}^3$ in 3D. The object configuration is parametrized by $q = (d, \theta) \in \mathbb{R}^m$, where $m = 3$ in 2D and $m = 6$ in 3D. The wrench generated by a force F_i acting on \mathcal{B} at x_i is given by the familiar formula:

$$\mathbf{w}_i = \begin{pmatrix} F_i \\ \boldsymbol{\rho}_i \times F_i \end{pmatrix} \quad \text{where } \boldsymbol{\rho}_i = R(\theta)r_i.$$

The collection of wrenches that act on \mathcal{B} at a particular configuration q is called the *wrench space* at q . This space can be identified with \mathbb{R}^m .

We assume the standard Coulomb friction model: $|F_i^t| \leq \mu|F_i^n|$, where F_i^t and F_i^n are the tangent and inward normal components of F_i , and μ is the coefficient of Coulomb friction¹. The force F_i can only push on the object, and this constraint is described by the inequality $F_i^n \geq 0$. The friction cone at the i^{th} contact, denoted FC_i , is the collection of all frictional forces that can be applied to \mathcal{B} at x_i , and it is given by

¹In 3D, under a soft-contact model there is also frictional torque about the contact normal.

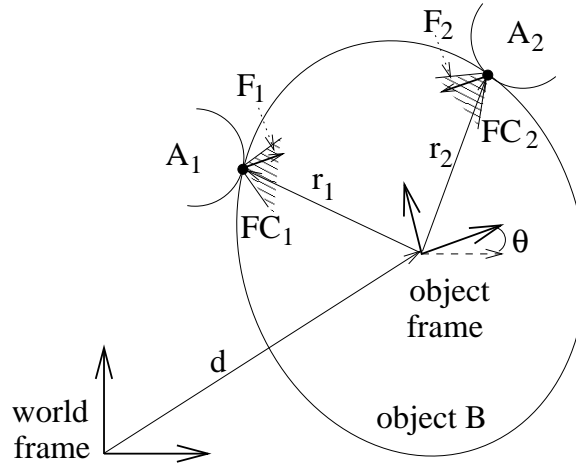


Figure 2.2: Basic notation for frictional grasps.
 סימונים בסיסיים לאחיזות המערבות מגעים עם חיכוך.

$$FC_i = \{F_i: F_i^n \geq 0 \text{ and } -\mu F_i^n \leq F_i^t \leq \mu F_i^n\}.$$

The set of wrenches generated by all forces in FC_i forms a cone of feasible wrenches.

The i^{th} feasible wrench cone, denoted \mathcal{W}_i , is given by

$$\mathcal{W}_i = \{\mathbf{w}_i: \mathbf{w}_i = \begin{pmatrix} F_i \\ \boldsymbol{\rho}_i \times F_i \end{pmatrix}, \forall F_i \in FC_i\}.$$

When \mathcal{B} is held by k fingers, we say that \mathcal{B} is in *equilibrium* if in the absence of any external wrench there exist feasible wrenches $\mathbf{w}_i \in \mathcal{W}_i$ for $i = 1, \dots, k$ such that $\sum_{i=1}^k \mathbf{w}_i = \vec{0}$.

2.2.2 Review of Active Force Closure

Active force closure is the standard notion of force closure [53, 76]. The collection of wrenches that can be generated by k frictional contacts is given by the set sum:

$\mathcal{W}_1 + \dots + \mathcal{W}_k = \{\mathbf{w}_1 + \dots + \mathbf{w}_k : \mathbf{w}_i \in \mathcal{W}_i \text{ for } i = 1, \dots, k\}$. This notation is used

in the following standard definition.

Definition 1 *Let an object \mathcal{B} be held in equilibrium grasp by k frictional point contacts. Let \mathcal{W}_i be the feasible wrench cone of the i^{th} contact. Then the grasp is **active force closure** if the sum of the wrench cones $\mathcal{W}_1 + \dots + \mathcal{W}_k$ spans the entire wrench space \mathbb{R}^m , where $m=3$ in 2D and $m=6$ in 3D.*

The active aspect of the grasp lies in the assumption that the grasping bodies can generate any contact force within the respective friction cones. The following theorem gives a simple rule for determining force closure [53, 80]. By definition, a grasp is *non-marginal* when the contact forces are non-zero and lie in the interior of their respective friction cones.

Theorem 1 (Active Force closure) *Let a 2D or 3D object \mathcal{B} be grasped by k frictional contacts, such that the contacts do not lie along the same spatial line when the grasp is 3D. Then the grasp is **active force closure** iff it is possible to establish a non-marginal equilibrium grasp of \mathcal{B} .*

2.2.3 Force Closure with Compliant Contacts

Force closure is based on the assumption that the contact forces can be freely modified within the respective friction cones. However, when the contact points are compliant each contact force obeys some force-displacement relationship subject to friction constraints at the contacts. To formalize this notion, we define three types of contacts that encapsulate three common types of force-displacement laws and other modelling idealizations.

Definition 1 • **A rigid-body contact** *is a stationary rigid-body that passively interacts with \mathcal{B} through a frictional contact.* • **A fixed-force contact** *is a frictional point*

contact that applies a specific force at the contact point. • A **compliant contact** is a frictional contact that applies force according to a force-displacement relationship of the contact point.

Let us give examples of these types of contacts. Rigid-body contacts are commonly used in fixturing applications to restrict the motions of a workpiece. Fixed-force contacts are generated by mechanisms such as pressure-controlled hydraulic fixels and force-controlled robot grippers. Compliant contacts are generated by finger and limb mechanisms whose joints are controlled by position-servoed controllers [13, 61], or by spring loaded fixtures. A more complex type of contact occurs when several contacts are coupled together by the grasping mechanism. Such coupled contacts often occur in power or enveloping grasps [80]. In order to avoid such coupled contacts, we assume that *each contact is generated by its own independent mechanism.*

We now give necessary and sufficient conditions for force closure of grasps having frictional compliant or fixed-force contacts, as well as frictionless rigid-body contacts. The conditions are based on the following notion of potential energy function. The wrench generated by a compliant contact can be written as $\mathbf{w}_i = -\nabla U_i(q)$, where $U_i(q)$ is the elastic potential energy function induced on \mathcal{B} by the i^{th} compliant contact². Similarly, the wrench generated by a fixed-force contact is induced by a potential function which is linear in x_i , where $x_i = R(\theta)r_i + d$. The wrench generated by a frictionless passive rigid-body contact also has the form $\mathbf{w}_i = -\nabla U_i(q)$, where the elastic energy function is given by the Hertz formula from elasticity theory [31]. (This theory treats the contacting bodies as quasi-rigid.) The total potential energy of \mathcal{B} is the sum $U(q) = \sum_{i=1}^k U_i(q)$.

² $U_i(q)$ is identically zero when the i^{th} contact is broken.

Proposition 2.2.1 *Let a 2D or 3D object \mathcal{B} be held in equilibrium grasp by k independent compliant frictional contacts, fixed-force frictional contacts, or frictionless rigid-body contacts. Let q_0 be \mathcal{B} 's equilibrium configuration, and let $U(q)$ be the potential energy induced on \mathcal{B} by the contacts. Then the following two conditions are sufficient for **force closure**:*

1. *The initial equilibrium grasp is non-marginal. (In 3D the contacts must not lie along a common line.)*
2. *The equilibrium q_0 is a non-degenerate local minimum of the potential energy function $U(q)$.*

Moreover, in all generic grasps conditions (1) and (2) are also necessary for passive force closure.

A proof of the proposition is sketched in appendix A.1. The first condition of the proposition states that the grasp must satisfy the condition for active force closure. I.e., the grasp must be active force closure if the contacts are made fully active. The second condition is the standard stability condition for compliant grasps [27, 39]. *The stability condition ensures that when an external wrench acts on \mathcal{B} , the object would automatically settle at a new equilibrium in the vicinity of q_0 where the contact forces balance the external wrench.* Note that two issues play a role in this convergence. First, the equilibrium induced by the external wrench must be locally stable. Second, the original unperturbed equilibrium must lie in the basin of attraction of the new equilibrium. Finally, the proposition generalizes to any type of contact whose dynamics varies smoothly with the external wrench acting on \mathcal{B} .

2.3 The Force Closure Set of Compliant Grasps

Given a force closure grasp, the *force closure set* is the collection of external wrenches which are automatically balanced by the contacts. In this section we characterize the force closure set of force closure grasps with compliant contacts.

2.3.1 Characterization of The Force Closure Set

Let us depict a fundamental difficulty in computing the force closure set. The Coulomb friction model allows generation of tangential forces at the contacts up to a limit determined by μ times the normal component of the contact forces. In compliant grasps the normal component of the contact forces is determined by the initial preload of the grasp, and can change only in response to an external wrench \mathbf{w}_{ext} acting on \mathcal{B} . In other words, the normal loadings at the contacts cannot “spontaneously” change as they do in fully active contacts. Thus we write the normal loading at the i^{th} contact as $F_i^n(\mathbf{w}_{ext})$. The friction cone at the i^{th} contact is determined by the inequality $|F_i^t| \leq \mu F_i^n(\mathbf{w}_{ext})$, and this friction cone determines a \mathbf{w}_{ext} -dependant feasible wrench cone denoted $\mathcal{W}_i(\mathbf{w}_{ext})$. An external wrench can be possibly balanced by the contacts only when the recursive relation $\mathbf{w}_{ext} \in \mathcal{W}_1(\mathbf{w}_{ext}) + \dots + \mathcal{W}_k(\mathbf{w}_{ext})$ holds true. The solution of this recursive relation is a key step in computing the closure stability set.

The *compliant grasps* are defined as grasps where a rigid object \mathcal{B} is held by compliant finger mechanisms. This class of grasps also includes multi-limbed robots bracing against a rigid environment. The rigidity of \mathcal{B} is an excellent approximation—although all objects exhibit some natural compliance at the contacts, this compliance

is negligible relative to the compliance induced by the joints of the grasping mechanism. For example, consider our experimental multi-limbed robot depicted in Figure 2.1(b) [71]. Each limb of this robot has four joints actuated by Maxon motors that generate a stiffness of 2 N/mm at the footpads. In contrast, the stiffness of objects made of Aluminum is $4.5 \cdot 10^3$ N/mm.

We make the following simplifying assumptions. First, each finger mechanism is assumed to interact with \mathcal{B} through a pointed finger-tip. This assumption implies that when a finger-tip locally rolls on the surface of \mathcal{B} , the location of the contact point remains fixed in \mathcal{B} 's body frame. Second, we assume that each finger mechanism is fully actuated, so that it can generate any force in \mathbb{R}^n , where $n=2$ in 2D and $n=3$ in 3D. Our third assumption is that each finger generates a force-displacement law of the form:

$$F_i = F_i^0 + \mathbf{f}_i(x_i), \quad (2.1)$$

where F_i^0 and x_i^0 are the contact forces and contact points at the initial equilibrium grasp, and \mathbf{f}_i is a smooth function such that $\mathbf{f}_i(x_i) = 0$ when $x_i = x_i^0$.

Our first step in the characterization of the force closure set is to express the contact forces as a function of the object configuration $q = (d, \theta)$. The i^{th} contact point is given by $x_i = R(\theta)r_i + d$, where r_i is the description of x_i in \mathcal{B} 's body coordinates. Let r_i^0 denote the coordinates of r_i at the initial grasp. Let \mathcal{FQ} denote the collection of \mathcal{B} 's configurations where the contact forces lie in their respective friction cones. (The set \mathcal{FQ} is considered below.) Then the pointed-finger assumption together with the rigidity of \mathcal{B} guarantee that *the points r_i remain fixed in \mathcal{B} 's body frame*, for all configurations $q \in \mathcal{FQ}$. Thus we may write $x_i = R(\theta)r_i^0 + d$ for $i = 1, \dots, k$. Substituting for the x_i 's in (2.1) gives the desired expression for the

contact forces:

$$F_i(d, \theta) = F_i^0 + \mathbf{f}_i(x_i(d, \theta)) \quad i = 1, \dots, k. \quad (2.2)$$

The approach presented here for computing the contact forces was originally proposed by Bicchi [2]. However, Bicchi assumes only a small change of Δq in the object's configuration, with a linear force-displacement law. Our formulation generalizes Bicchi's approach to any object configuration and any force-displacement law.

Next we write an expression for the set of feasible configurations \mathcal{FQ} . This set is given by the intersection $\mathcal{FQ} = \cap_{i=1}^k \mathcal{FQ}_i$, where \mathcal{FQ}_i denotes the collection of \mathcal{B} 's configurations where the i^{th} contact force $F_i(q)$ lies in the friction cone FC_i . Let n_i denote the inward normal to the boundary of \mathcal{B} at r_i , written in \mathcal{B} 's body coordinates. And let N_i be the inward unit normal to the boundary of \mathcal{B} at x_i , expressed in world coordinates. Then $N_i = R(\theta)n_i$, and the normal component of the i^{th} contact force is: $F_i^n = F_i \cdot N_i = F_i \cdot (R(\theta)n_i)$. The tangential component of F_i is: $F_i^t = \|[I - N_i N_i^T]F_i\| = \|[I - n_i n_i^T]R(\theta)^T F_i\|$. Substituting for F_i^n and F_i^t in the inequalities that define FC_i gives:

$$\begin{aligned} \mathcal{FQ}_i = \{q = (d, \theta): F_i \cdot (R(\theta)n_i) \geq 0 \quad \text{and} \\ \|[I - n_i n_i^T]R(\theta)^T F_i\| \leq \mu F_i \cdot (R(\theta)n_i)\}, \end{aligned}$$

where μ is the coefficient of friction. Substituting for the forces F_i according to (2.2) gives:

$$\begin{aligned} \mathcal{FQ}_i = \{q = (d, \theta): F_i(d, \theta) \cdot (R(\theta)n_i) \geq 0 \quad \text{and} \\ \|[I - n_i n_i^T]R(\theta)^T F_i(d, \theta)\| \leq \mu F_i(d, \theta) \cdot (R(\theta)n_i)\}. \end{aligned}$$

The desired set \mathcal{FQ} is the intersection of the sets \mathcal{FQ}_i for $i = 1, \dots, k$. Our third step is to identify the configurations that guarantee stable convergence of \mathcal{B} to the equilibrium induced by an external wrench. This condition is captured by the requirement

that the second-derivative matrix of the grasp potential energy function, $D^2U(q)$, be positive definite. The set of configurations that satisfy this stability condition, denoted \mathcal{P} , is given by

$$\mathcal{P} = \{q = (d, \theta) : \lambda_{\min}(D^2U(q)) > 0\}, \quad (2.3)$$

where λ_{\min} denotes the minimal eigenvalue of a matrix. Condition (2.3) guarantees local stability of the equilibrium induced by \mathbf{w}_{ext} at q . However, it does not guarantee that \mathcal{B} 's original equilibrium at q_0 lies in the basin of attraction of the new equilibrium at q . The condition for global convergence from q_0 to q is presented in the next section.

Finally, the net wrench generated on \mathcal{B} by the contact forces is $\mathbf{w} = \sum_{i=1}^k (F_i, \boldsymbol{\rho}_i \times F_i)$. Since F_i and $\boldsymbol{\rho}_i$ are functions of q , \mathbf{w} can be interpreted as a mapping from configuration space to wrench space. The force closure set, denoted \mathcal{W} , is the image in wrench-space of the configurations q in $\mathcal{FQ} \cap \mathcal{P}$ under the mapping $\mathbf{w}(q)$:

$$\mathcal{W} = \left\{ \mathbf{w} = \sum_{i=1}^k \begin{pmatrix} F_i(q) \\ \boldsymbol{\rho}_i(q) \times F_i(q) \end{pmatrix} : q \in \mathcal{FQ} \cap \mathcal{P} \right\}.$$

Any wrench \mathbf{w}_{ext} in \mathcal{W} would be automatically balanced by the contacts of the grasp.

Theorem 2 *For any $\mathbf{w}_{ext} \in \mathcal{W}$ there exist a locally stable equilibrium point q^**

Proof: The equilibrium equation is

$$\mathbf{w}_{ext} = \sum_{i=1}^k \begin{pmatrix} F_i(q^*) \\ \boldsymbol{\rho}_i(q^*) \times F_i(q^*) \end{pmatrix}$$

and since \mathbf{w}_{ext} is function of q^* thus there exist a configuration q^* that is an equilibrium point. Moreover, This equilibrium point q^* is in $\mathcal{FQ} \cap \mathcal{P}$. It means that the forces can be applied by the frictional contacts, and the equilibrium is locally stable.

□

2.3.2 The Force Closure Set Under Linear Compliance Law

Next we compute the force closure set of compliant grasps whose contacts specifically obey a *linear* compliance law of the form:

$$F_i = F_i^0 - K_i(x_i - x_i^0), \quad (2.4)$$

where F_i^0 and x_i^0 are the contact forces and contact points at the initial equilibrium grasp, and K_i is an $n \times n$ positive semi-definite matrix ($n = 2$ in 2D and $n = 3$ in 3D). First we substitute the linear law (2.4) into (2.2):

$$F_i(d, \theta) = F_i^0 - K_i((R(\theta)r_i^0 + d) - x_i^0) \quad i = 1, \dots, k.$$

Next we substitute for the contact forces $F_i(d, \theta)$ in the inequalities that define the sets $\mathcal{F}Q_i$. This substitution yields a closed-form expression for the set of feasible configurations, $\mathcal{F}Q = \cap_{i=1}^k \mathcal{F}Q_i$. Finally, the inequality that defines the locally stable configurations requires a formula for $D^2U(q)$. This formula is provided in the following lemma. Given a vector $u \in \mathbb{R}^3$, $[u \times]$ denotes the 3×3 skew-symmetric matrix satisfying $[u \times]v = u \times v$ for all $v \in \mathbb{R}^3$.

Lemma 2.3.1 ([53, 68]) *Let a rigid object \mathcal{B} be grasped by k compliant contacts each satisfying the linear compliance law (2.4). Then the formula for $D^2U(q)$ in the 3D case is:*

$$D^2U(q) = \sum_{i=1}^k \begin{bmatrix} K_i & K_i[\rho_i \times] \\ [\rho_i \times]^T K_i & [\rho_i \times]^T K_i [\rho_i \times] + ([F_i \times][\rho_i \times])_s \end{bmatrix} \quad (2.5)$$

where for a given matrix A , $A_s = \frac{1}{2}(A + A^T)$. The formula for $D^2U(q)$ in the 2D case is:

$$D^2U(q) = \sum_{i=1}^k \begin{bmatrix} K_i & -K_i J \rho_i \\ -(J \rho_i)^T K_i & (J \rho_i)^T K_i J \rho_i + F_i \cdot \rho_i \end{bmatrix}, \quad (2.6)$$

$$\text{where } J = \begin{bmatrix} 0 & 1 \\ -1 & 0 \end{bmatrix}.$$

The full derivation of $D^2U(q)$ appears in Appendix A.1

2.4 Global Stability Analysis

In this section we will develop analytic criteria to check whether the origin is in the basin of attraction of a given equilibrium point. This will ensure that an object located initially in the origin of the world reference frame will converge to a given equilibrium point while an external wrench applied on the object.

2.4.1 The Grasped Object Equilibria

First we would like to find all the possible equilibrium point for a given constant external wrench w_{ext} . Note that $w_{ext} = (w_f, w_t)^T$, where w_f and w_t are the force and the torque parts of w_{ext} respectively. In equilibrium $\sum_{i=1}^k F_i + w_f = 0$, and if we substitute F_i from (2.4) we get

$$\sum_{i=1}^k \{F_i^0 - K_i(\rho_i(\theta) + d - x_i^0)\} + w_f = 0$$

Next we isolate the position vector d as function of $\rho(\theta)$ and denote $P = \sum_{i=1}^k K_i$.

Thus we have

$$d = P^{-1} \sum_{i=1}^k \{F_i^0 - K_i(\rho_i(\theta) - x_i^0)\} + w_f. \quad (2.7)$$

The second equilibrium equation is that the sum of the external torque and the torques that all the forces apply on the object is equal to zero. Explicitly that means that $\sum_{i=1}^k \{\rho_i \times F_i\} + w_t = 0$, and substitution of F_i yields

$$\sum_{i=1}^k \{\rho_i \times [F_i^0 - K_i(\rho_i(\theta) + d - x_i^0)]\} + w_t = 0.$$

Note that this is a scalar equation. The term $\rho_i \times F_i$ can be written as $\rho_i^T J F_i$.

Substitution of the linear compliance law for F_i and d from equation (2.7) yields to

$$\sum_{i=1}^k \{\rho_i^T J [F_i^0 - K_i(\rho_i - x_i^0 + P^{-1} \sum_{j=1}^k \{F_j^0 - K_j(\rho_j - x_j^0)\} + w_f)]\} + w_t = 0.$$

To ease the writing we denote

$$A_{ij} = J K_i P^{-1} K_j,$$

$$B_i = J K_i,$$

and

$$C_i = J(F_i^0 + K_i(x_i^0 - P^{-1} \sum_{j=1}^k \{F_j^0 + K_j x_j^0\})),$$

Where $i = 1..k$ and $j = 1..k$. Furthermore, A_{ij} , B_i and C_i are all constants that do not depend on the object configuration and not on the external wrench. We rearrange the above equation and have

$$\sum_{i=1}^k \left[\sum_{j=1}^k (\rho_i(\theta)^T A_{ij} \rho_j(\theta)) - \rho_i(\theta)^T B_i \rho_i(\theta) + \rho_i(\theta)^T C_i - \rho_i(\theta)^T J P w_f \right] + w_t = 0. \quad (2.8)$$

Based on this result the following lemma characterize the possible number of equilibrium points a grasped object can have.

Lemma 2.4.1 (Maximum Number of Equilibrium Points) *Let a rigid object \mathcal{B} be grasped by k compliant contacts each satisfying the linear compliance law (2.4). Then for a given external wrench and preloading forces, \mathcal{B} has 0, 2 or 4 equilibrium points.*

Proof: The only unknown variable in the scalar equation (2.8) is θ . The solution of this equation give us the θ values of the equilibrium points. These values can be substitute into (2.7) to calculate the complete configuration of the equilibrium points.

$\rho_i(\theta)$ in equation (2.8) is $\begin{bmatrix} \cos(\theta) & -\sin(\theta) \\ \sin(\theta) & \cos(\theta) \end{bmatrix} r_i^0$, where r_i^0 is a constant vector of the i^{th} initial contact point. So equation (2.8) contains terms of $\sin^2(\theta), \cos^2(\theta)$ and $\sin(\theta) \cdot \cos(\theta)$. There are no higher orders of the power of $\sin(\theta)$ and $\cos(\theta)$. Next we use the famous substitution of $z = \tan(\frac{1}{2}\theta)$, then $\sin(\theta) = \frac{2z}{1+z^2}$ and $\cos(\theta) = \frac{1-z^2}{1+z^2}$. If we substitute these terms into (2.8) and solve for z , we get a quartic equation (i.e. fourth order polynomial equation) in z [16]. A fourth order polynomial has 0,2 or 4 real roots. Two times the arc tan of these roots are the θ values of the equilibrium points and together with $d(\theta)$ from (2.7) they are the critical points of $U(q)$. \square

2.4.2 Stability Characterization

we examine the shape of $U(q)$. The following lemma states the specific shape of the level sets of $U(q)$ in every θ layer.

Lemma 2.4.2 (Shape of θ Layers of Level Sets of $U(q)$) *The shape of the set $\{q = (d, \theta) : U(d, \theta = Const.) = Const.\}$ is ellipse, point or \emptyset .*

Proof: Let us write $U(q)$ explicitly as

$$U(q) = \sum_{i=1}^k \left[\frac{1}{2} (\rho_i + d - x_i^0)^T K_i (\rho_i + d - x_i^0) - (\rho_i + d - x_i^0)^T F_i^0 \right] - q^T w_{ext}. \quad (2.9)$$

It is possible to rewrite $U(q)$ in the following form

$$U(q) = \frac{1}{2} d^T P d + V_\theta^T d + C_\theta,$$

where $P = \sum_{i=1}^k K_i$, $V_\theta^T = \sum_{i=1}^k (\rho_i^T K_i - x_i^{0T} K_i - F_i^{0T}) - w_f^T$, and $C_\theta = \sum_{i=1}^k (\rho_i^T K_i \rho_i - \rho_i^T K_i x_i^0 + \frac{1}{2} x_i^{0T} K_i x_i^0 - \rho_i^T F_i^0 + x_i^{0T} F_i^0) - w_t \cdot \theta$. The completion of $U(q)$ to full quadratic form yields

$$U(q) = \frac{1}{2}(d + P^{-1}V_\theta)^T P(d + P^{-1}V_\theta) - \frac{1}{2}V_\theta^T P^{-1}V_\theta + C_\theta, \quad (2.10)$$

and for $U(q) = C_U = Const$ we get

$$\frac{1}{2}(d + P^{-1}V_\theta)^T P(d + P^{-1}V_\theta) = C_U - C_\theta + \frac{1}{2}V_\theta^T P^{-1}V_\theta. \quad (2.11)$$

For a given $\theta = Const$ layer the right hand side of equation (2.11) is a constant scalar number and the left hand side is a quadratic form with the matrix P positive definite. That is equation (2.11) is simply an ellipse equation that can be degenerated to a point or to an empty set. \square

Following are definition lemma and theorem that help us finding the topology of the sub level sets of $U(q)$.

Definition 2 (Compact Function) *Let a function $f(x) : \mathbb{R}^n \mapsto \mathbb{R}$ be a continuous differentiable function, and let $X_C = \{x : f(x) \leq C\}$ be a sub level set of $f(x)$, where $C \in \mathbb{R}$. Then $f(x)$ is a compact function if there exist a constant C_0 such that for any $C < C_0$ $X_C = \emptyset$, and for any $C > C_0$ X_C is compact.*

Lemma 2.4.3 (Compact Function $U(q)$) *The function $U(q)$ as in (2.9) is a compact function. Meaning that for every $C \in \mathbb{R}$ the sub level set of $U(q)$ $Q_C = \{q : U(q) \leq C\}$ is a compact set or \emptyset .*

Proof: To show that Q_C is compact we have to show that Q_C is closed and bounded. $U(q)$ is bounded from below because of the following reasons. The first term of (2.10) is positive semi definite since it is a quadratic form with the matrix P positive definite.

The second and third terms in (2.10) depends only on θ which is a bounded cyclic coordinate. These terms are continuous functions of $\theta \in [0, 2\pi]$ and therefore accept a minimal and maximal values $-M_1 \leq -\frac{1}{2}V_\theta^T P^{-1}V_\theta + C_\theta \leq M_3$, where M_1 and M_3 are positive real constant numbers. Thus all the components of $U(q)$ sums up to a function that is bounded from below. For C smaller from this lower bound $Q_C = \emptyset$, otherwise $Q_C \neq \emptyset$ and for that case we need to prove that Q_C is compact. Next we Show that Q_C is bounded. The first term in (2.10) is a quadratic form that takes the form $u^T P u$ with $P \in \mathbb{R}^{2 \times 2}$ positive definite matrix. For such quadratic form we can have

$$\lambda_{min}(P)\|u\|^2 \leq u^T P u \leq \lambda_{max}(P)\|u\|^2,$$

where u is an arbitrary vector and $\lambda_{min}(P), \lambda_{max}(P)$ are the minimal and maximal eigenvalues of P . The reason for this is as follows. We can define an orthonormal matrix Λ , where the columns of Λ are the normalized eigenvectors of P . The matrix $\Lambda^T P \Lambda$ is the diagonal matrix $diag(\lambda_1(P), \lambda_2(P))$, and $v^T \Lambda^T P \Lambda v = \lambda_1(P)v_1^2 + \lambda_2(P)v_2^2$. Following $\lambda_{min}(P)\|v\|^2 \leq v^T \Lambda^T P \Lambda v \leq \lambda_{max}(P)\|v\|^2$. Define $u = \Lambda v$ and we get $\lambda_{min}(P)\|v\|^2 \leq u^T P u \leq \lambda_{max}(P)\|v\|^2$. But $\|u\|^2 = u^T u = v^T \Lambda^T \Lambda v$ and since Λ is orthogonal $\Lambda^T \Lambda = I$ and $\|u\|^2 = v^T v = \|v\|^2$. Substituting back this result yield $\lambda_{min}(P)\|u\|^2 \leq u^T P u \leq \lambda_{max}(P)\|u\|^2$. Using this result we can substitute these bounds to (2.10) and get

$$U(q) \geq \frac{1}{2}\lambda_{min}(P)\|(d + P^{-1}V_\theta)\|^2 - M_1.$$

The triangle inequality state that $\|w_1\| - \|w_2\| \leq \|w_1 + w_2\| \leq \|w_1\| + \|w_2\|$. Using the triangle inequality we get

$$U(q) \geq \frac{1}{2}\lambda_{min}(P)(\|d\| - \|P^{-1}V_\theta\|)^2 - M_1.$$

Since $\|P^{-1}V_\theta\|$ is a continuous function over the interval $\theta \in [0, 2\pi]$ it accept a minimum and maximum values $M_2 \leq \|P^{-1}V_\theta\| \leq M_4$. Substituting this result to the previous equation yields

$$U(q) \geq \frac{1}{2}\lambda_{\min}(P)(\|d\| - M_2)^2 - M_1. \quad (2.12)$$

Consider the sub level set where $U(q) \leq C$ then

$$\frac{1}{2}\lambda_{\min}(P)(\|d\| - M_2)^2 - M_1 \leq U(q) \leq C$$

So we get $(\|d\| - M_2)^2 \leq \frac{2(C+M_1)}{\lambda_{\min}(P)}$ since $\lambda_{\min}(P)$ is positive. It follows that

$$\|d\| \leq \sqrt{\frac{2(C + M_1)}{\lambda_{\min}(P)}} + M_2 \equiv R,$$

where R is the radius of the circle containing all the (x, y) points for which $U(q) \leq C$.

We conclude that

$$Q_C \subset \{(x, y, \theta) : \theta \in [0, 2\pi], (x, y) \in \overline{B}(0, R)\},$$

where $\overline{B}(0, R)$ is the closed 2D ball with radius R and center in $(0, 0)$. This mean that Q_C is bounded within a close cylinder. Finally, there exist a theorem that states that for a continuous function $f : \mathbb{R}^n \mapsto \mathbb{R}$ the source set of a closed set is close. From (2.12) it is clear that $U(q)$ is bounded from below by $\frac{1}{2}\lambda_{\min}(P)M_2^2 - M_1$ and C bounds it from above. Since the image of $U(q)$ is a close set the source set of q is close. We proved that Q_C is a bounded close set and therefore compact. \square

Theorem 3 (Existence of connected sub level set of compact function) *Let a function $f(x) : \mathbb{R}^n \mapsto \mathbb{R}$ be a compact function, and let $X_C = \{x : f(x) \leq C\}$ be a sub level set of $f(x)$, Then there exist $C = C^*$ such that for any $C \geq C^*$ X_C is a connected compact set.*

Proof: By definition (2) for any $C > C^* > C_0$ X_C is compact. Denote all the connected subsets of X_C X_i for $i = 1, 2, \dots, N$. X_i is a connected compact set. By it's own definition X_i is connected. X_i is bounded as being a subset of a bounded set. X_i is a closed set because of the following reasons. There is no continuous path that belong to X_C and connect any $x_i \in X_i$ to any $x_j \in X_j$ otherwise X_i and X_j would be unite to one subset of X_C . Thus X_j cannot close an open set X_i and since $X_C = \bigcup_{i=1}^N X_i$ X_i must be a closed set. Denote $x_i^m \in X_i$ as

$$x_i^m = \arg \min_{x \in X_i} f(x).$$

Define a segment $\Gamma_{ij}(t) : [0, 1] \mapsto \mathbb{R}^n$ such that $\Gamma_{ij}(0) = x_i^m$ and $\Gamma_{ij}(1) = x_j^m$. In other words Γ_{ij} is a continuous path connecting x_i^m to x_j^m and as such is a compact set of points. In a compact set continuous function accept a minimum and maximum values. Therefore the maximal value of $f(x)$ along the path $\Gamma_{ij}(t)$ is

$$C_{ij} = \max_{t \in [0, 1]} f(\Gamma_{ij}(t)).$$

If $C \geq C_{ij}$ then the entire path Γ_{ij} is within X_C and there is a connection between X_i and X_j . Finally, if

$$C^* = \max_{i, j} C_{ij}$$

then for $C \geq C^*$ there is a path connecting any X_i to any X_j and X_C is a connected compact set. \square

According to lemma (2.4.3) and to theorem (3) there exists C^* for which the set $Q_C = \{q : U(q) \leq C^*\}$ is a connected compact set.

Lemma 2.4.4 (Existence of cylinder within a sub level set of $U(q)$) *Let $U(q)$ be as in (2.9), and let $Q_L = \{q : U(q) \leq C_L\}$ such that Q_L is a connected compact set*

that contains all the critical points of $U(q)$. Then for large enough C_L , $R'(C_L) > 0$, and there exist $d \in \mathbb{R}^2$ such that $\{q = (d, \theta) : \theta \in [0, 2\pi] \text{ and } \|d\|^2 \leq R'\} \subset Q_L$.

Proof: We follow the first steps of lemma 2.4.3 to get

$$U(q) \leq \frac{1}{2} \lambda_{\max}(P) (\|d + P^{-1}V_\theta\|)^2 + M_3.$$

All the (d, θ) points for which $\frac{1}{2} \lambda_{\max}(P) (\|d + P^{-1}V_\theta\|)^2 + M_3 \leq C_L$ are within Q_L . From the triangle inequality $\|w_1\| - \|w_2\| \leq \|w_1 + w_2\| \leq \|w_1\| + \|w_2\|$ we have

$$\frac{1}{2} \lambda_{\max}(P) (\|d\| + \|P^{-1}V_\theta\|)^2 + M_3 \leq C_L.$$

Substituting the bound for $\|P^{-1}V_\theta\| \leq M_4$ yields

$$\frac{1}{2} \lambda_{\max}(P) (\|d\| + M_4)^2 + M_3 \leq C_L.$$

Isolating $\|d\|$ yields

$$\|d\| \leq \sqrt{\frac{2(C_L - M_3)}{\lambda_{\max}(P)}} - M_4 \equiv R'$$

For C_L large enough $R'(C_L) > 0$ and the cylinder of radius R' is within the C_L sub level set of $U(q)$. Additionally, if q_1, \dots, q_4 are the critical points of $U(q)$ then set $C_L > \max\{U(q_1), \dots, U(q_4)\}$ to contain q_1, \dots, q_4 within Q_L . \square

Proposition 2.4.5 (Equilibria classification) *Let $U(q)$ be as in (2.9), and let $Q_L = \{q : U(q) \leq C_L\}$ as in lemma 2.4.4. Then $U(q)$ has 2 or 4 critical points that can be classified as follows:*

In case $U(q)$ has 2 equilibria:

- $U(q)$ has 1 minimum and 1 saddle.

In case $U(q)$ has 4 equilibria:

- $U(q)$ has 1 minimum and 3 unstable points.
- $U(q)$ has 2 minima and 2 saddle points.

Proof: To prove this proposition we need to use the Morse theory. We assume $U(q)$ is Morse function meaning all its critical points are not degenerate $D^2U(q) \neq 0$ in all the critical points. Thus all critical points of $U(q)$ are discrete and separated from each other. Morse theory can be applied on a compact differentiable manifold. This is the reason we proved Q_L is a compact connected set (lemma 2.4.3 and theorem 3).

Now we review the relevant parts of Morse theory. Morse theorem (part A) [44, page 4]: as C varies within the open interval between two adjacent critical values the topological type of Q_C remain constant.

The definition of Morse data for a function $U(q)$ at a critical point q_i in Q_L is a pair of topological spaces (A, B) where $B \subset A$ with the property that as C crosses the critical value $U(q_i)$, the changes in Q_C topology can be described as gluing in A along B .

Morse theorem (part B) [44, page 4]: Let $U(q)$ be a Morse function on a smooth manifold Q_L Morse data measuring the topological change in Q_C as C crosses the critical value $U(q_i)$ of the critical point q_i is given by the "handle" $(D^\lambda \times D^{n-\lambda}, (\partial D^\lambda) \times D^{n-\lambda})$, where λ is the number of negative eigenvalues of the Hessian matrix of $U(q_i)$, and n is the dimension of Q_L .

Here D^i denotes the closed i -dimensional disk and ∂^i denotes its boundary $i - 1$ sphere. (Note that 0-disk is a point and its boundary is empty).

The Morse data of $U(q)$ is as follows:

Critical point	Morse data (A, B) and its graphical description
minimum	$(D^0 \times D^3, \partial D^0 \times D^3) = \left(\begin{array}{c} \text{circle with dot} \\ \text{circle with slash} \end{array} \right)$
saddle with 1 negative eigenvalue	$(D^1 \times D^2, \partial D^1 \times D^2) = \left(\begin{array}{c} \text{cylinder} \\ \text{disk with dot} \end{array} \right)$
saddle with 2 negative eigenvalue	$(D^2 \times D^1, \partial D^2 \times D^1) = \left(\begin{array}{c} \text{cylinder} \\ \text{cylinder} \end{array} \right)$
maximum	$(D^3 \times D^0, \partial D^3 \times D^0) = \left(\begin{array}{c} \text{circle with dot} \\ \text{circle with dot} \end{array} \right)$

Q_L is a connected compact set without any pinching since it contains a cylinder. We wish to find a combination of critical points that forms a set with same topological characteristics as those of Q_L . Note that our space is (x, y, θ) , where $x \in \mathbb{R}$ and $y \in \mathbb{R}$ are linear coordinations, while θ is a cyclic coordination. One can imagine this space as a surface of a cylinder with one extra linear coordinate.

Q_L must contain a minimum point of $U(q)$ since a continuous function accepts a minimum and maximum values in a compact set. Moreover, the minimum point is inside Q_L while the maximum is on its boundary. Note that $U(q) = C_L$ on the boundary of Q_L . Thus if the minimum point is on the boundary it means that $U(q) = \text{const.}$ and this is impossible.

Generally, if we have only one minimum point of $U(q)$ then except of a very thin set flows, all the other flows will converge to the minimum of $u(q)$. Note that every small perturbation will cause the system to leave this set and to converge to the minimum.

In case $U(q)$ has 2 critical points there exist only one minimum since If we have 2 minima points we end with 2 disconnected 3D balls and this is not equivalent to the topology of Q_L .

In case $U(q)$ has 4 critical points, Q_L can not contain 3 minima points. The reason for this is that the topology of 3 minima points is 3 disconnected balls, but we have a connected set, Thus we need a "handle" with 3 gluing surfaces which we do not have.

We conclude that $U(q)$ can have 1 or 2 minima points. In case $U(q)$ have 4 critical points with two minima points we still need to characterize the other two critical points. According to the mountain pass theorem [48, 54] and the saddle point theorem between two minima points there exist a saddle point. So now we have two minima points and a saddle. Since θ is acyclic coordinate and since Q_L contain a cylinder in the full range of θ , there exist another saddle between the two minima in the other way around θ . \square

In case there are two minima points in Q_L and two saddle points. Denote the two minima points as q_1^* , q_2^* and the two saddle points as q_1^s , q_2^s . We can order the points in a way that $\theta_1^s < \theta_1^* < \theta_2^s < \theta_2^*$. The following proposition states which points are within the basin of attraction of q_1^* .

Proposition 2.4.6 (Basin of attraction) *Let $U(q)$ be as in (2.9), and let $Q_L = \{q : U(q) \leq C_L\}$ as in lemma 2.4.4. For the case $U(q)$ has 2 minima points and 2 saddle points. A point q_0 is within the basin of attraction of q_1^* if:*

- $U(q_0) < \min[U(q_1^s), U(q_2^s)]$
- $\theta_1^s < \theta_0 < \theta_2^s$

Proof: The first item states that the system initial energy must be lower then the lowest saddle. The sub level set is a positive invariant set and the flow can not move the state between disjoint subsets of the sub level set. This assures that the system will stay within the basin of attraction of q_1^* and will not have enough "energy" to

pass to the basin of attraction of q_2^* . The second item states that the plane $\theta = \theta_{saddle}$ separates between the two basins of attraction of the two minima points. To prove that we suppose $\theta = \theta_{saddle}$ is not a separating plane and will see that this lead to a contradiction to lemma 2.4.2. The saddle point q^s is both on the $\theta = \theta_{saddle}$ plane and on $U(q) = U(q^s)$ manifold. Thus according to lemma 2.4.2 the intersection of the manifold and the plane is the isolated point q^s or an ellipse that contains q^s on its boundary. But if the $\theta = \theta_{saddle}$ is not the separating plane it necessarily intersect both the two basins of attraction. Following it is impossible that the intersection between the plane $\theta = \theta_{saddle}$ and the manifold $U(q) = U(q^s)$ to be a unique ellipse rather it must be two tangent sets, and the tangent point suppose to be q^s . We get a contradiction to lemma 2.4.2 and we conclude that the plane $\theta = \theta_{saddle}$ is a separating plane and it's intersection point with the manifold $U(q) = U(q^s)$ is the unique point q^s . \square

2.4.3 Convergence Point Algorithm

Concluding the analysis of the equilibria points we have the following algorithm that uniquely define to which point the system converges from a given initial configuration point $q_0 = (d_0, \theta_0)$.

Basin of Attraction Algorithm:

Input: Initial configuration q_0 , and external wrench w_{ext} applied on \mathcal{B} .

Output: Stable equilibrium point which \mathcal{B} converges to $q^*(w_{ext}, q_0)$.

Algorithm:

1. Solve (2.8) to find the θ values of the equilibrium points.
2. Normalize all the θ_i such that $0 \leq \theta_i < 2\pi$.

3. Substitute all the θ_i into (2.7) to find the entire q_i configurations of the equilibrium points.
4. Compute $D^2U(q_i)$ for all the q_i .
5. If $D^2U(q_i) > 0$ for only one $i = i^*$ then assign $q^* = q_{i^*}$ and exit.
6. Identify θ_1^* and θ_2^* with the corresponding q_1^* and q_2^* for which $D^2U(q_i^*) > 0$.
7. Identify θ_1^s and θ_2^s with the corresponding q_1^s and q_2^s for which $D^2U(q_i^s) < 0$.
8. If $U(q_0) \geq \min[U(q_1^s), U(q_2^s)]$ then exit "the algorithm can not define uniquely to which equilibrium point the system converges".
9. Order the critical points such that $\theta_1^s < \theta_2^s$ and $\theta_1^* < \theta_2^*$.
10. If $\theta_1^s < \theta_0 < \theta_2^s$ then if $\theta_1^s < \theta_i^* < \theta_2^s$ assign $q^* = q_i^*$ and exit. Else
 - (a) If $\theta_1^s + 2\pi > \theta_0 > \theta_2^s$ then if $\theta_1^s + 2\pi > \theta_i^* > \theta_2^s$ assign $q^* = q_i^*$ and exit.
 - (b) If $\theta_1^s > \theta_0 > \theta_2^s - 2\pi$ then if $\theta_1^s > \theta_i^* > \theta_2^s - 2\pi$ assign $q^* = q_i^*$ and exit.

The importance of the above algorithm is that it allow us to uniquely calculate the point q^* for a given external wrench w_{ext} . Note that this algorithm is simply a description of an analytical function. Finally, we can write the force closure stability set as

$$\mathcal{W}_{global} = \{w_{ext} : 0 \leq F_i^t(q^*(w_{ext})) < \mu F_i^n(q^*(w_{ext})) \text{ for } i = 1 \dots k\}$$

2.5 Force Closure Set for Curved Fingers

In this section we relax the sharp pointed finger assumption and allow the fingers to be curved in the vicinity of the contact point. This also allow rolling motion between

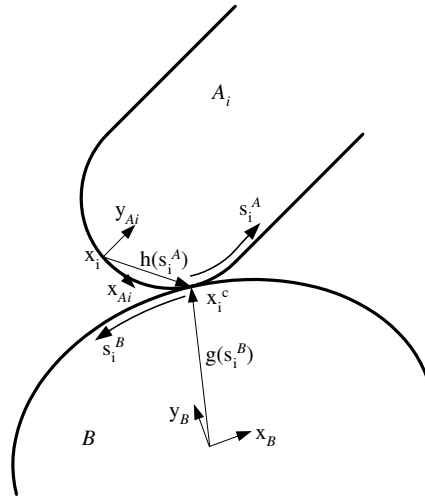


Figure 2.3: Schematic view of rolling motion between the i^{th} finger and the object.
 תרשים סכימטי של תנועת הגלגול בין אצבע i לאובייקט.

the object and each finger.

2.5.1 Problem Statement and Mathematical Representation

As in the previous section we use a linear control law such that the finger apply a force

$$F_i = F_i^0 - K_i(x_i - x_i^0) \quad (2.13)$$

However, now this force is applied in a point called *control point* which is located on the tip of the finger where the designed contact point is located. The control point is stationary relative to the finger. Additionally the object frame origin is located at the control point (figure 2.3).

Since the fingers can roll on the object boundary we have additional k degrees of freedom. For the stability matter we need to express $F_i(x_i)$ as function of these $3 + k$ degrees of freedom.

Denote the i^{th} finger orientation α_i . We parameterize the object and the finger boundary curves with the length parameters $s_i^{\mathcal{B}}$ and $s_i^{\mathcal{A}}$ respectively. In this parameterization $g_i(s_i^{\mathcal{B}})$ is a vector from the object origin to the boundary of \mathcal{B} near the i^{th} contact point. Note that the parameters are in opposite directions to be consistent with the rolling direction. For example in figure (2.3) $s_i^{\mathcal{A}}$ and $s_i^{\mathcal{B}}$ parameterize the boundaries of the object and the fingers in contra-clock-wise direction. $h_i(s_i^{\mathcal{A}})$ is a vector from the i^{th} finger control point x_i to the contact point with \mathcal{B} x_i^c . The i^{th} contact point location relative to a stationary frame is given by

$$x_i^c = R(\theta)g_i(s_i^{\mathcal{B}}) + d,$$

and the control point, x_i , location in this frame is

$$x_i = x_i^c - R(\phi_i)h_i(s_i^{\mathcal{A}}). \quad (2.14)$$

Substitution of x_i^c into (2.14) yields

$$x_i = R(\theta)g_i(s_i^{\mathcal{B}}) + d - R(\phi_i)h_i(s_i^{\mathcal{A}}). \quad (2.15)$$

Rolling contact constraints: In order to have a contact between the i^{th} finger and the object we demand

$$v_i^n \equiv 0, \quad \forall i$$

where v_i^n is the difference between \mathcal{B} 's and the i^{th} finger velocities in the normal direction.

Since there exist a point contact between the finger and the object we have the following two constraints. In the first constraint we assume to have a no slippage contact. This will later on be justified by demanding $F_i \in FQ_i$. Thus, denote

$$s_i \equiv s_i^{\mathcal{B}} = -s_i^{\mathcal{A}}. \quad (2.16)$$

The second constraint states that at the contact point, the tangent vector to the boundary of the finger is identical to the tangent vector to the boundary of the object. This means that

$$R(\theta)g'_i(s_i^B) = R(\phi_i)h'_i(-s_i^A), \quad (2.17)$$

where $(\cdot)'_i = \frac{\partial}{\partial s_i}(\cdot)$. Since the parameterizations $g_i(s_i^B)$ and $h'_i(s_i^A)$ are *uniform parameterizations* therefore $\|g'_i(s_i^B)\| = \|h'_i(s_i^A)\| = 1$. It is possible to solve (2.17) for

$$\begin{aligned} \cos(\phi_i) &= h_i'^T R(\theta)g'_i \\ \sin(\phi_i) &= h_i'^T J R(\theta)g'_i, \end{aligned}$$

where $J = \begin{bmatrix} 0 & 1 \\ -1 & 0 \end{bmatrix}$ and $h'_i = h'_i(-s_i)$. One can check that indeed $\cos^2(\phi_i) + \sin^2(\phi_i) = 1$. Now we can express $R(\phi_i)$ as function of θ and s_i as

$$R(\phi_i) = \begin{bmatrix} h_i'^T R(\theta)g'_i & -h_i'^T J R(\theta)g'_i \\ h_i'^T J R(\theta)g'_i & h_i'^T R(\theta)g'_i \end{bmatrix}.$$

For simplicity we define a new variable

$$\rho_i(\theta, s_i) = R(\theta)g_i - R(\phi_i)h_i,$$

which is the vector connecting the object origin to the finger's initial contact point (where the compliant law force act). This let us write

$$x_i(q, s_i) = \rho_i(\theta, s_i) + d.$$

The roll potential energy: The total roll potential energy $U(q, s_1, \dots, s_k)$ is

$$U(q, s_1, \dots, s_k) = \frac{1}{2} \sum_{i=1}^k [(x_i - x_i^0)^T K_i (x_i - x_i^0) - x_i^T F_i^0] - q^T w_{ext}. \quad (2.18)$$

Lemma 2.5.1 (Derivatives of $U(q)$) *Let $U(q)$ as in (2.18) Then it's first derivative is given by*

$$DU(q, s_1, \dots, s_k) = - \sum_{i=1}^k Dx_i^T(q, s_1, \dots, s_k) F_i(q, s_1, \dots, s_k),$$

and it's second derivative is

$$D^2U(q, s_1, \dots, s_k) = \sum_{i=1}^k \begin{pmatrix} K_i & -K_i J \rho_i & \cdots & K_i \rho'_i & \cdots \\ \rho_i^T J K_i & (J \rho_i)^T K_i (J \rho_i) + \rho_i^T F_i & \cdots & \rho_i^T J K_i \rho'_i + (J \rho'_i)^T F_i & \cdots \\ \vdots & \vdots & \ddots & \vdots & \vdots \\ \rho_i'^T K_i & \rho_i'^T K_i J \rho_i + (J \rho'_i)^T F_i & \cdots & \rho_i'^T K_i \rho'_i - \rho_i''^T F_i & \cdots \\ \vdots & \vdots & \cdots & \vdots & \vdots \end{pmatrix}.$$

Proof: A straight forward derivation of $U(q, s_1, \dots, s_k)$ yields

$$DU(q, s_1, \dots, s_k) = - \sum_{i=1}^k Dx_i^T(q, s_1, \dots, s_k) F_i(q, s_1, \dots, s_k).$$

The second derivative of $U(q, s_1, \dots, s_k)$ is

$$D^2U(q, s_1, \dots, s_k) = \sum_{i=1}^k Dx_i^T(q, s_1, \dots, s_k) K_i Dx_i^T(q, s_1, \dots, s_k) - D^2x_i^T(q, s_1, \dots, s_k) F_i(q, s_1, \dots, s_k).$$

Next we compute the first and second derivatives of $x_i(q, s_i) = \rho_i(\theta, s_i) + d$. The first derivative is

$$Dx_i(q, s_i) = [I_{2 \times 2} ; -J \rho_i ; \rho'_i].$$

For computing $D^2x_i(q, s_i)$ we compute the derivative of $Dx_i^T(q, s_i) F_i$ while holding F_i constant. Thus we have

$$Dx_i^T(q, s_i) F_i = \begin{pmatrix} F_i \\ -(J \rho_i)^T F_i \\ \rho_i'^T F_i \end{pmatrix}.$$

Computing $D[Dx_i^T(q, s_i)F_i]$ when F_i is constant yields

$$D^2x_i^T(q, s_i)F_i = \begin{pmatrix} 0_{2 \times 2} & 0_{2 \times 1} & 0_{2 \times 1} \\ 0_{1 \times 2} & -\rho_i^T F_i & -(J\rho_i')^T F_i \\ 0_{1 \times 2} & -(J\rho_i')^T F_i & \rho_i''^T F_i \end{pmatrix}.$$

The first term in $D^2U_i(q, s_i)$ is

$$Dx_i^T(q, s_i)K_iDx_i^T(q, s_i) = \begin{pmatrix} K_i & -K_iJ\rho_i & K_i\rho_i' \\ \rho_i^T JK_i & (J\rho_i)^T K_i(J\rho_i) & \rho_i^T JK_i\rho_i' \\ \rho_i'^T K_i & \rho_i'^T K_iJ\rho_i & \rho_i'^T K_i\rho_i' \end{pmatrix}.$$

Combining the two terms to construct $D^2U_i(q, s_i)$ yields

$$D^2U_i(q, s_i) = \begin{pmatrix} K_i & -K_iJ\rho_i & K_i\rho_i' \\ \rho_i^T JK_i & (J\rho_i)^T K_i(J\rho_i) + \rho_i^T F_i & \rho_i^T JK_i\rho_i' + (J\rho_i')^T F_i \\ \rho_i'^T K_i & \rho_i'^T K_iJ\rho_i + (J\rho_i')^T F_i & \rho_i'^T K_i\rho_i' - \rho_i''^T F_i \end{pmatrix}.$$

Summing $D^2U_i(q, s_i)$ over the k fingers gives

$$D^2U(q, s_1, \dots, s_k) = \sum_{i=1}^k \begin{pmatrix} K_i & -K_iJ\rho_i & \cdots & K_i\rho_i' & \cdots \\ \rho_i^T JK_i & (J\rho_i)^T K_i(J\rho_i) + \rho_i^T F_i & \cdots & \rho_i^T JK_i\rho_i' + (J\rho_i')^T F_i & \cdots \\ \vdots & \vdots & \ddots & \vdots & \vdots \\ \rho_i'^T K_i & \rho_i'^T K_iJ\rho_i + (J\rho_i')^T F_i & \cdots & \rho_i'^T K_i\rho_i' - \rho_i''^T F_i & \cdots \\ \vdots & \vdots & \cdots & \vdots & \vdots \end{pmatrix}.$$

□

2.5.2 Initial Equilibrium Point with Rolling

We show that an equilibrium point of grasping system with pointed sharp finger is still an equilibrium point even if we replace the sharp fingers with curved ones. This is not trivial since we add k DOF to the dynamic system.

Lemma 2.5.2 (Equilibrium point) *If q^* is an equilibrium point of the grasping system with pointed sharp fingers, Then $(q^*, 0, \dots, 0)$ is an equilibrium point for the grasping system with curved fingers (i.e. when the rolling parameters s_i vanish).*

Proof: In equilibrium point

$$DU(q, s_1, \dots, s_k) = - \sum_{i=1}^k \begin{pmatrix} F_i \\ -(J\rho_i)^T F_i \\ \rho_1^T F_i \\ \vdots \\ \rho_k^T F_i \end{pmatrix} = 0.$$

Thus we need to evaluate ρ_i and ρ'_i for $s_i = 0$. Note that $h_i(s_i = 0) = 0$. Therefore when evaluating $\rho_i(\theta_i, s_i) = R(\theta)g_i(s_i) - R(\phi_i)h(s_i)$ for $s_i = 0$ we get $\rho_i(\theta_i, 0) = R(\theta)g_i(s_i)$. Similarly $\rho'_i = -R'(\phi_i)h_i$ becomes $\rho'_i(\theta, 0) = \mathbf{0}$. For that reason all the k last rows of $DU(q, s_1, \dots, s_k)$ vanish. The first two rows becomes

$$DU(q) = - \sum_{i=1}^k \begin{pmatrix} F_i \\ R(\theta)g_i(0) \times F_i \end{pmatrix}.$$

which is exactly the conditions for q to be an equilibrium point when the fingers are sharp and therefore vanish when $q = q^*$ and $s_i = 0$ for $i = 1, \dots, k$. \square

Note that there are only two forces applied on each finger. The first force is the compliance law force which act in the initial contact point. The second force is the contact force applied in the contact point. In order the finger to be in equilibrium these forces have to act along the same line of action in the same magnitude in different directions. The condition for the forces to act along the same line can be phrased as $\rho'_i \cdot F_i = 0$. (The physical meaning of ρ' is presented in the next sub

section.) Thus the conditions for an equilibrium point are

$$\begin{aligned}\sum_{i=1}^k F_i &= w_{ext} \\ \sum_{i=1}^k R(\theta)g_i(s_i) \times F_i &= \tau_{ext} \\ \rho'_i \cdot F_i &= 0 \text{ for } i = 1, \dots, k.\end{aligned}$$

The solution of these $k + 3$ equations is a set of equilibria points $(x, y, \theta, s_1, \dots, s_k)$.

2.5.3 Rolling Stability of Equilibrium Point

Here we examine the stability property of the $(q^*, 0, \dots, 0)$ equilibrium point.

Theorem 4 (Equilibrium stability) *If q^* is a stable equilibrium point of the grasping system with pointed sharp fingers then $(q^*, 0, \dots, 0)$ is locally stable equilibrium point of the grasping system with curved fingers.*

Proof: In order to prove the proposition we need to show that $F_i \in FQ_i$ for $i = 1, \dots, k$ and that $D^2U(q, s_1, \dots, s_k)$ is positive definite in the $(q^*, 0, \dots, 0)$ point. The proposition states that q^* is a stable equilibrium point of the grasping system with pointed sharp fingers. Thus, $F_i \in FQ_i$ for $i = 1, \dots, k$. Evaluating $D^2U(q, s_1, \dots, s_k)$ at $(q^*, 0, \dots, 0)$ yields

$$D^2U(q^*, 0, \dots, 0) = \sum_{i=1}^k \begin{pmatrix} K_i & -K_i J \rho_i & \cdots & 0 & \cdots \\ \rho_i^T J K_i & (J \rho_i)^T K_i (J \rho_i) + \rho_i^T F_i & \cdots & 0 & \cdots \\ \vdots & \vdots & \ddots & \vdots & \vdots \\ 0 & 0 & \cdots & -\rho_i'^T F_i & \cdots \\ \vdots & \vdots & \cdots & \vdots & \vdots \end{pmatrix}.$$

The upper left 3×3 sub matrix of $D^2U(q^*, 0, \dots, 0)$ is simply the $D^U(q^*)$ matrix of the grasping system with pointed sharp fingers. Since we know that q^* is a stable equilibrium point of this system then $D^U(q^*)$ is positive definite. Therefor the condition

for the matrix $D^2U(q^*, 0, \dots, 0)$ to be positive definite is that the term $-\rho_i''^T F_i^0 > 0$ for $i = 1, \dots, k$.

Next we investigate the term $-\rho_i''^T F_i$. The derivatives of ρ_i with respect to s_i are

$$\begin{aligned}\rho_i' &= R(\theta)g_i' - R(\phi_i)h_i' - R'(\phi_i)h_i = -R'(\phi_i)h_i \\ \rho_i'' &= -R''(\phi_i)h_i - R'(\phi_i)h_i'.\end{aligned}$$

In order to have better understanding of the physical meaning of ρ_i'' we need to find the meaning of $R'(\phi_i)$. Specifically,

$$R'(\phi_i) = \begin{bmatrix} h_i''^T R(\theta)g_i' & -h_i''^T JR(\theta)g_i' \\ h_i''^T JR(\theta)g_i' & h_i''^T R(\theta)g_i' \end{bmatrix} + \begin{bmatrix} h_i'^T R(\theta)g_i'' & -h_i'^T JR(\theta)g_i'' \\ h_i'^T JR(\theta)g_i'' & h_i'^T R(\theta)g_i'' \end{bmatrix}. \quad (2.19)$$

For general curve we have $h'' \cdot h' = 0$ $g'' \cdot g' = 0$ since we use a uniform parameterization.

If we assume that the fingers and the object have locally arc shape bounding curve and if we assume the following radii of curvature,

$$\begin{aligned}\text{finger radius of curvature at the } i^{\text{th}} \text{ contact point} &= \frac{1}{\alpha_i} \\ \text{object radius of curvature at the } i^{\text{th}} \text{ contact point} &= \frac{1}{\beta_i}\end{aligned}$$

then

$$\begin{aligned}h_i''(s_i) &= -\alpha_i Jh_i'(s_i) \\ g_i''(s_i) &= \beta_i Jg_i'(s_i)\end{aligned}$$

Substituting $h_i''(s_i)$ and $g_i''(s_i)$ back to (2.19) yields

$$R'(\phi_i) = \begin{bmatrix} -\alpha_i (Jh_i')^T R(\theta)g_i' & \alpha_i (Jh_i')^T JR(\theta)g_i' \\ -\alpha_i (Jh_i')^T JR(\theta)g_i' & -\alpha_i (Jh_i')^T R(\theta)g_i' \end{bmatrix} + \begin{bmatrix} \beta_i h_i'^T R(\theta)Jg_i' & -\beta_i h_i'^T JR(\theta)Jg_i' \\ \beta_i h_i'^T JR(\theta)Jg_i' & \beta_i h_i'^T R(\theta)Jg_i' \end{bmatrix}.$$

Simplifying $R'(\phi_i)$ with the following identities, $JR(\theta) = R(\theta)J$, $JR(\theta)J = -R$ and $J^T = -J$, results with

$$R'(\phi_i) = \begin{bmatrix} \alpha_i \sin(\phi_i) & \alpha_i \cos(\phi_i) \\ -\alpha_i \cos(\phi_i) & \alpha_i \sin(\phi_i) \end{bmatrix} + \begin{bmatrix} \beta_i \sin(\phi_i) & \beta_i \cos(\phi_i) \\ -\beta_i \cos(\phi_i) & \beta_i \sin(\phi_i) \end{bmatrix}.$$

Which is $\alpha_i JR(\phi_i) + \beta_i JR(\phi_i)$. Therefore we have

$$R'(\phi_i) = (\alpha_i + \beta_i)JR(\phi_i). \quad (2.20)$$

Recall that $\rho_i'' = -R''(\phi_i)h_i - R'(\phi_i)h_i'$ and for $s_i = 0$, h_i vanish so we have $\rho_i'' = -R'(\phi_i)h_i'$. Additionally, from (2.20) we have $R'(\phi_i) = (\alpha_i + \beta_i)JR(\phi_i)$. Substituting these terms to $-\rho_i''^T F_i^0$ yields $-\rho_i''^T F_i = (\alpha_i + \beta_i)(JR(\phi_i)h_i')^T F_i^0$. Thus the stability condition becomes

$$(\alpha_i + \beta_i)(JR(\phi_i)h_i')^T F_i^0 > 0 \text{ for } i = 1, \dots, k$$

The $JR(\phi_i)h_i'$ vector is a unit vector pointing into \mathcal{B} . Thus, $(JR(\phi_i)h_i')^T F_i^0$ is the compressing part of F_i^0 since F_i^0 must be a compressing force and not a tension force. Therefore in general $(JR(\phi_i)h_i')^T F_i^0$ is positive. For a convex object ($\beta > 0$) and convex fingers ($\alpha_i > 0$) The system will be locally stable if it was stable for sharp fingers. Figure 2.4 show that the control force together with the contact force produce restoring torque. Then the fingers converge to their original state where the initial contact point contacting the object. In case the finger is concave ($\alpha_i < 0$) the object must be convex ($\beta > 0$). In this case the size of the radius of curvature of \mathcal{B} must be smaller or equal to the size of the radius of curvature of \mathcal{A} so ($|\alpha_i| \leq |\beta|$) and $\alpha_i + \beta_i \geq 0$. In case the object is be concave ($\beta < 0$) the finger must be convex ($\alpha_i > 0$), and the size of the radius of curvature of \mathcal{B} must be greater or equal to the size of the radius of curvature of \mathcal{A} so ($|\alpha_i| \geq |\beta|$) and $\alpha_i + \beta_i \geq 0$. Next we show that $\alpha_i + \beta_i = 0$ is almost impossible. In this case the radius of curvature of the finger equals the radius of curvature of the object but one is convex and the second is concave. This case is not practical since it is almost impossible to manufacture two objects with exactly the same radius of curvature. \square

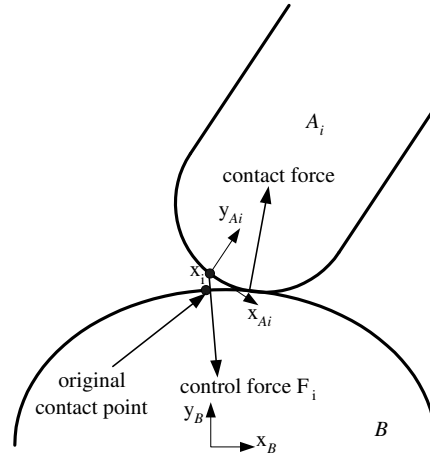


Figure 2.4: Schematic view of the forces applied on the i^{th} finger during roll motion.
 תרשים סכימטי של הכוחות הפועלים על אצבע i במהלך תנועת גילגול.

2.6 Simulations and Experimental Results

This section presents several experiments conducted in order to verify the computed force closure stability set. All experiments involve stability of two fingers grasps. The first experiment presents a set of external wrenches on the boundary of the force closure stability set. The second experiment shows how the preloading forces affect the size of the force closure stability set. First we present the experiments setup.

2.6.1 Experiments Setup

Figure 2.5 shows the apparatus used for the experiments. This apparatus includes two compliant sphere shaped fingers made of aluminum. Each finger can move along horizontal and vertical frictionless linear guides. For the passive compliant of the fingers we use a linear compressible springs. We calculate the springs coefficients from the calibration process shown in figure 2.6. The coefficient of the horizontal springs is

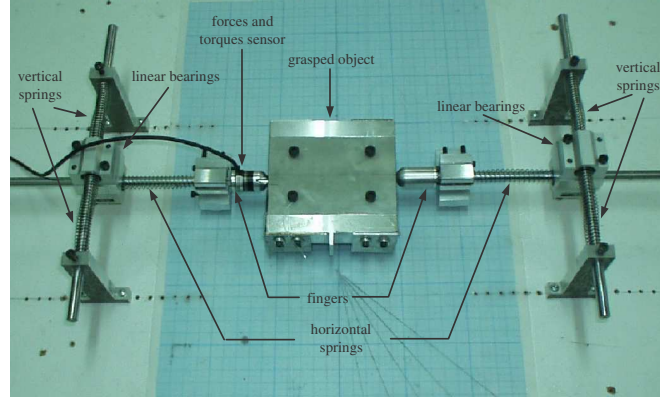


Figure 2.5: The apparatus used for the two-fingered grasp experiments.

מערכת הניסוי לאחיזת דו-אצבעיות

$k_1 = 0.1122[N/mm]$, and the coefficient of the vertical spring is $k_2 = 0.1402[N/mm]$. For measuring the contact forces we use a 6-DOF agile small-size force and torque sensor. The force and torque sensor is used for measuring the preloading forces and for determining the friction coefficient μ between the object and the fingers. The grasp object is a $100mm \times 100mm$ rectangle aluminum piece, coated with high friction material providing $\mu = 0.5$. We attach four rollers to the bottom of the object in order to minimize friction between the object and the supporting table. The wrenches are applied using $50[g]$ weights connected to the object by a string. In the following sections we use $[mm]$ as length units, $[rad]$ for angle units, $[N]$ for force units, and $[N \cdot mm]$ for torque units.

2.6.2 Verifying the Force Closure Stability Set Experiment

In this experiment we apply various external wrenches on the object to determine which wrench causes the object to converge to a stable posture. We then compare

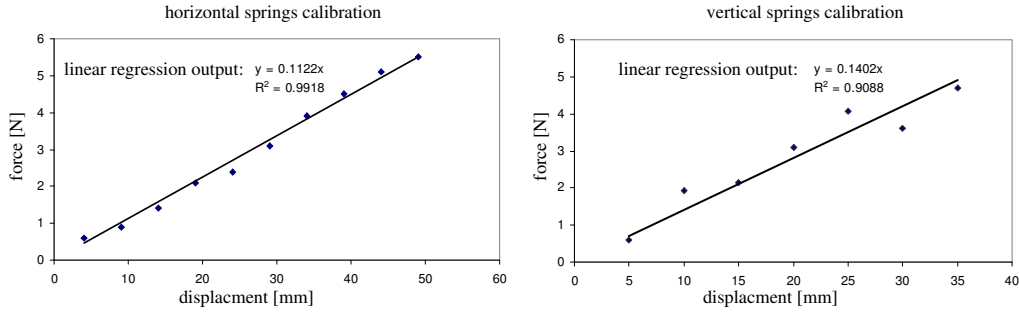


Figure 2.6: The springs calibration. The marked points show the measured points, and the line results from the linear regression.

מדידת קבועי הקפיצים. הנקודות הן המדידות בפועל, והקו הוא תוצאה של רגרסיה לינארית.

these results to the computed force closure stability set. Figure 2.7 shows schematically the point and directions of the applied external forces. In this experiment we use a preloading forces of $F_0 = 5.8[N]$ for each finger. These forces are antipodal and horizontal. For these conditions we calculate both the feasible configurations set and the force closure stability set (figure 2.8). The upper and the lower surfaces of the manifold in figure 2.8 (both in the configuration space and in the wrench space) are associated with the $D^2U(q) > 0$ constraint, while the surfaces of the manifold that bounds the force closure stability set from the sides are associated with the friction cones constraints.

In this experiment we apply forces in different angles. Since the force action line does not pass through the object's frame origin, this force also generates an external torque. We gradually increase this external force until instability occurs. The instability is observed as a slip of the contact points or as a relatively large movement of the object. The results of this experiment are shown as dots in figure 2.9 and are compared to the analytic calculated maximum applicable external force

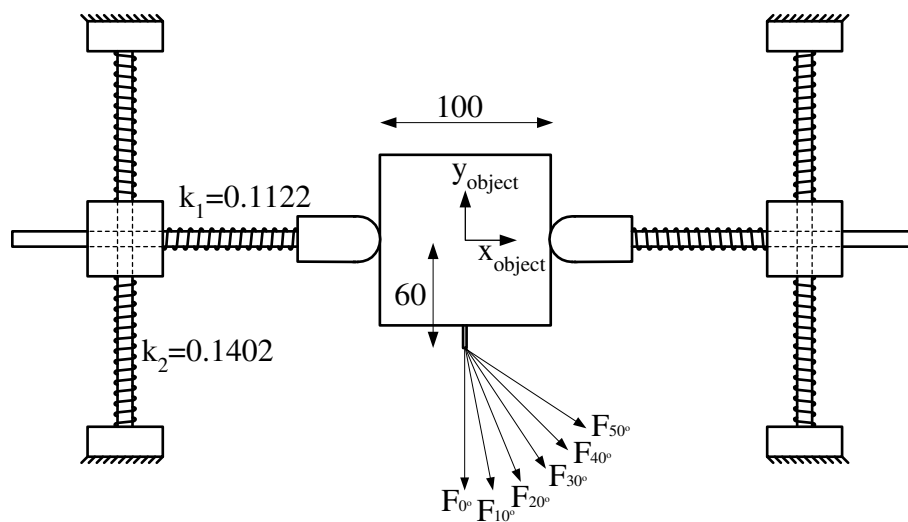


Figure 2.7: Schematic view of the experiment setup that shows how the external forces are been applied to the grasped object.

תרשים סכמטי של מהלך הניסוי המראה את כיווני הפעלת הכוחות על האובייקט.

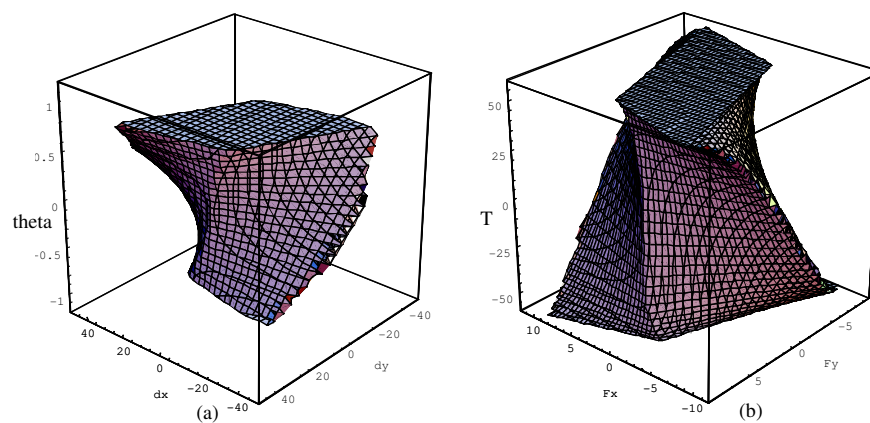


Figure 2.8: (a) The feasible configurations set and (b) the force closure stability set of the first experiment.

(a) קבוצת הקונפיגורציות בהן האובייקט יציב ו-(b) קבוצת סגור הכוחות היציבה עבור הניסוי הראשון.

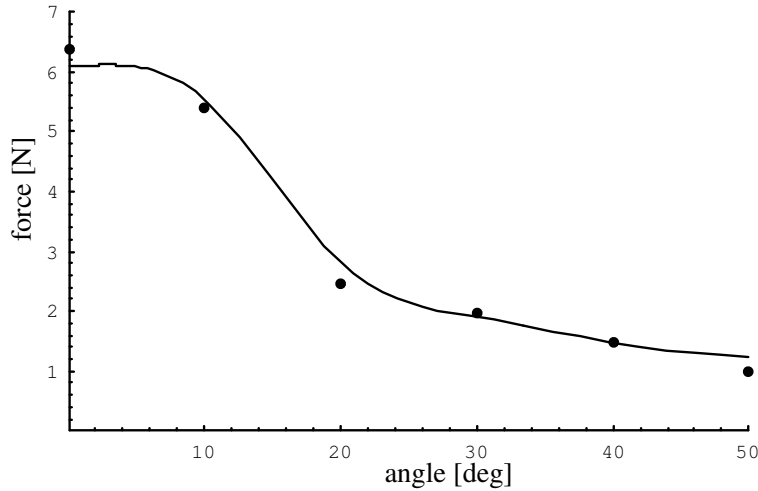


Figure 2.9: For every angle of application the graph shows the maximum applied external force in the force closure stability set. Solid line represent analytic results and the dotted marks represent experimental results.

הכוח המקסימלי הנמצא בקבוצת סגור הכוחות היציבה שניתן להפעיל על האובייקט בכל זווית של הפעלת הכוח. הקו מציין תוצאה אנליטית ואילו הנקודות נמדדו בניסוי.

(the solid curve).

Figure 2.10 presents the wrenches applied in this experiment. For any given angle of external force, the wrench applied on the object increases linearly. Furthermore, as the angle of force increases, the torque component of the wrench becomes dominant. As we use 50 grams weights for the external force we have discrete and finite number of wrenches points. Figure 2.10 shows that all wrenches that cause the object to converge to a stable posture are within or very close to the boundary of the force closure stability set manifold. Increasing the external force beyond the boundary of the force closure stability set causes instability, marked as \times in figure 2.10.

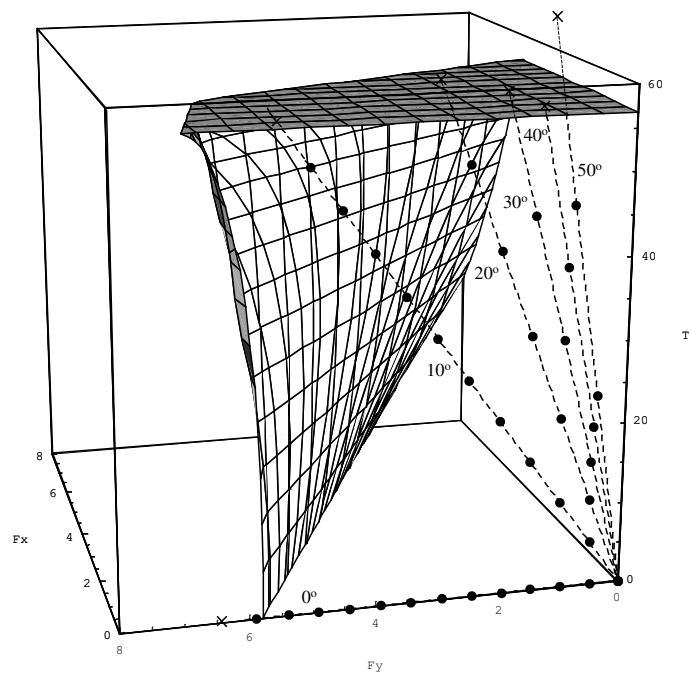


Figure 2.10: The applied external wrenches shown in the wrench space.
הכוחות והמומנטים שהופעלו על האובייקט מוצגים במרחב הכוחות והמומנטים.

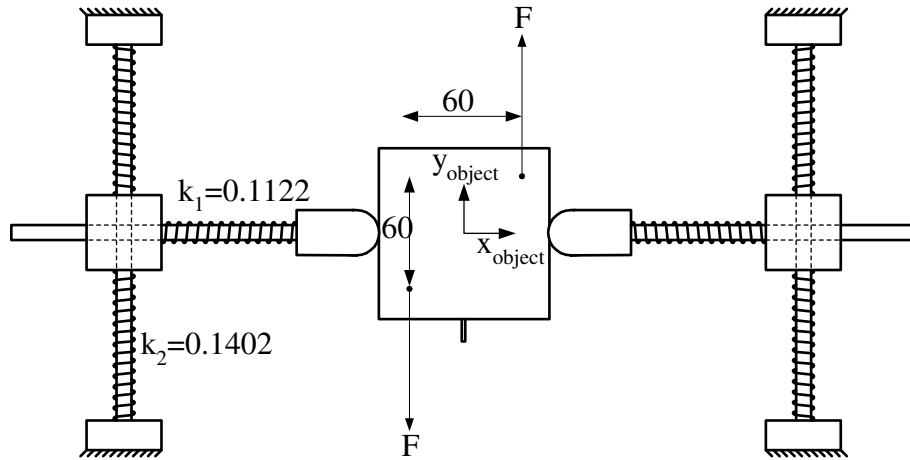


Figure 2.11: Schematic view of the experiment setup that shows how the pure external torque is been applied to the grasped object.
 תרשים סכימטי של מערכת הניסוי המראה כיצד הופעל מומנט טהור על האובייקט האוחז.

2.6.3 The Effect of Preloading Forces on Stability

The objective of the second experiment is to observe the effect of different preloading forces on the size of the force closure stability set. Especially we are interested in the maximal external torque that can be applied on the object without losing stability. When high preloading force is applied, instability occurs since $D^2U(q)$ becomes singular or even negative definite. Instability due to singularity of $D^2U(q)$ involves a rotation of the object since the pure translation part of $D^2U(q)$ is $\sum K_i$ which is always positive definite. Thus we choose to examine the effect of preloading forces on the maximal allowable torque. A schematic view of the apparatus used for this set of experiments is shown in figure 2.11.

For these conditions we calculate the maximal allowable external torque and plot it as a function of the preloading force (the solid curve in figure 2.12). We first set the

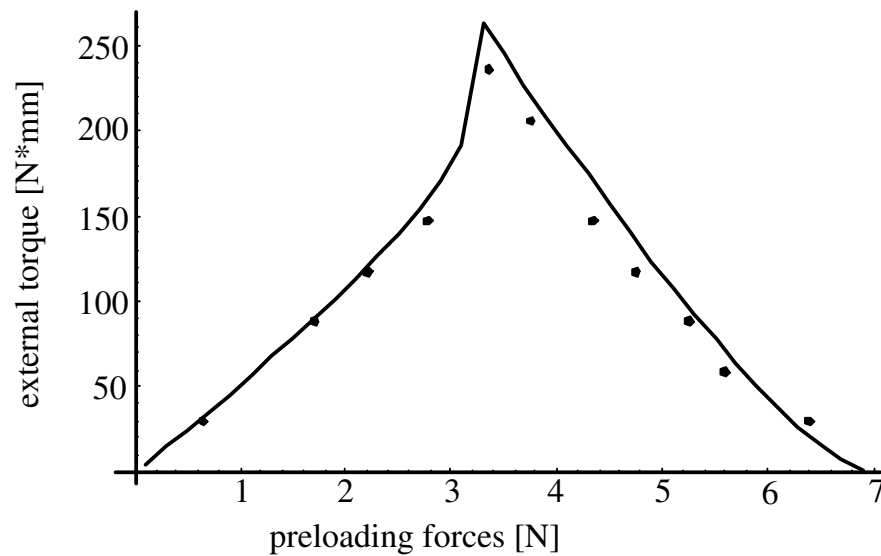


Figure 2.12: The maximal allowable external torque vs. the preloading forces. In solid line is the computed maximal torque, and the marked dots are the experimental measurements.

המומנט החיצוני המקסימלי הניתן להפעלה על האובייקט מול כוח הלחיצה ההתחלתי. הקו מתאר את המומנט המחושב והנקודות מתארות את המומנט שנמדד בניסוי.

amount of preloading force and gradually increase the external torque until instability occurs. We repeat this experiment for various preloading forces. The maximal torque for which the system remained stable in each experiment is plotted as dots in figure 2.12.

The maximal torque curve in figure 2.12 can be divided into two curves. In the first curve (for preloading force between 0.1 to 3.3) the preloading force is relatively small and instability results in a slip at the contacts. In this part of the curve the maximal external torque that can be applied monotonically increases as the preloading force increases. In the second curve (for preloading force between 3.3 to 6.9) the preloading force is relatively high and no slippage occurs at contacts. Instead, instability occurs when the object severely rotates. The maximal external force that can be applied,

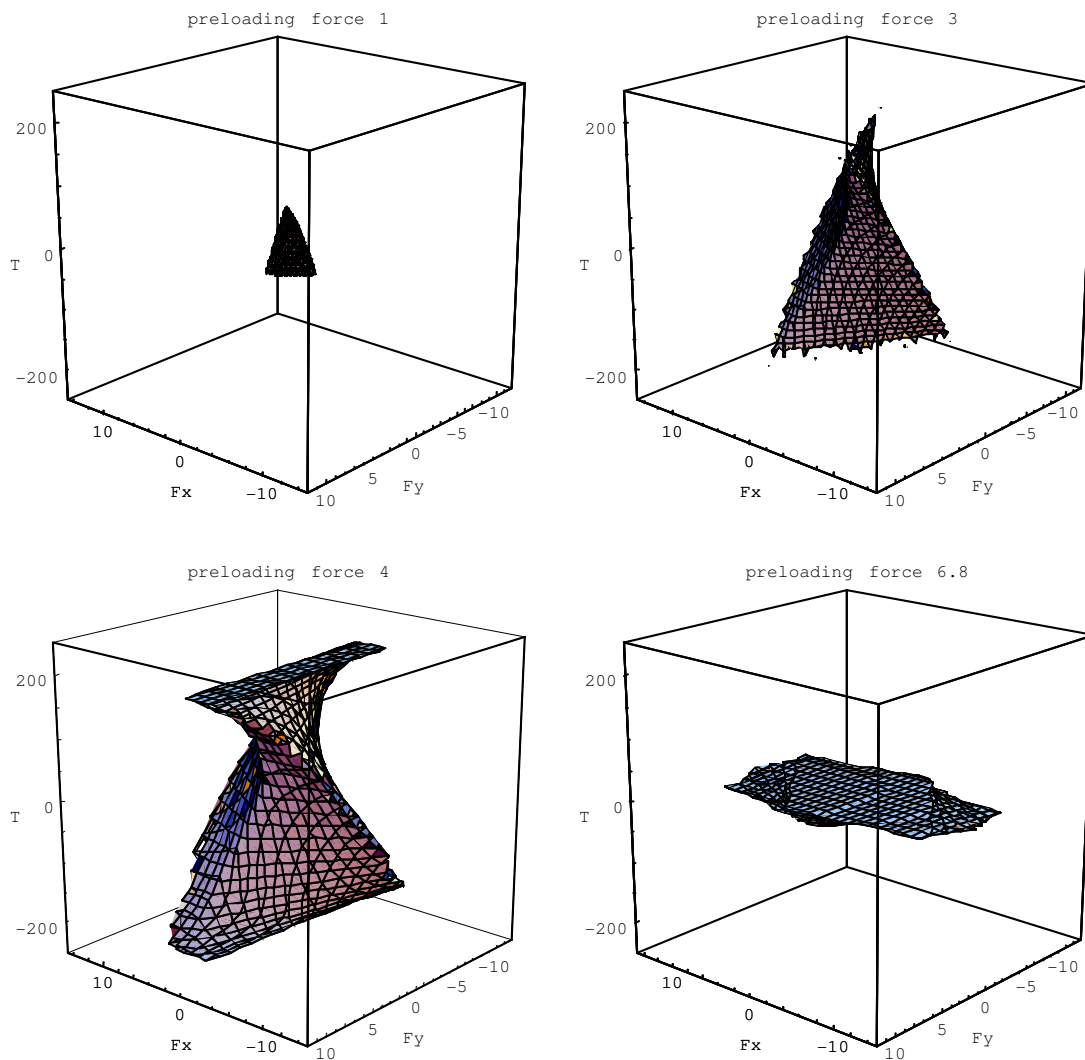


Figure 2.13: The force closure stability set presented in the wrench space for different preloading forces.

קבוצת סגור הכוחות היציבה מוצגת במרחב הכוחות והמומנטים עבור כוחות לחיצה התחלתיים שונים.

decreased as the preloading force increases. Increasing the external torque above a certain limit causes the matrix $D^2U(q)$ to become negative definite due to the term $\rho \cdot F$ in $D^2U(q)$ which becomes more negative as contact force increases. This phenomenon is often referred as "the coin snapping problem".

Figure 2.13 shows the manifold that bounds the force closure stability set for various preloading forces. The volume of the force closure stability set is small for low and high preloading forces, and larger for the middle range preloading forces. In addition, the shape of the force closure stability set is affected by the constraints bounding the set. As for low preloading forces friction is the only constraint bounding the force closure stability set, while for large preloading forces the bounding constraints are also due to the positive definiteness of $D^2U(q)$. For higher preloading forces the force closure stability set does not contain the origin resulting in instability for any given external wrench.

2.7 Conclusion

In active force closure the fingers resist external wrenches by actively applying the required forces at the contacts. Active grasping requires sophisticated contact-force sensors and contact-force controllers whose action must be precisely coordinated. In passive force closure each contact satisfies some fixed force-displacement law. The contacts apply preload grasping forces, and the balancing of external wrenches is performed automatically by the contacts. Passive grasping can be implemented with controllers that simply maintain fixed joint torques or fixed joint positions, without any coordination of the individual contacts.

We formally defined *force closure with compliant contacts* and provided necessary

and sufficient conditions for generic force closure grasps. In particular, the geometrical condition for active force closure is necessary but not sufficient for force closure with compliant contacts. To guarantee force closure, the grasped object must automatically converge to a nearby equilibrium where the contact forces balance the external wrench. Next we characterized the *force closure set* of compliant-rigid grasps. In these grasps a rigid object \mathcal{B} is held by compliant grasping mechanisms. We derived analytic expressions for the force closure set of such grasps. we used linear force-displacement laws for the following. A global stability criterion ensuring that the original unperturbed equilibrium would converge to the new equilibrium induced by the external wrench is presented. We characterize the force closure set for fingers having any shape at the contacts

Finally, we compare the force closure set of 2-finger and planar grasps with an experimental results that show a good matching between the computed set to the experiments results.

Chapter 3

PCG: A Foothold Selection

Algorithm

3.1 Introduction

This chapter presents a polynomial time algorithm, called PCG (short for Partitioned Cubes Gaiting), for planning the foothold positions of spider-like robots in planar tunnel environments.

A *spider-like robot* consists of k articulated limbs attached to a central body, such that each limb ends with a *footpad* (Figure 3.1). We assume that the robot moves quasistatically by exerting forces on the tunnel walls¹, while the robot is supported against gravity by frictionless contacts mounted under the mechanism. In general, a spider-like robot must have at least *three* limbs in order to move quasistatically in planar tunnel environments. At every instant the spider braces against the tunnel walls in static equilibrium using two or three limbs. During a 2-limb posture the

¹In quasistatic motion inertial effects due to moving parts of the robot are kept small relative to the forces and torques of interaction between the robot and the environment.

spider moves its free limb to the next foothold position. During a 3-limb posture the spider changes its internal geometry in preparation for the next limb lifting. The PCG algorithm is presented in the context of such 3-limb robots. However, we also discuss the generalization of the algorithm to robots having a higher number of limbs.

We make the following assumptions. First, we assume piecewise linear tunnel walls with known geometry. The tunnel can be discontinuous and can include holes or intersections. Second, each limb contacts the environment only through its footpad, which can only push against the environment. Third, each footpad contacts the tunnel walls through a frictional point contact, with a known lower bound on the coefficient of friction. The foothold positions are represented as points in contact c-space, which is defined as follows. Let L be the total length of the tunnel walls, and let $s_i \in [0, L]$ be the arc-length parametrization of the position of the i^{th} contact along the tunnel walls (Figure 3.2). Then for a k -limb mechanism *contact c-space* is the k -dimensional space $(s_1, \dots, s_k) \in [0, L]^k$. Fourth, we lump the kinematic structure of the robot into a single parameter called the *robot radius* and denoted R . This parameter is the length of a fully stretched limb, measured from the center of the robot's central base to the closet point on the limb's footpad. The algorithm uses this parameter to ensure that the selected foothold positions can be reached from the robot's central base.

The use of contact c-space is common in the grasp planning literature. For example, Elci Longman and Shoham [15] uses contact c-space of circle and ellipse in order to re-grasp the object and thus manipulate it. However, they do not optimize the number of re-grasp manipulation needed. Nguyen [52] and Ponce et al. [56, 57] introduced the notion of contact independent regions. Given a k -finger grasp of a

planar object, a contact independent region is a k -dimensional cube² in contact c-space. This cube represents k segments along the object's boundary, such that any placement of the k contacts inside these segments generates an equilibrium grasp. We use a similar notion in our representation of the feasible footholds as cubes in contact c-space. Each cube represents three segments along the tunnel walls, such that any placement of three footpads inside these segments results in a feasible 3-limb equilibrium posture. Other relevant papers from the grasp planning literature are papers that discuss finger gaiting. Brook Shoham and Dayan [8] presented a criterion for enabling sequence of re-grasp manipulations, but they do not globally optimize the number of re-grasp manipulation needed. Hong et al. [25] describe 3 and 4-finger gaits for planar objects. However, they assume that once an object is grasped, the fingers may not change their order along the object's boundary. In contrast, we impose no restriction on the order of the footpads along the tunnel walls. Goodwine et al. [18, 79] investigate the stratification of the full configuration space associated with finger gaiting. While this approach is justifiable for the design of feedback control laws, motion planning can be carried out in lower dimensional spaces such as contact c-space. For example, our 3-limb spider robot has 12 actuated joints and 3 unactuated degrees of freedom of the central base, while contact c-space has only three dimensions.

In the multi-legged locomotion literature, Boissonnat et al. [5, 6] discuss a motion planning algorithm for multi-legged robots that move in a gravitational field over a flat terrain. They assume that the legs are allowed to contact only a discrete collection of point sites. Much like our approach, they lump the kinematic structure of the robot into a reachability radius, and use this parameter to design a path that takes

²The cube is aligned with the coordinate axes and has three independent lengths.

the robot from start to target through a sequence of stable stances. Our work differs from the work of Boissonnat et al. in several fundamental ways. First, we consider motions where the robot stably braces against tunnel walls rather than maintaining stable stances against gravity. Second, we allow arbitrary footpad placement along the tunnel walls rather than on discrete point sites. Third, Boissonnat et al. first plan a path for the central body in the plane, then select footpad placements that realize the path. In contrast, the PCG algorithm first plans a sequence of foothold positions in contact c -space, then determines the mechanism's joint values that would bring the footpads to the desired foothold positions. Other papers that consider motion planning for multi-legged robots are [22, 37, 40, 41, 77]. However, all of these papers are concerned with locomotion over a terrain in a gravitational field, while we consider motion in congested tunnel-like environments.

This chapter focuses on the portion of the PCG algorithm that plans a sequence of foothold positions in contact c -space. The algorithm consists of the following three stages. The first stage is based on a key result, that the set of feasible 3-limb postures is a union of convex sets in contact c -space. Using convex optimization techniques, the algorithm approximates each of the convex sets by p maximal cubes. In the second stage the algorithm partitions the cubes into compatible sub-cubes, where two sub-cubes are *compatible* if it is possible to move between any two postures in these sub-cubes by a single limb lifting. However, compatibility encodes only a kinematic transition between two sub-cubes. Each sub-cube is also assigned an *orientation vector* which identifies what limbs can be stably lifted from the postures in the sub-cube. The algorithm constructs a graph whose nodes are sub-cubes and whose edges connect compatible sub-cubes with suitable orientation vectors. In the third stage the algorithm searches along the graph for the shortest sequence of foothold positions

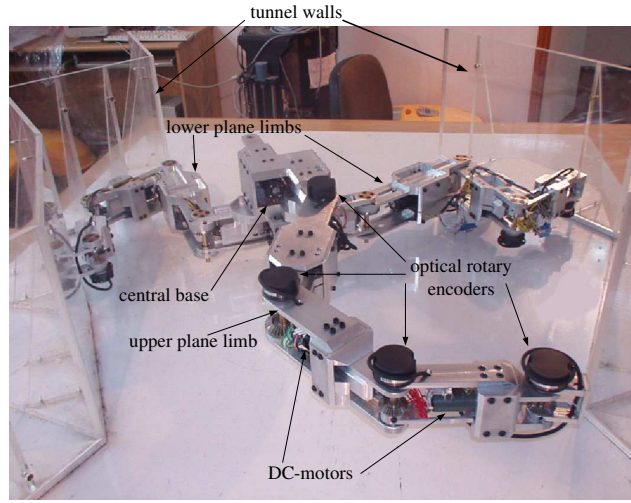


Figure 3.1: Top view of a 3-limb spider robot moving in a planar tunnel environment.

מבט על של רובוט עכביש תלת-רגלי הנע בתוך מנהרה מישורית.

that moves the robot from start to target. This sequence yields a minimal 3-2-3 gait pattern, where minimality is relative to the cube approximation of contact c -space.

The chapter is organized as follows. In Section 3.2 we characterize the feasible 3-limb postures in contact c -space. The feasible postures must be reachable, form stable equilibria, and satisfy a condition that allows their inclusion in a 3-2-3 gait pattern. In Section 3.3 we establish that the feasible 3-limb postures are a union of convex sets in contact c -space. It is also shown in this section that the approximation of a convex set by p maximal cubes is a convex optimization problem. In Section 3.4 we describe the PCG algorithm and analyze its computational complexity. In practical tunnel environments the robot can reach from any given position only a small number of walls. In such environments the algorithm runs in $O(np^6 \log(np))$ time, where n is the number of tunnel walls and p is the number of cubes used in the approximation of contact c -space. Next we investigate the effect of various p values on the path

length and present an algorithm that determine if p should be increased. In Section 3.6 we run the PCG algorithm on a simulated tunnel environment. An experimental results of the spider-robot walking in tunnel built in our laboratory is presented in section 5 and show practical implementation of the PCG algorithm. Finally, in the concluding section we discusses the generalization of the algorithm to robots with a higher number of limbs.

3.2 The Feasible 3-Limb Postures

In this section we characterize the feasible 3-limb postures as inequality constraints in contact c-space. The feasible 3-limb postures must form stable equilibria, be reachable, and satisfy the following *gait feasibility* condition. This condition requires that the 3-limb posture will contain two distinct 2-limb postures—one for entering the 3-limb posture by establishing a new foothold, and one for leaving the 3-limb posture by releasing some other foothold. Note that the initial and target 3-limb postures are required to contain one rather than two 2-limb postures. We now consider the individual constraints.

Equilibrium and stability of 2-limb postures. Gait feasibility requires that a 3-limb will contain two distinct 2-limb postures. Hence we first review the conditions for equilibrium and stability of 2-limb postures. By definition, a mechanism bracing against the environment is in *static equilibrium* if the net wrench (i.e. force and torque) generated by the contact forces acting on the mechanism is zero. In particular, a 2-limb mechanism forms an equilibrium posture if the line segment connecting the two contacts lies inside the two friction cones [52]. As a stability criterion we use the notion of force closure. By definition, an equilibrium posture is *force closure*

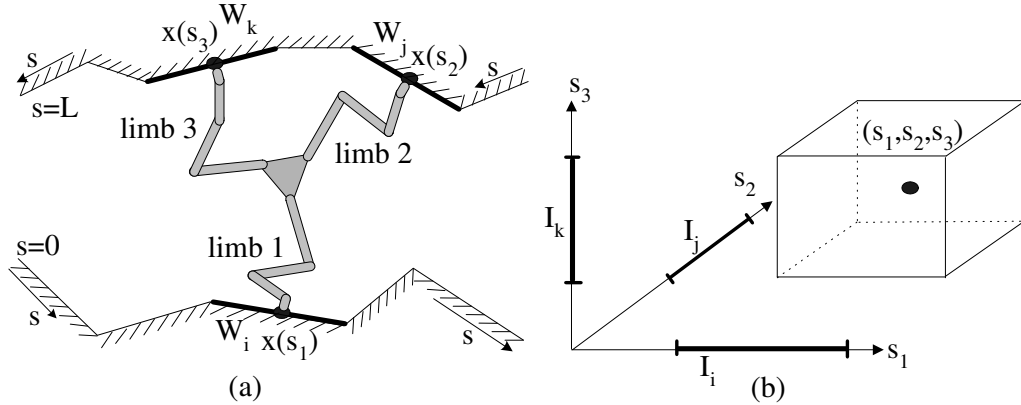


Figure 3.2: (a) A 3-limb robot in a planar tunnel, and (b) the parametrization of its contact c-space.

(a) רובוט תלת-רגלי במנהרה מישורית, ו-(b) פרמטריזציה של מרחב קונפיגורציות המגע שלו

if the mechanism can resist any perturbing wrench by suitable adjustment of its contact forces with the environment [4]. In general, an equilibrium posture in a planar environment is force closure if the contact forces of the unperturbed posture lie in the interior of the respective friction cones [80].

We now write the above conditions as inequalities in contact c-space. First we introduce some notation. The contact of each limb with the tunnel walls is parametrized by a scalar $s_l \in [0, L]$, where $l = 1, 2, 3$. Let W_1, \dots, W_n denote the tunnel walls, and let I_1, \dots, I_n be the partition of $[0, L]$ into intervals that parametrize the individual walls (Figure 3.2). Thus, for instance, the cube $I_i \times I_j \times I_k$ parametrizes the 3-limb postures where limb 1 contacts the wall W_i , limb 2 contacts the wall W_j , and limb 3 contacts the wall W_k . The unit tangent and unit normal to the wall W_i are denoted \mathbf{t}_i and \mathbf{n}_i , where \mathbf{n}_i is pointing away from the wall. Using this notation, the points along W_i are given by $\mathbf{x}(s) = \mathbf{x}_i + s\mathbf{t}_i$, where \mathbf{x}_i is the initial vertex of W_i and $s \in I_i$. Given a contact force f_i , we write the force as $f_i = f_i^t \mathbf{t}_i + f_i^n \mathbf{n}_i$, where f_i^t and f_i^n are

the tangent and normal components of f_i . The Coulomb friction cone at a contact along the i^{th} wall, denoted FC_i , is the collection of forces satisfying the inequalities: $FC_i = \{f_i : f_i^n \geq 0 \text{ and } -\mu f_i^n \leq f_i^t \leq \mu f_i^n\}$, where μ is the coefficient of friction.

Let two limbs with indices l and m contact the tunnel walls W_i and W_j . Then for a 2-limb stable equilibrium, the vector $x(s_m) - x(s_l)$ must lie in the interior of the friction cone FC_i , while $x(s_l) - x(s_m)$ must lie in the interior of the friction cone FC_j . This condition defines a set in the (s_l, s_m) plane, denoted \mathcal{E}_{ij}^{lm} , which is given by

$$\mathcal{E}_{ij}^{lm} = \{(s_l, s_m) \in I_i \times I_j : \begin{aligned} |(x(s_m) - x(s_l)) \cdot \mathbf{t}_i| &< \mu(x(s_m) - x(s_l)) \cdot \mathbf{n}_i, \\ |(x(s_l) - x(s_m)) \cdot \mathbf{t}_j| &< \mu(x(s_l) - x(s_m)) \cdot \mathbf{n}_j \end{aligned}\}.$$

An example of 2-limb stable equilibrium sets appears Figure 3.7. It is important to note that the inequalities describing \mathcal{E}_{ij}^{lm} are linear in s_l and s_m . Hence \mathcal{E}_{ij}^{lm} is a *convex polygon* in the (s_l, s_m) plane. When \mathcal{E}_{ij}^{lm} is considered as a subset of the contact c-space of a 3-limb mechanism, it becomes a three-dimensional set which is denoted as follows. Let \times serve as a place holder for the limb that does not participate in the 2-limb posture. Then a 2-limb equilibrium set, \mathcal{E}_{ij}^{12} for instance, becomes a three-dimensional set which is denoted $\mathcal{P}_{ij \times}$ and given by

$$\mathcal{P}_{ij \times} = \{(s_1, s_2, s_3) \in I_i \times I_j \times [0, L] : \begin{aligned} |(x(s_2) - x(s_1)) \cdot \mathbf{t}_i| &< \mu(x(s_2) - x(s_1)) \cdot \mathbf{n}_i, \\ |(x(s_1) - x(s_2)) \cdot \mathbf{t}_j| &< \mu(x(s_1) - x(s_2)) \cdot \mathbf{n}_j \end{aligned}\}.$$

The set $\mathcal{P}_{ij \times}$ is a prism orthogonal to the (s_1, s_2) plane with a polygonal cross section given by \mathcal{E}_{ij}^{12} . Similarly, the sets $\mathcal{P}_{i \times j}$ and $\mathcal{P}_{\times ij}$ are prisms orthogonal to the (s_1, s_3) and (s_2, s_3) planes, with polygonal cross sections given by \mathcal{E}_{ij}^{13} and \mathcal{E}_{ij}^{23} .

Reachability constraint of 3-limb postures. A 3-limb posture is reachable when its footholds lie within the robot's radius R . For each triplet of walls W_i, W_j, W_k , the

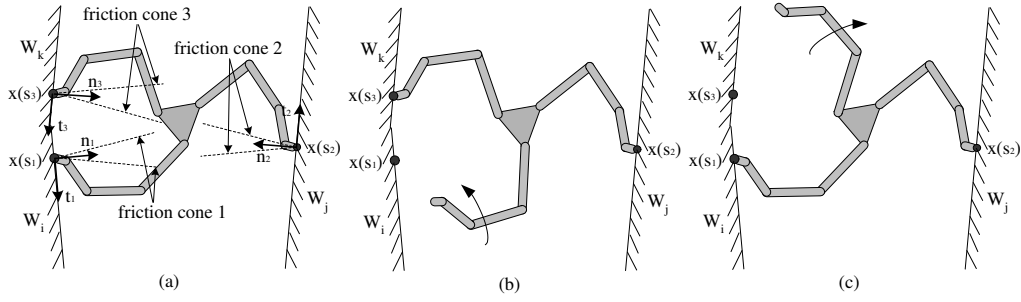


Figure 3.3: (a) A gait feasible 3-limb posture, (b)-(c) contains two distinct 2-limb postures.

(a) אחיזה תלת-רגלית חוקית, (b)-(c) המכילה שתי אחיזות דו-רגליות שונות.

reachability constraint is given by

$$\mathcal{R}_{ijk} = \{(s_1, s_2, s_3) \in I_i \times I_j \times I_k : \exists c \in \mathbb{R}^2 \max\{\|x(s_1) - c\|, \|x(s_2) - c\|, \|x(s_3) - c\|\} \leq R\}, \quad (3.1)$$

The point c appearing in (3.1) can be interpreted as the center of a disc containing the three foothold positions, such that the disc radius is bounded by R . As discussed below, the elimination of the existential quantifier in (3.1) results in a set which is bounded by quadratic surfaces in contact c-space.

Gait feasibility of 3-limb postures. A 3-limb posture is gait feasible if it contains two distinct 2-limb equilibrium postures (Figure 3.3). Let us write this constraint in the cell $I_i \times I_j \times I_k$ in contact c-space. The cell $I_i \times I_j \times I_k$ corresponds to contact with the walls W_i, W_j, W_k , and gait feasibility is satisfied by intersection of pairs of 2-limb prisms associated with the three walls. There are three such pairs— $(\mathcal{P}_{ij \times}, \mathcal{P}_{i \times k})$, $(\mathcal{P}_{ij \times}, \mathcal{P}_{\times jk})$, and $(\mathcal{P}_{\times jk}, \mathcal{P}_{i \times k})$ —and the resulting set of feasible 3-limb postures in the cell, denoted \mathcal{F}_{ijk} , is given by

$$\mathcal{F}_{ijk} = (\mathcal{P}_{ij \times} \cap \mathcal{P}_{i \times k} \cap \mathcal{R}_{ijk}) \cup (\mathcal{P}_{ij \times} \cap \mathcal{P}_{\times jk} \cap \mathcal{R}_{ijk}) \cup (\mathcal{P}_{\times jk} \cap \mathcal{P}_{i \times k} \cap \mathcal{R}_{ijk}). \quad (3.2)$$

Note that the same three walls appear in *six* cells in contact c-space, each corresponding to a specific assignment of the limbs to the three walls. The entire collection of feasible 3-limb postures is the union of all such sets over all ordered wall triplets. We end this section with an assertion that it is always possible to affect a transition between two 2-limb postures contained in a feasible 3-limb posture by suitable change of the contact forces.

Lemma 3.2.1 *Let a feasible 3-limb posture contain two 2-limb equilibrium postures. Then there exists a continuous change of the contact forces that allows a transition between the 2-limb postures, while the mechanism is kept in static equilibrium with fixed contacts.*

Proof: Since the mechanism has three limbs, any two 2-limb postures must share a limb in common. Without loss of generality, let the 3-limb posture lie inside $\mathcal{P}_{ij\times} \cap \mathcal{P}_{\times jk}$ in contact c-space, so that limb 2 is common to both 2-limb postures. Let \mathbf{f}_1 and \mathbf{f}_2 be the contact forces at the 2-limb posture involving limbs 1 and 2, and let \mathbf{g}_2 and \mathbf{g}_3 be the contact forces at the 2-limb posture involving limbs 2 and 3. Then it can be verified that the convex combination $(1-s)\mathbf{f}_1 + (1-s)\mathbf{f}_2 + s\mathbf{g}_2 + s\mathbf{g}_3$ where $s \in [0, 1]$ generates a zero net wrench for all s . This convex combination specifies a continuous transition between the two 2-limb postures, while the mechanism is kept in static equilibrium. Specifically, the contact forces of limbs 1 and 3 vary only in magnitude, while the contact force of limb 2 varies in magnitude and direction between \mathbf{f}_2 and \mathbf{g}_2 . Finally, since \mathbf{f}_2 and \mathbf{g}_2 lie inside the friction cone at the contact of limb 2 with the environment, their convex combination also lies inside the friction cone, for all $s \in [0, 1]$. □

The lemma generalizes as follows. If a k -limb posture contains two equilibrium postures having a smaller number of limbs, it is always possible to affect a transition between these two posture by suitable change of the contact forces, while the mechanism is kept in static equilibrium.

3.3 Convexity of the Feasible 3-Limb Postures

In this section we discuss two issues concerning convexity that will be used by the PCG algorithm. First we establish that the feasible 3-limb postures are a union of convex sets in contact c-space. Then we show that the approximation of a convex set by p maximal cubes is a convex optimization problem.

3.3.1 Convexity of the Feasible Postures

The set \mathcal{F}_{ijk} of feasible 3-limb postures is specified in (3.2) as a union of three sets, each corresponding to a different pair of 2-limb postures. The following lemma asserts that each of these sets is convex in contact c-space.

Lemma 3.3.1 *In each cell $I_i \times I_j \times I_k$ of contact c-space, the set \mathcal{F}_{ijk} of feasible 3-limb postures is a union of three convex sets.*

Note that any of the convex sets comprising \mathcal{F}_{ijk} may be empty. For example, in Figure 3.8 each set \mathcal{F}_{ijk} is either empty or consists of a single convex set.

Proof: The three sets that comprise \mathcal{F}_{ijk} have a similar form. Hence it suffices to consider only one of these sets, say $\mathcal{P}_{ij \times} \cap \mathcal{P}_{\times jk} \cap \mathcal{R}_{ijk}$. The prisms $\mathcal{P}_{ij \times}$ and $\mathcal{P}_{\times jk}$ are defined by intersection of linear inequalities. Each prism is therefore a convex polytope in contact c-space. Next consider the reachability set \mathcal{R}_{ijk} . The existential

quantifier in (3.1) acts on a set, denoted $\bar{\mathcal{R}}_{ijk}$, which is defined in the five-dimensional space (s_1, s_2, s_3, c) :

$$\bar{\mathcal{R}}_{ijk} = \{(s_1, s_2, s_3, c) \in I_i \times I_j \times I_k \times \mathbb{R}^2 : \max\{\|x(s_1) - c\|, \|x(s_2) - c\|, \|x(s_3) - c\|\} \leq R\}.$$

The norm function $\|x - c\|$ is convex in (x, c) space, and each $x(s_i)$ is linear in s_i . Since composition of a convex function with a linear map preserves convexity, the functions $\|x(s_i) - c\|$ are convex in (s_1, s_2, s_3, c) space. In general, the pointwise maximum of convex functions is a convex function [12, p. 47]. Hence $\bar{\mathcal{R}}_{ijk}$ is convex in (s_1, s_2, s_3, c) space. But \mathcal{R}_{ijk} is the coordinate projection of $\bar{\mathcal{R}}_{ijk}$ onto contact c-space. Since projection preserves convexity, \mathcal{R}_{ijk} is convex in contact c-space. Finally, the intersection of convex sets is convex, hence $\mathcal{P}_{ij} \cap \mathcal{P}_{jk} \cap \mathcal{R}_{ijk}$ is convex. \square

The PCG algorithm described below approximates the feasible 3-limb postures by cubes. The approximation requires an explicit formula for the reachable set which we now describe. The following is an equivalent formulation for \mathcal{R}_{ijk} ,

$$\mathcal{R}_{ijk} = \{(s_1, s_2, s_3) \in I_i \times I_j \times I_k : r_{min}(s_1, s_2, s_3) \leq R\},$$

where $r_{min}(s_1, s_2, s_3)$ is the radius of the minimal disc containing the foothold positions $x(s_1)$, $x(s_2)$, and $x(s_3)$. Let Δ be the triangle generated by these three points. Then the formula for $r_{min}(s_1, s_2, s_3)$ is divided into two cases (Figure 3.4). When Δ is an acute triangle (i.e. with angles less than 90°), $r_{min}(s_1, s_2, s_3)$ is the radius of the disc passing through the three points, given by

$$r_{min}(s_1, s_2, s_3) = \frac{\|x(s_1) - x(s_2)\| \cdot \|x(s_2) - x(s_3)\| \cdot \|x(s_3) - x(s_1)\|}{2\|x(s_1) \times x(s_2) + x(s_2) \times x(s_3) + x(s_3) \times x(s_1)\|},$$

where $u \times v$ is the scalar obtained by taking the determinant of the 2×2 matrix $[u \ v]$. When Δ is an obtuse triangle, $r_{min}(s_1, s_2, s_3)$ is simply half the length of the longest

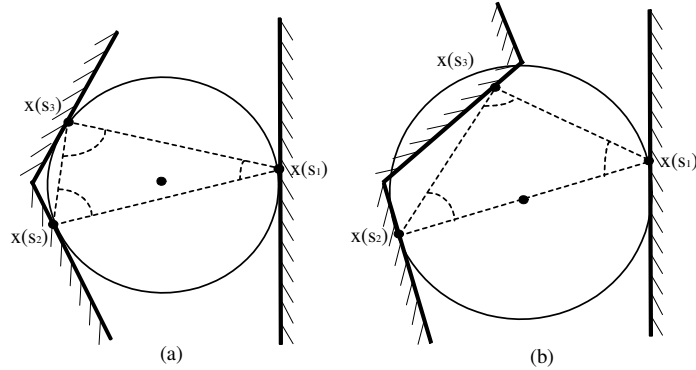


Figure 3.4: The minimal disc containing the three foothold positions when Δ is (a) an acute triangle, and (b) an obtuse triangle.
הדיסק המינימלי המכיל את שלושת נקודות האחיזה כאשר Δ הוא (a) משולש חד-זווית, ו-(b) משולש כהה-זווית.

edge of Δ ,

$$r_{min}(s_1, s_2, s_3) = \frac{1}{2} \max_{1 \leq p, q \leq 3} \{\|x(s_p) - x(s_q)\|\}.$$

The two-part formula for $r_{min}(s_1, s_2, s_3)$ reveals that the set \mathcal{R}_{ijk} is bounded by quadratic surfaces in contact c-space. To summarize, the set \mathcal{F}_{ijk} is the union of three *convex* sets, each bounded by planar surfaces associated with the 2-limb prisms, and quadratic surfaces associated with the reachability constraint.

3.3.2 Convexity of the Cube Approximation Problem

We have already established in Lemma 3.3.1 that the set \mathcal{F}_{ijk} is a union of three convex sets. Now we discuss the approximation of these convex sets by maximal cubes. We discuss the problem in the context of three dimensional contact c-spaces, but the result is completely general.

Consider the approximation of a three-dimensional convex set \mathcal{S} by p cubes, where the cubes have arbitrary center and dimensions. We assume as input a desired relative

configuration for the cubes, where a *relative configuration* is a specification of an adjacency relation between the cubes in terms of a set of separating planes, such that no two cubes can possibly intersect. Each of the separating planes is defined in terms of the relative position of two cubes, and does not restrict the absolute position of the two cubes. The i^{th} cube is parameterized by its center $c_i \in \mathbb{R}^3$, and its dimensions along the coordinate axes, $h_i \in \mathbb{R}^3$. The optimization therefore takes place in the $6p$ -dimensional space whose coordinates are $(c_1, h_1, \dots, c_p, h_p)$. Our objective is to maximize the total volume of the cubes. However, the sum of the cubes' volumes is not a convex function of the optimization variables. Rather, we use a normalized total volume function given by³

$$\phi(c_1, h_1, \dots, c_p, h_p) = \sum_{i=1}^p (h_{i1}h_{i2}h_{i3})^{\frac{1}{3}}.$$

Next we list the constraints involved in the cube approximation problem. First we have the requirements that the cubes' dimensions be non-negative, and that their centers would lie inside contact c-space. Second, the relative configuration of the cubes is specified by a list of separating planes, each involving the center and dimensions of two cubes separated by the plane. Last, we must ensure that the cubes lie inside the convex set \mathcal{S} . The following proposition asserts that the maximization of ϕ over p cubes contained in \mathcal{S} is a convex optimization problem.

Proposition 3.3.2 *The maximization of $\phi = \sum_{i=1}^p (h_{i1}h_{i2}h_{i3})^{\frac{1}{3}}$ over p cubes contained in a convex set \mathcal{S} and satisfying a relative-configuration specification is a convex optimization problem.*

Proof: In general, the minimization of a scalar function $\phi(x)$ subject to scalar constraints $\psi_1(x), \dots, \psi_r(x) \leq 0$ is *convex* if ϕ and ψ_1, \dots, ψ_r are convex functions

³We are grateful to Prof. A. Nemirovsky who suggested this function.

of the optimization variables. In our case, the maximization of the total volume function ϕ is equivalent to the minimization of $-\phi$, and convexity of $-\phi$ is equivalent to *concavity* of ϕ . Hence we must first verify that the function $\phi = \sum_{i=1}^p (h_{i1}h_{i2}h_{i3})^{\frac{1}{3}}$ is concave. A sufficient condition is that the second derivative matrix of ϕ be negative semi-definite. Since ϕ depends only on the variables h_1, \dots, h_p , its second derivative matrix is block diagonal, with non-zero 3×3 blocks corresponding to the second derivative of the functions $\phi_i = (h_{i1}h_{i2}h_{i3})^{1/3}$ where $i = 1, \dots, p$. The first derivative of ϕ_i , written as a column vector, is:

$$D\phi_i = \frac{1}{(h_{i1}h_{i2}h_{i3})^{\frac{2}{3}}} \begin{pmatrix} h_{i2}h_{i3} \\ h_{i1}h_{i3} \\ h_{i1}h_{i2} \end{pmatrix}.$$

The second derivative of ϕ_i is:

$$\begin{aligned} D^2\phi_i &= \frac{1}{(h_{i1}h_{i2}h_{i3})^{\frac{2}{3}}} \begin{bmatrix} 0 & h_{i3} & h_{i2} \\ h_{i3} & 0 & h_{i1} \\ h_{i2} & h_{i1} & 0 \end{bmatrix} - \frac{1}{(h_{i1}h_{i2}h_{i3})^{\frac{5}{3}}} \begin{pmatrix} h_{i2}h_{i3} \\ h_{i1}h_{i3} \\ h_{i1}h_{i2} \end{pmatrix} \begin{pmatrix} h_{i2}h_{i3} & h_{i1}h_{i3} & h_{i1}h_{i2} \end{pmatrix} \\ &= -\frac{1}{(h_{i1}h_{i2}h_{i3})^{\frac{2}{3}}} \begin{bmatrix} \frac{h_{i2}h_{i3}}{h_{i1}} & 0 & 0 \\ 0 & \frac{h_{i1}h_{i3}}{h_{i2}} & 0 \\ 0 & 0 & \frac{h_{i1}h_{i2}}{h_{i3}} \end{bmatrix}. \end{aligned}$$

The resulting matrix $D^2\phi_i$ has only negative eigenvalues and is therefore negative definite. The entire matrix $D^2\phi$ is consequently negative semi-definite, and ϕ is a concave function.

Next consider the constraints on the optimization variables. First, the constraint that the cubes' dimensions be non-negative is linear in the optimization variables, and linear functions are convex. Second, a relative configuration of the cubes is specified

by a list of constraints of the form: $c_{i1} + \frac{1}{2}h_{i1} \leq c_{j1} - \frac{1}{2}h_{j1}$. (This particular constraint separates the i^{th} and j^{th} cubes along a plane orthogonal to the s_1 -axis.) We see that the separation constraints are also linear in the optimization variables. Last consider the constraint that the cubes must lie inside the convex set \mathcal{S} . The i^{th} cube lies inside \mathcal{S} if its vertices lie in \mathcal{S} . We may assume that \mathcal{S} is specified by inequalities $\psi_1(s_1, s_2, s_3), \dots, \psi_r(s_1, s_2, s_3) \leq 0$ such that ψ_1, \dots, ψ_r are convex functions. In that case a vertex v_j lies in \mathcal{S} if it satisfies the inequalities $\psi_1(v_j), \dots, \psi_r(v_j) \leq 0$. Each vertex is given by an expression of the form $v_j = c_i \pm \frac{1}{2}h_i$ for a suitable selection of the signs of $h_i \in \mathbb{R}^3$. The vertices are therefore linear functions of the optimization variables. Since composition of a convex function with a linear map preserves convexity, the cube containment constraints are convex functions of the optimization variables. \square

It is worth mentioning that convex optimization algorithms, for instance the ellipsoid algorithm used in our implementation, generate an ϵ -accurate solution in $O(m^2 l \log(1/\epsilon))$ time, where m is the number of optimization variables and l the number of steps required to evaluate the constraints. An example of the approximation of a convex set by five maximal cubes appears in Figure 3.9.

3.4 The PCG Algorithm

In this section we describe the PCG algorithm and analyze its computational complexity. First we give an overview of the algorithm. The set of feasible 3-limb postures in each cell of contact c-space is a union of three convex sets. However, in practical tunnel environments each cell contains at most one convex set. We describe the algorithm under the assumption of a single convex set per cell, and discuss the case of

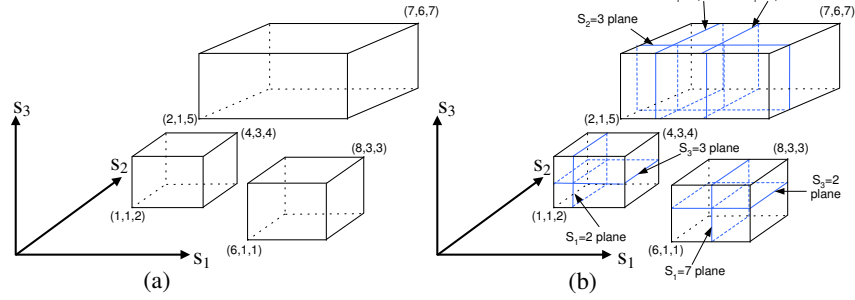


Figure 3.5: (a) Three cubes in contact c -space, and (b) their mutual partition into sub-cubes along the separating planes.

(a) שלוש תיבות במרחב קונפיגורציות המגע, ו-(b) וחלוקה החדית שלהן ע"י המישורים המפרידים.

multiple convex sets in the appendix. The algorithm first approximates each of the convex sets by p maximal cubes. The number of cubes and their relative configuration are user-specified inputs whose practical selection is discussed below. In order to describe the next stage of the algorithm we introduce the notion of cube orientation. A maximal cube parametrizes a set of feasible 3-limb postures, each containing two distinct 2-limb postures. The two 2-limb postures necessarily share a limb in common. However, this common limb *cannot be lifted*, since its lifting would destroy both 2-limb postures. By construction, all the 3-limb postures parametrized by a given maximal cube have the same common limb. In contact c -space, we associate with each maximal cube an *orientation vector*, which is aligned with the s_i -axis of the limb that cannot be lifted from the 3-limb postures parametrized by the cube. The orientation vectors play an important role in the graph construction described below.

In the second stage the algorithm partitions the maximal cubes as follows. The algorithm constructs an arrangement of all the separating planes of the cubes, where each separating plane contains one of the cubes' faces. Using this arrangement, the

algorithm partitions the cubes as illustrated in Figure 3.5. The figure shows three cubes and their mutual partition along the separating planes into sub-cubes. During the partition process each sub-cube inherits the orientation vector of its parent cube. The resulting sub-cubes are disjoint⁴, and they satisfy the following projection property. Any two sub-cubes either have the same projection on one of the coordinate planes, or their projection on all three coordinate planes are disjoint. If two sub-cubes share a projection they are called *compatible*, and the s_i -axis aligned with the direction of projection is called the *direction of compatibility*. The algorithm next defines a graph called the *sub-cube graph*. The nodes of the graph are center points of the sub-cubes. The edges of the graph connect compatible sub-cubes whose direction of compatibility is orthogonal to the orientation vector of the two sub-cubes.

Let us pause to discuss the edges of the sub-cube graph. Every edge of the graph represents lifting and re-placement of a particular limb. The lifting of a limb must leave the robot with a stable 2-limb posture. The orientation vector of a sub-cube describes which limb may not be lifted from the 3-limb postures parametrized by the sub-cube. Hence all edges emanating from a node must be *orthogonal* to the orientation vector of the sub-cube associated with the node. Moreover, all edges of the sub-cube graph are *straight lines parallel to the s_i -axes in contact c -space* (Figure 3.11). For example, when an edge is parallel to the s_1 -axis, motion along this edge means that only limb 1 is moving, while the foothold positions of limbs 2 and 3 remain fixed. According to Lemma B.0.1 in the appendix, the motion of a limb between any two sub-cubes connected by an edge can be executed such that reachability is maintained throughout the limb's motion. Finally, the start and target 3-limb postures, denoted S and T , are added as special nodes to the sub-cube graph.

⁴We say that two sets are *disjoint* when their interiors are disjoint.

The construction of edges from S and T to the other nodes of the graph is described below.

In the third stage the algorithm assigns unit weights to all edges, then searches along the sub-cube graph for the shortest path from S to T . The shortest path on the graph minimizes the number of limb lifting and re-placement steps along the path from start to target. However, this minimality is only relative to the cube approximation obtained in the first stage of the algorithm. A formal description of the algorithm follows.

PCG Algorithm:

Input: Geometrical description of an n -wall tunnel. A value for the coefficient of friction. Start and target 3-limb postures S and T . A value for the number of cubes p and their relative configuration.

1. Cube approximation:

- 1.1 Determine which cells $I_i \times I_j \times I_k$ contain a non-empty set \mathcal{F}_{ijk} of feasible 3-limb postures.
- 1.2 Approximate each non-empty set \mathcal{F}_{ijk} by p maximal cubes. Assign an orientation vector to each maximal cube.

2. Cube partition:

- 2.1 Construct an arrangement of the separating planes of all maximal cubes.
- 2.2 Subdivide each maximal cube into sub-cubes along the separating planes. Assign to each sub-cube the orientation vector of its parent maximal cube.
- 2.3 Define a *sub-cube graph* with nodes at the center of the sub-cubes, and edges between compatible sub-cubes whose direction of compatibility is orthogonal to the orientation vector of both sub-cubes.

2.4 Define S and T as special nodes and connect them to the graph as described below.

3. Graph search:

3.1 Assign unit weight to all edges.

3.1 Search for the shortest path along the sub-cube graph from S to T .

Two technical details of the algorithm need explanation. The first is the construction of edges from S and T to the other nodes of the graph. For simplicity, let the start and target be feasible 3-limb postures with their own orientation vector. (In general, S and T are required to contain only one stable 2-limb posture.) For the start and target nodes, compatibility with a sub-cube means that the projection of the sub-cube on one of the coordinate planes contains the corresponding projection of the node. Having defined orientation and compatibility for S and T , the edges connecting these nodes to the other nodes of the graph are constructed by the rule specified in step 2.3 of the algorithm. The second technical issue is the selection of a relative configuration for the p cubes. In principal any relative configuration can be used by the algorithm. In the next section we specify in each cell a relative configuration that separates the p cubes perpendicular to the cell's direction vector. This relative configuration tends to preserve the connectivity of the set feasible 3-limb postures in the cell.

Next we discuss some notable features of the algorithm. First, the uniform weight assignment reflects our desire to minimize the total number of limb lifting and replacement along the path. However, the edges can be assigned different weights, for instance, ones that reflect a measure of distance traversed between successive footholds. Second, the path generated by the algorithm is contact independent in two ways. Each node of the graph parametrizes three contact independent wall segments, and each edge of the graph can be realized by limb lifting and re-placement between

any two postures in the sub-cubes joined by the edge. Third, the algorithm treats the motion of a limb between walls and along a single wall in a uniform manner. One implication of this uniformity is that small changes to the tunnel geometry, for instance a change of a long straight wall into a piecewise linear wall, would not have a significant influence on the path generated by the algorithm. Last, the size of the sub-cube graph increases with p . However, if an edge exists in the graph for low values of p , it would persist in the graph for larger values of p . Consequently, the path from start to target only becomes shorter as p increases.

The remainder of this section is concerned with the computational complexity of the algorithm. We assume in the analysis that the robot can reach from any given position only a small number of walls which is bounded by a constant. This assumption is called *local reachability*.

Theorem 5 *Let S and T be start and target 3-limb postures in a tunnel environment that satisfies the local reachability assumption. Then the PCG algorithm finds the shortest path from S to T in the cube approximation of contact c -space in $O(np^6 \log(np))$ time using $O(np^6)$ space, where n is the number of tunnel walls and p is the number of maximal cubes in each non-empty cell of contact c -space.*

Proof: First consider step 1.1 of the algorithm, identifying which cells of contact c -space contain feasible 3-limb postures. The feasible 3-limb postures must in particular be reachable, and the algorithm first identifies which cells contain reachable 3-limb postures. The radius- R neighborhood about a wall is bounded by two linear and two quadratic curves. The collection of these neighborhood forms a planar arrangement of $O(n)$ curves. By the local reachability assumption, a radius- R neighborhood intersects a constant number of other radius- R neighborhoods. Hence

the arrangement of radius- R neighborhoods contains $O(n)$ intersection points. A line sweep algorithm can compute the intersection points in $O(n \log(n))$ time. Each intersection point is associated with a finite number of overlapping radius- R neighborhoods, and any triplet of overlapping neighborhoods is a potentially non-empty cell in contact c-space. Thus we obtain $O(n)$ potentially non-empty cells in $O(n \log(n))$ time. The actual verification that these cells are non-empty is carried out in the next step of the algorithm.

Next consider step 1.2, where each non-empty set \mathcal{F}_{ijk} is approximated by p maximal cubes. Any convex optimization algorithm first computes an initial feasible solution, or reports that no feasible solution exists. This first step determines which of the $O(n)$ cells generated by the line sweep algorithm contains a non-empty set of feasible 3-limb postures. Standard convex optimization algorithms, for instance the ellipsoid algorithm used in our implementation, generate an ϵ -accurate solution in $O(m^2 l \log(1/\epsilon))$ time, where m is the number of optimization variables and l the number of steps required to evaluate the constraints [50]. In our case $m = 6p$ since each cube has six parameters. The l constraints are the validity of the cubes' relative configuration, and the containment of the cubes' vertices in \mathcal{F}_{ijk} . The relative configuration consists of $p - 1$ separating planes, and the total number of cube vertices is $8p$. Thus $m = O(p)$ and $l = O(p)$. The approximation of each set \mathcal{F}_{ijk} by p maximal cubes takes $O(p^3 \log(1/\epsilon))$ time. Since there are $O(n)$ potentially non-empty sets \mathcal{F}_{ijk} , step 1.2 generates $O(np)$ maximal cubes in $O(np^3 \log(1/\epsilon))$ time.

Next consider steps 2.1 and 2.2, where the maximal cubes are partitioned into sub-cubes. Since there are $O(np)$ maximal cubes, sorting the cubes' separating planes and generating their arrangement takes $O(np \log(np))$ time. Each of the maximal cubes parameterizes three segments along the tunnel walls. When two limbs contact two of

the three segments, the local reachability assumption implies that the third limb can reach a constant number of walls. Since only one limb has moved, the 3-limb posture resulting from the re-placement of the third limb must reach a maximal cube whose projection overlaps the projection of the previous maximal cube. Since the limb can reach a constant number of cells each containing p maximal cubes, *every maximal cube has an overlapping projection with $O(p)$ other maximal cubes*. Consider now the partitioning of a maximal cube along the separating planes. If we first partition the maximal cube along the s_1 -axis, it is divided into $O(p)$ slabs orthogonal to the s_1 -axis. The slabs are divided along the s_2 -axis into $O(p^2)$ rectangular prisms. Finally, the prisms are divided along the s_3 -axis into $O(p^3)$ sub-cubes. Since there are $O(np)$ maximal cubes, step 2.2 generates a total of $O(np^4)$ sub-cubes in $O(np^4)$ time.

Step 2.3 concerns the construction of edges between sub-cubes. In our implementation the edges are constructed during the cube partitioning process. For purposes of analysis, let us assume that the construction of an edge takes $O(1)$ time, so that the time for step 2.3 is equal to the total number of edges in the sub-cube graph. Recall that all edges are aligned with the s_i -axes, and that an edge connects compatible sub-cubes with a matching projection on one of the coordinate planes. A maximal cube has an overlapping projection with $O(p)$ other maximal cubes. In each of these overlaps two columns of the maximal cubes have a matching projection. Since each column contains $O(p)$ sub-cubes, each sub-cube can have a common projection with $O(p^2)$ other sub-cubes. The edge degree of a sub-cube is therefore $O(p^2)$. Since there are $O(np^4)$ sub-cubes, the total number of edges is $O(np^6)$. Note that the size of the sub-cube graph, $O(np^6)$, is the space requirement of the algorithm.

Finally consider step 3. In general, a shortest path search on a graph with m vertices and e edges takes $O(e \log(m))$ time. Substituting $m = O(np^4)$ and $e =$

$O(np^6)$, the search for the shortest path along the sub-cube graph takes $O(np^6 \log(np))$ time. Summarizing all the steps, we obtain a run time of $O(n \log(n) + np^3 \log(1/\epsilon) + np^4 + np^6 \log(np)) = O(np^6 \log(np))$. \square

3.5 Selection Number of Maximal Cubes

In this section we oracle p , number of maximal cubes, to sufficiently approximate the convex set of foothold positions. low values of p may result with connectivity lose between convex sets or between maximal cubes within a convex set. To check connectivity between two convex sets we need to check if there *exist* two compatible 3-limb postures in every pair of convex sets. Thus, in the first subsection we check if there exist a common projection on the main planes for two convex sets. In the second subsection we discuss how to select the relative configuration of maximal cubes in order to reduce lose of connection between the p maximal cubes approximating a convex set. The choice of the relative configuration of the maximal cubes has implication on the ability to conduct steps between the maximal cubes within a convex set. This section concludes with an algorithm that check whether p maximal cubes sufficiently approximate a convex set.

3.5.1 Connectivity Between Convex Sets

A connection between two convex sets of feasible 3-limb postures exists if there exist a common projection on the main planes in direction perpendicular to the two direction vectors. The following theorem states that the problem of checking the connectivity between two convex sets is a convex programming problem.

Theorem 6 *Let $c = (c_1, \dots, c_k) \in C \subset \mathbb{R}^k$ and $d = (d_1, \dots, d_k) \in D \subset \mathbb{R}^k$ be convex sets. Then the existence problem of points c and d such that $c_i = d_i$ for $i \in I = \{m_1, \dots, m_l\}$ is a convex programming problem.*

Proof: We construct \mathbb{R}^{2k} space, where C and D are in two orthogonal subspaces of \mathbb{R}^{2k} . Next we construct cylinders over C and D denoted $C_c \subset \mathbb{R}^{2k}$ $D_c \subset \mathbb{R}^{2k}$ respectively. Consider the set $C_c \cap D_c$. This set is convex since it is intersection of convex sets. Every point in $C_c \cap D_c$ is of the form $(c_1, \dots, c_k, d_1, \dots, d_k)$ and represents two points in \mathbb{R}^k that are in C and D respectively. Denote the subspace $P = \{(s_1, \dots, s_{2k}) : s_i = s_{i+k} \forall i \in I\}$. Every point in Linear subspace P represent two points in \mathbb{R}^k that share the same value along the i^{th} coordinate. The set $P \cap C_c \cap D_c$ is convex since it is intersection of a hyperplane with convex set. Moreover every point in $P \cap C_c \cap D_c$ represent a point in C and point in D such that these points share the same value along the i^{th} coordinate. The problem now reduced to find if a convex set is not empty, that can be done using the deep-cut ellipsoid algorithm [7] \square

3.5.2 Selection of the Maximal Cubes Relative Configuration

We wish to select the relative configuration of the maximal cubes in such way that it will be possible to carry out at least one step within every convex set. To enable at least one step within a convex set two consecutive maximal cubes must have a common projection on one of the major planes, and the projection direction must be perpendicular to the direction vector of the convex set.

We chose the maximal cubes relative configuration to be linear. In this configuration there is only one plane separating between each cube to the consecutive one.

This is the simplest configuration yet it well approximates the convex set, since every cube takes volume of a thick cube shaped layer from the convex set.

We assigned a direction vector to every convex set. It is possible to perform steps only in directions perpendicular to the direction vector. Therefore a motion between the maximal cubes can be carried out only if the configuration of the maximal cube is perpendicular to the direction vector of the convex set. To conclude we choose linear relative configuration of maximal cubes in direction perpendicular to the convex set direction vector. Note however that we still have two directions that we can randomly select one of them for the configuration of the maximal cubes.

3.5.3 An Algorithm to Oracle Number of Maximal Cubes

Next, we describe an algorithm which is simply a function that generate an error message if the value of p is too small. The criterion to decide whether p is large enough is based on preserving connectivity within convex set and between convex sets. We do not want the approximation of the convex sets to brake any possible connections. Note however that this lower bound is not necessarily tight.

Checking number of maximal cubes algorithm

Input: The maximal cubes approximating the convex sets.

For each convex set \mathcal{F}_{ijk} whose orientation vector is along s_l do:

1. Check if every consecutive maximal cubes in \mathcal{F}_{ijk} have common projection along axis perpendicular to s_l . if not send message “ p is too small”.
2. Find all \mathcal{F}_{mno} such that
 - Case $l = 1$: $m = i$ and ($n = j$ or $o = k$)
 - Case $l = 2$: $n = j$ and ($m = i$ or $o = k$)

Case $l = 3$: $o = k$ and $(m = i$ or $n = j)$

3. For every \mathcal{F}_{mno} from step 2 do:

3.1 Check if there exist 3-limb postures in \mathcal{F}_{ijk} that is compatible to a 3-limb postures in \mathcal{F}_{mno} using convex programming technique. If there is not such compatible pair continue to the next \mathcal{F}_{mno} in step 3.

3.2 Check compatability of all possible pairs of maximal cubes such that one cube is in \mathcal{F}_{ijk} and the second is in \mathcal{F}_{mno} . If there is not a compatible pair send message “ p is too small”.

The effect of p value selection can be explained using Figure 3.6. In this 2D figure when p is too small the connection between the maximal cubes is lost and path is not available even though connection between the convex sets exists. When p is large enough there exist connection between the maximal cubes and path is available. In the figure it can be seen that there is no point of enlarging p beyond some limit since it will not affect the length of the path (number of steps along the path) or the effect will be minor.

3.6 Simulation Results

In this section we run several simulations. First we present full implementation of the PCG algorithm for selection of foothold positions along simulated tunnel. Next we investigate the effect of various p , number of maximal cubes, values on the path length.

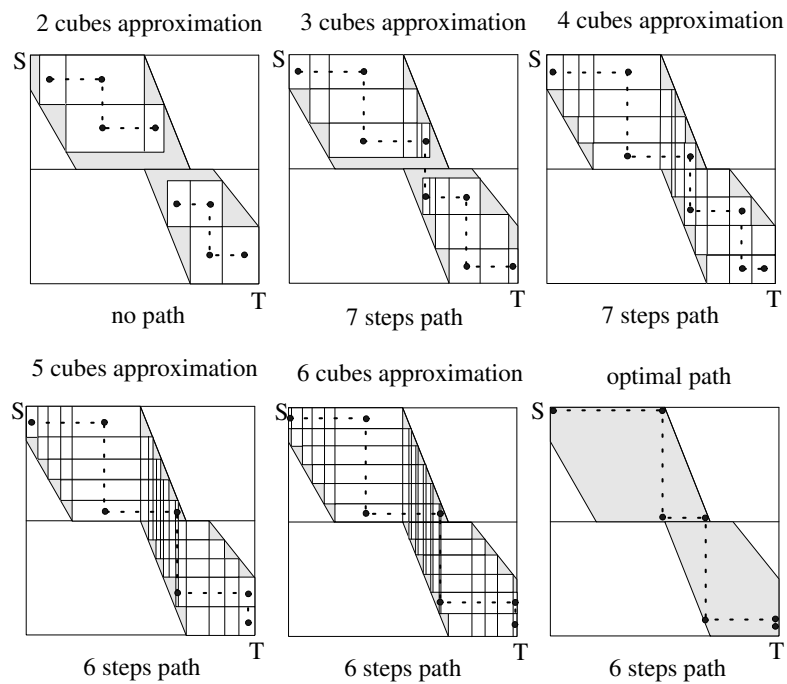


Figure 3.6: 2D illustration of the effect of number of approximating cubes on the number of steps in the path
 אילוסטרציה דו-מימדית המראה את ההשפעה של מספר התיבות המקסימליות על אורך המסלול.

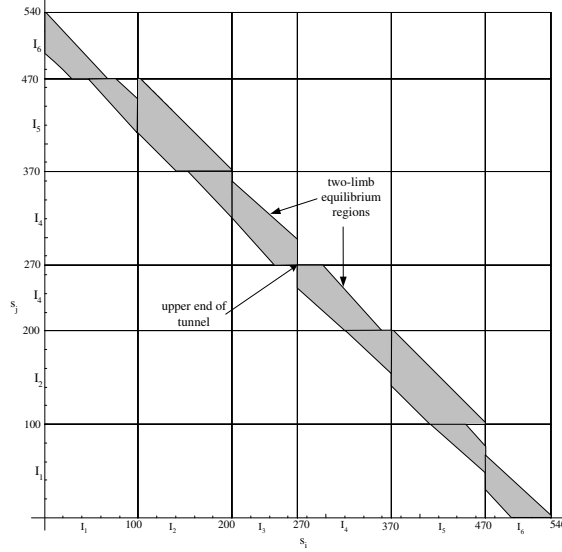


Figure 3.7: The 2-limb equilibrium postures in the (s_i, s_j) plane.
 תנוחות שיווי-משקל דו-רגליות במישור (s_i, s_j) .

3.6.1 Simulation of the PCG Algorithm

We run the PCG algorithm in the tunnel depicted in Figure 3.12. The tunnel consists of six walls whose lengths are marked in the figure. All lengths are given in terms of “length units”, but they are basically centimeters. The figure also shows a 3-limb robot at its start and target positions. In this simulation we set the robot reachability radius to be $R = 60$ length units. The coefficient of friction is $\mu = 0.5$, a value that corresponds to rubber coated footpads contacting walls made of metal or perspex. Note that the simple tunnel already contains significant geometric features. The two walls at the tunnel’s bottom form a closing cone. The tunnel next turns leftward and becomes two parallel walls. Finally, the two walls at the tunnel’s top form an opening cone. These geometric features are significant, since *the robot must use friction effects to traverse such features*.

The walls are parametrized by path length in counterclockwise order (Figure 3.12).

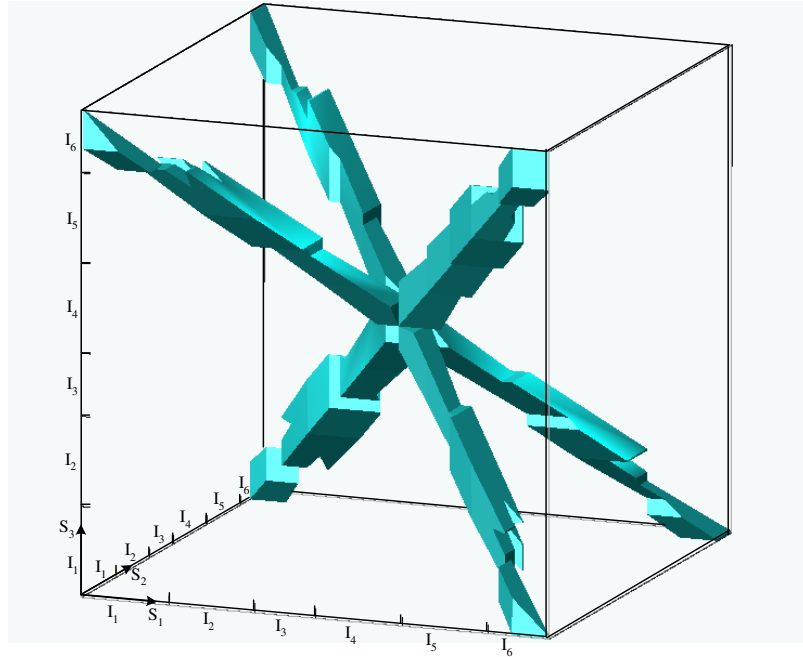


Figure 3.8: The collection of feasible 3-limb postures in contact c-space.
 אוסף כל התנוחות התלת-רגליות החוקיות במרחב קונפיגורציות המגע.

Thus $s = 0$ and $s = 270$ correspond to the bottom and top of the tunnel's right side, while $s = 270$ and $s = 540$ correspond to the top and bottom of the tunnel's left side. Using this parametrization, contact c-space consists of the cube $[0, 540]^3$, which is depicted in Figure 3.8. The center point of contact c-space at $(270, 270, 270)$ represents 3-limb postures where the three footpads touch the upper point of either side of the tunnel. Topologically, we ought to put a cube-shaped puncture at the center of contact c-space, since the top points on the left and right sides of the tunnel are physically distinct. The eight outer vertices of contact c-space represent 3-limb postures where the three footpads are located at the bottom part of the tunnel. These vertices represent the $2^3 = 8$ possible assignments of the three limbs to the tunnel's two sides. Note that the robot must contact both sides of the tunnel in order to generate an equilibrium posture. Hence the vertices $(0, 0, 0)$ and $(540, 540, 540)$ will

certainly lie outside the set of feasible 3-limb postures presented below. Topologically, when we introduce a small cube puncture at the center point, contact c-space becomes a set embedded in a three-dimensional torus. This fact has been noted in the context of 3-finger grasps by Leveroni and Salisbury [38].

Let us now turn to the computation of the feasible 3-limb postures in contact c-space. Figure 3.7 shows the collection of 2-limb equilibrium postures in the (s_i, s_j) plane. It can be seen that these postures form a *convex polygon* in each planar cell. The edges of these polygons consist of frictional equilibrium constraints and the cell's boundaries. Note that the figure is symmetric with respect to the $s_i = s_j$ axis, reflecting the possibility of switching the limbs between the two contacts. Figure 3.8 shows the collection of feasible 3-limb postures, consisting of intersection of pairs of prisms whose polygonal cross section appears in Figure 3.7. In this particular tunnel all prism intersections automatically satisfy the reachability constraint. (This is an artifact of our tunnel environment, coefficient of friction, and robot radius.) The collection of feasible 3-limb postures has a *six-fold symmetry* consisting of six symmetric “arms”: every non-empty cell represents an assignment of the three limbs to a triplet of walls, and there are six permutations of the three limbs on the triplet of walls. The arms are roughly aligned with the diagonals of contact c-space, and this can be explained as follows. The coordinate projection of each arm covers the entire length of the tunnel. Each arm can therefore be visualized as “dragging” the 3-limb mechanism as a single rigid body along the entire length of the tunnel. There are nine non-empty cells in each arm, giving a total of 54 non-empty cells in the entire contact c-space.

Next consider the approximation of the feasible 3-limb postures in each cell by p maximal cubes. We use $p = 5$ maximal cubes per cell and compute the maximal cubes

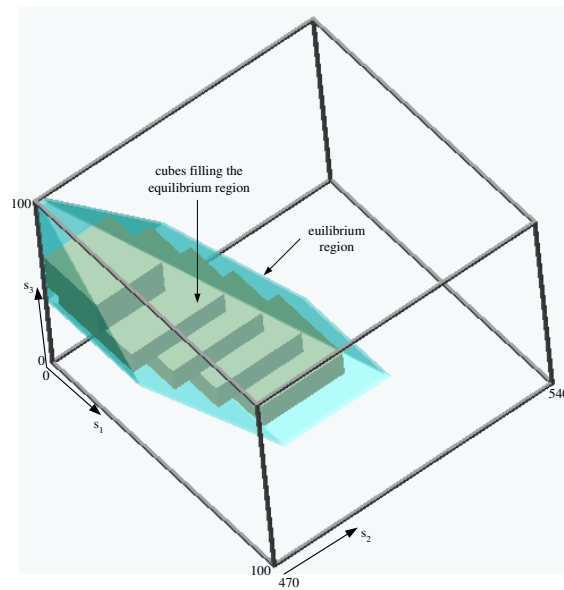


Figure 3.9: A five-cube approximation of the feasible 3-limb postures in the cell $I_1 \times I_6 \times I_1$.

קירוב באמצעות חמש תיבות של התנוחות התלת-רגליות החוקיות בתא $I_1 \times I_6 \times I_1$.

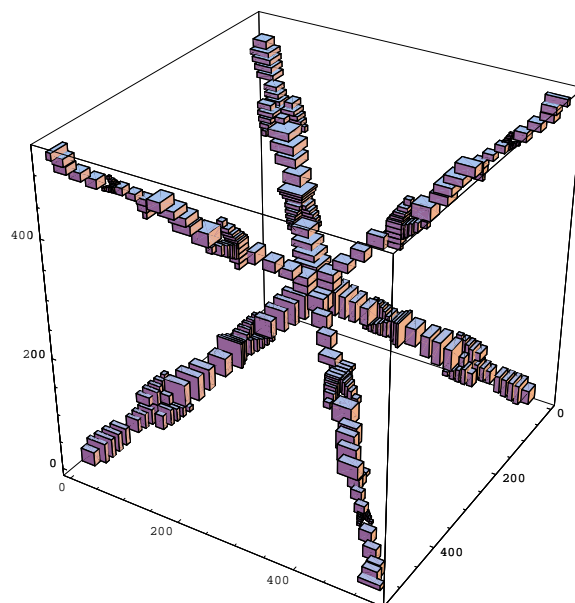


Figure 3.10: The collection of 270 maximal cubes approximating the feasible 3-limb postures.

אוסף 270 התיבות המקסימליות המקרבות את התנוחות התלת-רגליות החוקיות.

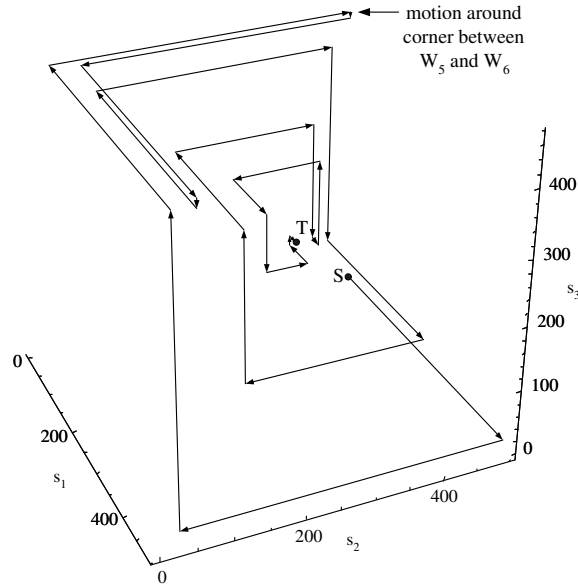


Figure 3.11: The shortest path from S to T along the edges of the sub-cube graph in contact c -space.

המסלול הקצר ביותר מ- S ל- T לאורך קשתות גרף תת-התיבות במרחב קונפיגורציות המגע.

using the ellipsoid algorithm. This value of p preserves the connectivity of the set of feasible 3-limb postures, while still being sufficiently low to allow reasonable execution time. Figure 3.9 shows the cube approximation of the feasible 3-limb postures in the cell $I_1 \times I_6 \times I_1$, where the relative configuration is specified by four separating planes orthogonal to the s_3 -axis. The result of running the ellipsoid algorithm on the non-empty cells in one arm of contact c -space appear in Figure 3.10. Since there are 54 non-empty cells, the resulting cube approximation of contact c -space contains $5 \cdot 54 = 270$ maximal cubes. The algorithm next partitions each of the maximal cubes along the separating planes of the other maximal cubes. The partitioning of the maximal cubes generated 28,299 sub-cubes in each of the six arms of contact c -space (the resulting sub-cubes are not shown).

The algorithm next constructs the sub-cube graph, assigns unit edge weights,

and searches the graph for the shortest path from the start to target postures. The result of computing the shortest path using Dijkstra's algorithm is shown in Figure 3.11. Each segment in the figure is an edge of the sub-cube graph that represents one limb lifting and re-placement. Figure 3.12 shows the same path in physical space, where each foothold is marked by its index in the sequence of steps taken by the robot. Let us denote the sequence of 3-limb postures by (i_1, i_2, i_3) , where i_j is the foothold position of limb j at the i^{th} 3-limb posture. Then the path computed by the algorithm consists of the 3-limb postures: $S = (1, 2, 3) \rightarrow (4, 2, 3) \rightarrow (4, 5, 3) \rightarrow (4, 5, 6) \rightarrow (7, 5, 6) \rightarrow (7, 8, 6) \rightarrow (7, 8, 9) \rightarrow (7, 10, 9) \rightarrow (11, 10, 9) \rightarrow (11, 10, 12) \rightarrow (13, 10, 12) \rightarrow (13, 14, 12) \rightarrow (13, 14, 15) \rightarrow (16, 14, 15) \rightarrow (16, 17, 15) \rightarrow (16, 17, 18) \rightarrow (19, 17, 18) \rightarrow (19, 20, 18) \rightarrow (19, 20, 21) \rightarrow (22, 20, 21) \rightarrow (22, 20, 23) \rightarrow (22, 24, 23) \rightarrow (25, 24, 23) \rightarrow (25, 24, 26) \rightarrow (25, 27, 26) \rightarrow (28, 27, 26) \rightarrow (28, 27, 29) \rightarrow T = (30, 27, 29)$. This sequence describes a 3-2-3 gait pattern, where successive 3-limb postures are interspersed by a 2-limb posture that allows motion of a limb between the two 3-limb postures. Note that the path generated by the algorithm is minimal in terms of the number of steps relative to the cube approximation of the feasible 3-limb postures (Figure 3.10). Note, too, that the short edge along the s_3 axis in Figure 3.11 corresponds to the transition $(7, 8, 6) \rightarrow (7, 8, 9)$. This edge takes the robot around the leftward turning corner between the walls W_5 and W_6 . The difficulty in accomplishing this maneuver can be appreciated by inspecting the narrow overlap between the planar cells $I_5 \times I_1$ and $I_6 \times I_1$ in Figure 3.7.

3.6.2 The Effect of Number of Maximal Cubes on Path Length

We run several simulation to investigate the effect of the selection of p , number of maximal cubes, on the path length in terms of total number of steps along the path.

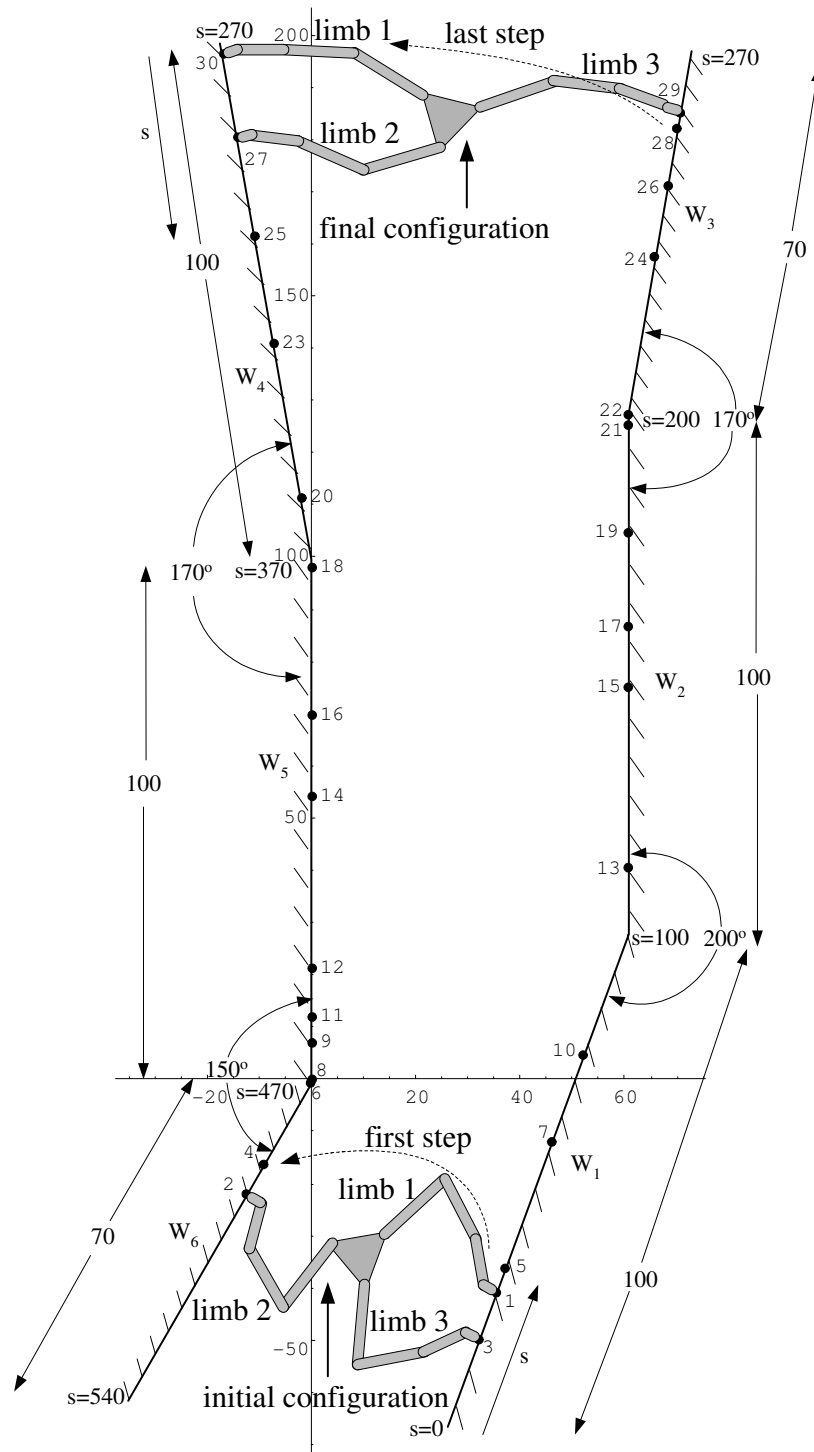


Figure 3.12: The tunnel environment used in the simulations, and the sequence of footholds generated by the PCG algorithm.

המנהרה אשר שימשה לסימולציות, וסידרת נקודות האחיזה אשר יוצרה ע"י אלגוריתם PCG

For these simulations we used robot reachability radius of $R = 77.2$ length units and coefficient of friction $\mu = 0.5$. We used the following two tunnels. The first tunnel is two parallel walls of length of 200 length units and the width of the tunnel between the wall is 115.8 length units. The second tunnel is in the shape of $> |$, where the right wall is in length of 150 length units and the left wall consists on two 80 length units segments with angle of 140° between the segments. The narrower part of this tunnel is 101.9 length units width. The results of running the PCG algorithm for $p = 2, 3, 4, 5, 6$ in these tunnels are shown in the following table.

p	number of steps in tunnel	number of steps in > tunnel
2	no path	no path
3	10	9
4	10	9
5	10	8
6	10	7

From this table we can conclude that after path was found with some p enlarging p may reduce the total number of steps but the amount of steps reduced will be small. Therefor if path was found with a given p there is no point to increase p dramatically since the effect of increasing p on the total number of steps along the path is minor.

3.7 Conclusion

We presented the PCG algorithm for selecting the foothold positions of a 3-limb robot in a planar tunnel environment. The algorithm assumes knowledge of the tunnel geometry and a lower bound on the amount of friction at the contacts. Using

this knowledge, we established that the feasible 3-limb postures consist of a union of convex sets in contact c -space. Using convex programming techniques, the PCG algorithm approximates the collection of feasible 3-limb postures by $O(np)$ maximal cubes, where n is the number of walls and p the number of cubes in each non-empty cell of contact c -space. The algorithm next partitions the cubes into sub-cubes and defines a graph whose nodes are sub-cubes and whose edges represent feasible motion of a limb between any 3-limb postures in the two sub-cubes. A shortest path search on the resulting graph generates a 3-2-3 gait sequence that moves the robot from start to target using a minimum number of foothold exchanges. In practical tunnel environments the PCG algorithm runs in $O(np^6 \log(np))$ time, and we demonstrated the execution of the algorithm in a tunnel. Experiments conducted in our laboratory show practical implementation of the PCG algorithm for selecting the foothold position of a real spider-robot in real tunnel environment.

The algorithm's main strength is its emphasize on achieving contact independent foothold placement sequences. Each sub-cube parametrizes three contact independent wall segments, and each edge can be realized by limb lifting and re-placement between any two postures in the two sub-cubes connected by the edge. Thus a controller for the robot's limbs need only ensure footpad placement within the segments parametrized by the sub-cubes. The main weakness of the algorithm is the lack of a procedure for selecting the parameter p . Instead we introduced an algorithm that determine a lower bound on p , but this lower bound is not necessarily tight. This parameter has to be sufficiently high to ensure that the resulting cube approximation induces a sub-cube graph whose connectivity reflects the connectivity of the feasible 3-limb postures in contact c -space. Yet it must not be too high as to require an unnecessary long computation time.

Finally consider the generalization of the PCG algorithm to robots with a higher number of limbs. In this case some modifications should be done in the algorithm to be suitable for k -limb mechanisms. It seems that the algorithm directly generalizes to k -limb mechanisms that move with a $k - (k - 1) - k$ gait pattern. Contact c -space in this case is k -dimensional, and one must first establish that the feasible k -limb postures in this space are a union of convex sets. If this is the case, the algorithm can be applied to such mechanisms without any change. However, the computational complexity of the algorithm would become $O(np^{k+3} \log(np))$ i.e., exponential in the number of limbs. A second more challenging topic is how to plan the foothold positions of a k -limb mechanism using a variable gait pattern. For instance, a 4-limb mechanism can move a single limb at a time, or two limbs at a time, resulting in a variable gait pattern. One possibility to generate variable gait pattern is by adding more edges to the graph that connect different $k - limb$ postures. However this will increase the algorithm complexity considerably. We are currently investigating foothold placement algorithms for such mechanisms, with the objective of generating a variable gait pattern that would minimize the number of steps from start to target and will take reasonable running time.

Chapter 4

Control of Spider-Like Robot

4.1 Introduction

The control problem associated with quasistatic locomotion of spider-like robots is as follows. Consider a k -limbed spider mechanism, such that each limb has n actuated degrees of freedom. The limbs are interconnected by a central base that has three *unactuated* degrees of freedom. A spider robot thus has $kn+3$ degrees of freedom, of which only kn degrees of freedom are actuated. If we regard the spider's configuration space as \mathbb{R}^{kn+3} , the control problem is how to induce forces and torques on the spider in order to bring it to a desired configuration in \mathbb{R}^{kn+3} . Existing solutions to the problem make specific assumptions either on the spider's structure or the environment's geometry. Roassman and Pfeiffer [60] assume that the spider limbs have a negligible mass relative to the central-base mass. This assumption induces a decoupling of the limbs and central-base dynamics, which allows in turn a control of the limbs' contact forces and the central-base's dynamics. It should be noted that Pfeiffer's objective is to control the limbs' contact forces with the tunnel walls,

while we seek to control the spider's configuration within the tunnel. Another control approach is proposed by Dubowsky et al. [14] in the context of ladder climbing. Using Impedance Control [24], they attach virtual springs to the spider footpads and central base such that the springs' set-points reflect the desired spider configuration. However, their approach seems to rely on the specific geometry of a ladder and lacks a formal proof of convergence.

In contrast, we present a control approach which is guaranteed to work no matter what is the mass distribution of the spider or the geometry of the environment. Our approach exploits the natural compliance in the contacts to stabilize the mechanism using two three or even more footholds. Since we have frictional contacts we first derive the contact stiffness matrix. The stiffness matrix presented in section 4.2 is based on model developed by Walton [78] that describe the contact force as function of the normal and tangential displacements for loading paths where the ration between the normal and tangential displacements is constant. In the preloading process we choose a loading path that meets this Walton loading path condition. The contact stiffness matrix is not symmetric and we show the condition for it's symmetric part to be positive definite, which is a key property that we need later on to prove the stability of the mechanism. Next we present the spider-robot dynamic equations. We introduce a simple decentralized PD controller for the actuated joints of the robot. Then we find the equilibrium point of the closed-loop system. Following we analyze the stability of the system using linearization about the equilibrium of the non-linear closed-loop system. The linearized dynamic system is asymmetric.

In the literature [29, p. 86] such asymmetric systems are called *circulatory systems*. Known results on the stability of circulatory systems are based on the symmetrizability of asymmetric matrix. Taussky [74] was the first to define symmetrizability of a

matrix. She also showed [75] that any real square matrix can be written as the product of two symmetric matrices. Huseyin [28, p. 174] applied Taussky's results to analyze the stability of circulatory systems. Additional results on the stability of circulatory systems based on the symmetrizability of asymmetric matrix can be found in [29, 1]. However finding the two symmetric matrices composing the asymmetric matrix is a numerical process and thus general analytic results on the stability of asymmetric systems are, to best of our knowledge, not exist. Therefore we develop criteria for the stability of asymmetric systems. These criteria are based on the fact that we consider system which its symmetric part is stable, then a small enough asymmetric part should not destroy the stability of the system. The proof of this result is inspired by the proof of stability for symmetric systems presented in [49, p. 192].

Other relevant papers that discuss robot's stiffness matrix are [10, 72], where they show the effect of internal forces in closed kinematics chains on the overall stiffness matrix. However, in these papers the overall stiffness matrix is symmetric.

In this work we introduce a computed lower bound on the stiffness of the PD controller in order to stabilize the symmetric system. Additionally an analytic criterion for the maximum allowed magnitude of the asymmetry of the system is developed.

4.2 Compliant Contact Model

We use a Compliant contact model for the forces occurs when two quasi-rigid bodies are pressed one against the other. We consider the case of contact between two spheres of radius R ¹, shear modulus G , and Poisson's ratio ν . Though in our case

¹For spheres of different radii R is the equivalent radius defined as $\frac{1}{R} = \frac{1}{R_1} + \frac{1}{R_2}$. Johnson [31, p. 92] defines an equivalent elastic modulus as well, where the shear modulus is function of the elastic

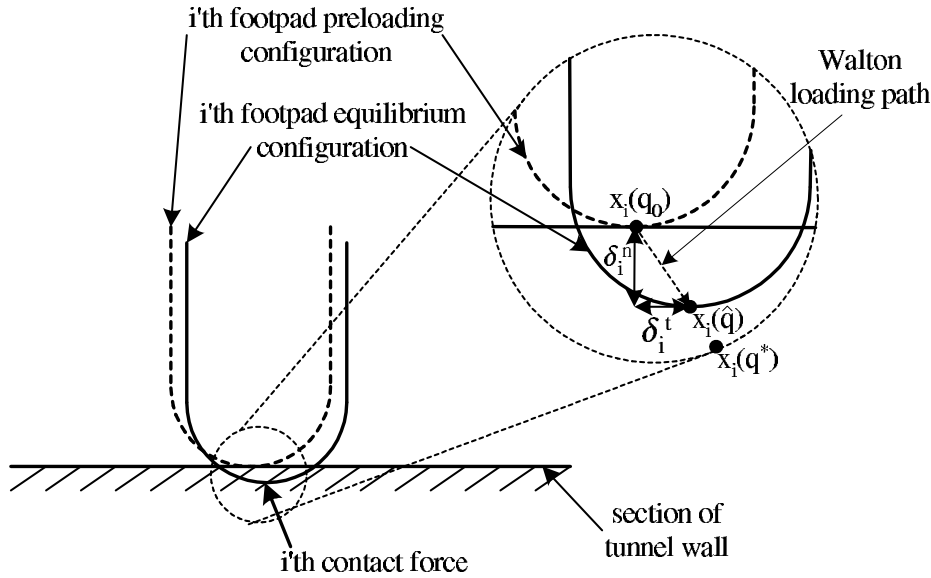


Figure 4.1: The interpenetration of the spider-robot's footpad and the tunnel wall.
החדירה ההדדית בין כף הרגל של רובוט העכביש ודופן המנהרה.

the footpad is not of sphere shape the contact force-displacement law should not differ dramatically from the case of contacting spheres. Moreover, if the contacting surfaces are rough then the asperities can be modelled as spheres and therefore we can use the contacting sphere model. The spheres are initially contact in a point with zero contact force. Then as external force presses the spheres one against the other the shapes of the spheres deform and they contact through an area. However if we consider the non-deformed spheres then we get that the initial contact point on the sphere displaced in $\delta = (\delta^n, \delta^t)$, where δ^n and δ^t are the normal and tangential displacements respectively (Figure 4.1). The compliant contact model is the relation between the contact force $f = (f^n, f^t)$ and the displacement $\delta = (\delta^n, \delta^t)$.

For the normal direction the Hertz model [31, 21], which has been verified theoretically and experimentally, establish that the normal traction over the circular contact modulus and Poisson's ratio.

area is given by

$$q^n = \frac{4G}{\pi R(1-\nu)}(R\delta^n - r^2)^{1/2}, \quad (4.1)$$

where r ($0 \leq r \leq \sqrt{R\delta^n}$) is the radial distance from the center of the contact area.

For the tangential direction Mindlin [45] showed that when two axially pressed spheres are further displaced tangentially, the contact area and the normal traction are unaffected and the axisymmetric tangential traction is given by

$$q^t = \frac{4G\delta^n}{\pi(2-\nu)}(R\delta^n - r^2)^{-1/2}.$$

However, for our application this loading path is not applicable, since we need to apply the loading force in both directions. In that case Walton [78] showed that for the special loading path where

$$\frac{\delta^t}{\delta^n} = c = \text{constant} \quad (4.2)$$

the tangential and normal tractions are given by

$$q^n = \frac{4G}{\pi R(1-\nu)}(R\delta^n - r^2)^{1/2}, \quad (4.3)$$

$$q^t = \frac{8Gc}{\pi R(2-\nu)}(R\delta^n - r^2)^{1/2}. \quad (4.4)$$

For this loading path the normal and tangential contact forces are computed by integrating the tractions over the contact area as follows,

$$f^n = \int_0^{\sqrt{R\delta^n}} q^n 2\pi r dr = \frac{8G\delta^n \sqrt{R\delta^n}}{3(1-\nu)}, \quad (4.5)$$

$$f^t = \int_0^{\sqrt{R\delta^n}} q^t 2\pi r dr = \frac{16Gc\delta^n \sqrt{R\delta^n}}{3(2-\nu)}. \quad (4.6)$$

4.2.1 The Contact Stiffness Matrix

For further analysis we use a first order approximation (or linearization) of the contact forces. The contact stiffness matrix is defined as

$$K = \begin{bmatrix} \frac{\partial f^n}{\partial \delta^n} & \frac{\partial f^n}{\partial \delta^t} \\ \frac{\partial f^t}{\partial \delta^n} & \frac{\partial f^t}{\partial \delta^t} \end{bmatrix} \quad (4.7)$$

By continuity argument we can assume that in the vicinity of Walton path (i.e. $\frac{\delta^t}{\delta^n} \approx c \neq \text{constant}$) the tractions and forces have the similar form as in equations (4.5,4.6).

The normal force is only a function of δ_n . Therefore it's derivatives are

$$\frac{\partial f^n}{\partial \delta^n} = \frac{4G\sqrt{R\delta^n}}{1-\nu}$$

and

$$\frac{\partial f^n}{\partial \delta^t} = 0.$$

To compute the partial derivatives of the tangential contact force we apply the derivative definition as follows

$$\frac{\partial f^t}{\partial \delta^n} = \lim_{\Delta \delta^n \rightarrow 0} \frac{f^t(\delta_0^n + \Delta \delta^n, \delta_0^t) - f^t(\delta_0^n, \delta_0^t)}{\Delta \delta^n}$$

and

$$\frac{\partial f^t}{\partial \delta^t} = \lim_{\Delta \delta^t \rightarrow 0} \frac{f^t(\delta_0^n, \delta_0^t + \Delta \delta^t) - f^t(\delta_0^n, \delta_0^t)}{\Delta \delta^t}.$$

From the geometric relations of figure (4.2) we can express f^t as function of δ^n and c rather than function of δ^n and δ^t . This will enable us to use the former Walton model. The relations are

$$f^t(\delta_0^n + \Delta \delta^n, \delta_0^t) = f^t(\delta_0^n + \Delta \delta^n, c - \Delta c)$$

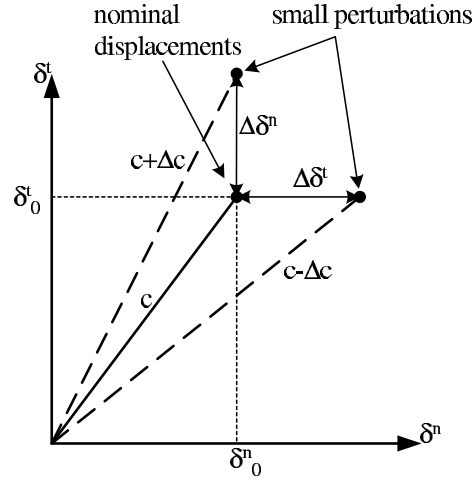


Figure 4.2: Schematic representation of the geometric relations in infinitesimal perturbations from the nominal penetration.

הצגה סכמטית של הקשרים הגיאומטריים עבור תזוזות אינפיניטיסימליות מהחדירה הנומינלית.

$$f^t(\delta_0^n, \delta_0^t + \Delta\delta^t) = f^t(\delta_0^n, c + \Delta c)$$

Recall that

$$f^t(\delta^n, c) = \frac{16Gc\delta^n\sqrt{R\delta^n}}{3(2-\nu)}.$$

Now we can write

$$\begin{aligned} \frac{\partial f^t}{\partial \delta^n} &= \lim_{\Delta\delta^n \rightarrow 0} \frac{f^t(\delta_0^n + \Delta\delta^n, c - \Delta c) - f^t(\delta_0^n, \delta_0^t)}{\Delta\delta^n} \\ &= \lim_{\Delta\delta^n \rightarrow 0} \frac{16G(c - \Delta c)(\delta_0^n + \Delta\delta^n)\sqrt{R(\delta_0^n + \Delta\delta^n)} - 16Gc\delta_0^n\sqrt{R\delta_0^n}}{3(2-\nu)\Delta\delta^n} \end{aligned}$$

From figure (4.2) we observe that

$$(c - \Delta c)(\delta_0^n + \Delta\delta^n) = \delta_0^t = c\delta_0^n.$$

For the $\sqrt{R(\delta_0^n + \Delta\delta^n)}$ term we use first order approximation (using Taylor series)

as follows

$$\sqrt{R(\delta_0^n + \Delta\delta^n)} = \sqrt{R\delta_0^n} + \frac{1}{2\sqrt{R\delta_0^n}}R\Delta\delta^n.$$

Substitute these results back yields

$$\begin{aligned}\frac{\partial f^t}{\partial \delta^n} &= \lim_{\Delta \delta^n \rightarrow 0} \frac{16Gc\delta_0^n (\sqrt{R\delta_0^n} + \frac{1}{2\sqrt{R\delta_0^n}} R\Delta\delta^n) - 16Gc\delta_0^n \sqrt{R\delta_0^n}}{3(2-\nu)\Delta\delta^n} \\ &= \frac{16Gc\delta_0^n R}{6\sqrt{R\delta_0^n}(2-\nu)} \\ &= \frac{8G\delta_0^t R}{3\sqrt{R\delta_0^n}(2-\nu)}\end{aligned}$$

Next we compute the derivative of f^t with respect to δ^t . We express f^t as function of δ^n and c then from the derivative definition we have

$$\begin{aligned}\frac{\partial f^t}{\partial \delta^t} &= \lim_{\Delta \delta^t \rightarrow 0} \frac{f^t(\delta_0^n, c+\Delta c) - f^t(\delta_0^n, c)}{\Delta \delta^t} \\ &= \lim_{\Delta \delta^t \rightarrow 0} \frac{16G(c+\Delta c)\delta_0^n \sqrt{R\delta_0^n} - 16Gc\delta_0^n \sqrt{R\delta_0^n}}{3(2-\nu)\Delta \delta^t} \\ &= \lim_{\Delta \delta^t \rightarrow 0} \frac{16G\Delta c\delta_0^n \sqrt{R\delta_0^n}}{3(2-\nu)\Delta \delta^t}.\end{aligned}$$

From figure(4.2) we find the following geometric relation,

$$\Delta \delta^t = (c + \Delta c)\delta_0^n.$$

Recall that $\delta^t = c\delta_0^n$. Thus from this relation we have

$$\Delta c = \frac{\Delta \delta^t}{\delta_0^n}$$

Substitute this relation back to the partial derivative of f^t yields

$$\begin{aligned}\frac{\partial f^t}{\partial \delta^t} &= \lim_{\Delta \delta^t \rightarrow 0} \frac{16G\Delta \delta^t \delta_0^n \sqrt{R\delta_0^n}}{3(2-\nu)\delta_0^n \Delta \delta^t} \\ &= \frac{16G\sqrt{R\delta_0^n}}{3(2-\nu)}.\end{aligned}$$

we conclude with the following stiffness matrix

$$K = \begin{bmatrix} \frac{4G\sqrt{R\delta_0^n}}{1-\nu} & 0 \\ \frac{8GR\delta^t}{3\sqrt{R\delta_0^n}(2-\nu)} & \frac{16G\sqrt{R\delta_0^n}}{3(2-\nu)} \end{bmatrix}. \quad (4.8)$$

Next we wish to examine the positive definiteness property of K . But since K is an asymmetric matrix we examine the positive definiteness of the symmetric part of

K . Denote $(K)_s = \frac{1}{2}(K + K^T)$ the symmetric part of K , and $(K)_{as} = \frac{1}{2}(K - K^T)$ the skew-symmetric part of K . The following lemma assert the conditions for which the symmetric part of of K is positive definite.

Proposition 4.2.1 (Positive definiteness of K) *Let $K \in \mathbb{R}^{2 \times 2}$ be a frictional contact stiffness matrix. Then for*

$$-\sqrt{\frac{12(2-\nu)}{(1-\nu)}} < \frac{\delta^t}{\delta^n} < \sqrt{\frac{12(2-\nu)}{(1-\nu)}}$$

$(K)_s$ is positive definite

Proof: Since K is not a symmetric matrix, we express K as sum of symmetric matrix, $(K)_s$ and a skew-symmetric matrix $(K)_{as}$. $Tr((K)_s)$ is the sum of $(K)_s$'s eigenvalues and it is positive for all $\delta^n > 0$. Thus if the multiplication of K_s 's eigenvalues is positive then all the eigenvalues are positive. The multiplication of $(K)_s$'s eigenvalues is simply $det((K)_s)$, and the condition for $(K)_s$'s positive definiteness is

$$\left| \begin{array}{cc} \frac{4G\sqrt{R\delta^n}}{1-\nu} & \frac{4GR\delta^t}{3\sqrt{R\delta^n}(2-\nu)} \\ \frac{4GR\delta^t}{3\sqrt{R\delta^n}(2-\nu)} & \frac{16G\sqrt{R\delta^n}}{3(2-\nu)} \end{array} \right| = \frac{16RG^2(12(\delta^n)^2(2-\nu) - (\delta^t)^2(1-\nu))}{9\delta^n(2-\nu)^2(1-\nu)} > 0.$$

Since the denominator is positive we demand positive nominator. It follow that

$$12(\delta^n)^2(2-\nu) > (\delta^t)^2(1-\nu).$$

Finally, the condition for $(K)_s$ to be positive definite is given by

$$-\sqrt{\frac{12(2-\nu)}{(1-\nu)}} < \frac{\delta^t}{\delta^n} < \sqrt{\frac{12(2-\nu)}{(1-\nu)}}.$$

□

Finally, note that the contact forces stiffness matrix is given in the contact reference frame (with respect to the definitions of δ^n and δ^t). A simple transformation of

the form

$$R^T(\gamma)KR(\gamma)$$

enables us to express K in a reference frame rotated by angle γ relative to the contact reference frame. In this formula $R(\gamma)$ is a rotation matrix of angle γ .

4.3 Control Law

We first describe the dynamics of spider robots, then present the control laws, and finally analyze their stability. The spider's configuration parameters are denoted as follows. The base configuration (position and orientation) is denoted $q_0 \in \mathbb{R}^3$. Each limb possesses n actuated joints, and the joints associated with the i^{th} limb are denoted $q_i \in \mathbb{R}^n$. The joint vector of the entire spider is denoted $\bar{q} \in \mathbb{R}^{kn}$, and the configuration of the entire spider (i.e. central-base configuration and joint values) is denoted $q = (q_0, \bar{q}) \in \mathbb{R}^{kn+3}$.

4.3.1 The Dynamics of k -Limbed Spider Robot

Our first task is to compute the inertia matrix of a k -limbed spider robot. Since the limbs are attached to a common central base, the position of the i^{th} limb is determined by the configuration parameters (q_0, q_i) . Hence the total kinetic energy of the mechanism, denoted $T(q, \dot{q})$, is given by

$$T(q, \dot{q}) = \frac{1}{2}\dot{q}_0^T M_0(q_0)\dot{q}_0 + \sum_{i=1}^k \frac{1}{2}(\dot{q}_0, \dot{q}_i)^T M_i(q_0, q_i) \begin{pmatrix} \dot{q}_0 \\ \dot{q}_i \end{pmatrix}, \quad (4.9)$$

where $M_0(p_0)$ is the central-base 3×3 inertia matrix, and $M_i(q_0, q_i)$ is the i^{th} limb $(n+3) \times (n+3)$ inertia matrix. However, in general $T(q, \dot{q}) = \frac{1}{2}\dot{q}^T M(q)\dot{q}$, where

$M(q)$ is the spider's *total inertia matrix*. Equation (4.9) thus implies that $M(q)$ is the symmetric positive-definite matrix:

$$M(q) = \begin{bmatrix} M_0 & M_{01} & M_{02} & \cdots & M_{0k} \\ M_{01}^T & M_{11} & 0 & \cdots & 0 \\ M_{02}^T & 0 & M_{22} & \cdots & 0 \\ \cdots & \cdots & \cdots & \cdots & \cdots \\ M_{0k}^T & 0 & 0 & \cdots & M_{kk} \end{bmatrix}_{(kn+3) \times (kn+3)}$$

where

$$M_i = \begin{bmatrix} 0 & M_{0i} \\ M_{0i}^T & M_{ii} \end{bmatrix}.$$

The inertia matrix has a special structure which reflects the spider's kinematics. The non-zero entries in the first row and column correspond to the kinematic coupling between the central-base and each limb, and the zero entries correspond to the lack of any coupling between the spider's limbs.

Next we describe the external forces and torques that act on the spider mechanism. First, the spider's actuators apply joint torques. These torques are denoted $(0, \tau)$, where $0 \in \mathbb{R}^3$ represents the absence of central-base actuation, and $\tau \in \mathbb{R}^{kn}$ represents the nk joint torques. Second, the tunnel walls apply reaction forces on the spider's holding footpads. Denote $2 \leq m \leq k$ the number of limbs that brace against the tunnel. Without loss of generality we assume the indices of the bracing limbs are in the range $0 \dots m$. Note that the $k - m$ limbs whose indices are $m \dots k$ are free and does not contact the environment. The net wrench due to these forces is given by $\sum_{i=1}^m J_i^T F_i$, where F_i is the i^{th} contact force and $J_i = Dx_i(q)$ is the Jacobian matrix of this contact. Finally, the spider's motion as a single rigid body incurs damping. This damping has three major sources. The first source for this damping is due to plastic

deformations and hysteresis at the contacts. Kumar et. al. [36, 35] first modelled the contact forces hysteresis as equivalent damping. The second source is viscoelastic losses due to material compression at the contacts [17]. The third source for this damping is caused since in our experimental apparatus the spider is supported by planar air bearings against a horizontal plane, and frictional losses in these bearings is an additional source of damping. Since only the central-base configuration q_0 varies when the spider moves as a single rigid body, we write these damping effects as $(-D_0\dot{q}_0, \vec{0})$, where D_0 is a 3×3 positive-definite matrix and $\vec{0} \in \mathbb{R}^{n_k}$. Summarizing all the external influences, the spider's dynamics is given by

$$M(q)\ddot{q} + B(q, \dot{q}) = \begin{pmatrix} 0 \\ \tau \end{pmatrix} - \begin{pmatrix} D_0\dot{q}_0 \\ \vec{0} \end{pmatrix} + \sum_{i=1}^m J_i^T F_i, \quad (4.10)$$

where $B(q, \dot{q}) = \dot{M}(q)\dot{q} - \frac{1}{2}\dot{q}^T(\frac{d}{dq}M(q))\dot{q}$ contains Coriolis and centrifugal forces.

4.3.2 The Control Law

We now present a control law for k -limbed spider robots. In order to bring all parts of a spider robot to a desired configuration, we induce forces and torque on the spider's unactuated central-base as follows. Consider for example the three-legged spider robot depicted in Figure 3.1. The spider brace against the tunnel walls using two limbs, and it has to bring its third limb to a new position specified by a higher-level motion planner. During this motion, all parts of the spider are free to move, *provided that the two footpads contacting the environment remain stationary with respect to each other*. The latter condition ensures that from the perspective of the tunnel walls, the spider remains grasped as a single rigid body throughout its motion. Since the spider hold itself in a stable frictional grasp the two footpads will settle at their original position

once the moving parts reach their destination. In order to realize this behavior, the motion planner specifies a sequence of target configurations to the robot controller, such that each target configuration is stable frictional grasp. The motion planner is not discussed in this paper. However, quasistatic motion paradigms for 3-legged spider robot is described in chapter 3. We now proceed with the description of the control law.

Let $q^* = (q_0^*, \bar{q}^*)$ denote the spider's desired configuration. Then the control law is the PD rule:

$$\tau(t) = -\bar{P}(\bar{q}(t) - \bar{q}^*) - D\dot{\bar{q}}(t), \quad (4.11)$$

where \bar{P} and D are $nk \times nk$ positive-definite matrices of proportional gains and damping coefficients. Note that the PD rule (4.11) requires no cancellation of the spider's nonlinear dynamics, and as such is simple to implement. Note, too, that in the case where \bar{P} and D are diagonal matrices, (4.11) becomes a *decentralized* control law, where each joint needs only measure its own angular state. This approach allows straightforward implementation of (4.11) using standard controller boards.

4.3.3 Equilibrium Point of the Spider-Robot System

Substituting the control law in the dynamical equation (4.10) gives the closed-loop system:

$$M(q)\ddot{q} + B(q, \dot{q}) = -P(q - q^*) + \sum_{i=1}^m J_i^T F_i - Q\dot{q}, \quad (4.12)$$

where $Q = \text{diag}(D_0, D)$ is a positive-definite damping matrix, and $P = \text{diag}(0_{3 \times 3}, \bar{P})$ is symmetric positive semi definite gain matrix. Our first task is to identify the static equilibrium point of (4.12). Substituting $\dot{q} = 0$ in (4.12) gives the equilibrium condition:

$$\sum_{i=1}^k \left(\frac{\partial}{\partial q_0} x_i(q_0, \bar{q}) \right)^T F_i = 0 \quad \text{and} \quad \sum_{i=1}^m \left(\frac{\partial}{\partial \bar{q}} x_i(q_0, \bar{q}) \right)^T F_i = -\bar{P}(\bar{q}(t) - \bar{q}^*). \quad (4.13)$$

By construction, the motion planner specifies an equilibrium posture for the spider, at which the footpads penetrate the tunnel walls by a small amount. This posture determines the desired spider configuration q^* which appears in the control laws. The equilibrium point of the closed-loop system is achieved by pressing the footpads against the tunnel walls at the specified contacts, until the equilibrium condition (4.13) is satisfied. The loading process is done by gradually increasing the penetrations δ_i^n and δ_i^t while holding the ratio $c_i = \frac{\delta_i^t}{\delta_i^n}$ constant. This loading path meet the requirement for walton path. Moreover, This loading path enables to increase the contact force magnitude while maintaining the same line of action for the force, as we have

$$c_i^f = \frac{F_i^t}{F_i^n} = c_i \frac{2(1 - \nu)}{(2 - \nu)}. \quad (4.14)$$

The first part of (4.13) requires that the net wrench on the central-base due to the tunnel's reaction forces be zero. The second part of (4.13) requires that the closed-loop joint actuators balance the joint torques induced by the tunnel's reaction forces. The following lemma establishes that such a balance can be achieved.

Lemma 4.3.1 *[Equilibrium point] Let q^* be a spider configuration at which m limbs ($2 \leq m \leq k$) press against the environment in an equilibrium posture. Let $P = \text{diag}(0_{3 \times 3}, \bar{P})$, and let $R(\gamma_i)$ be a rotation matrix by the i^{th} tunnel segment angle γ_i . Then first order approximation for an equilibrium configuration of the entire robot, \hat{q} , is given by*

$$\hat{q} = q^* + \left(P + \sum_{i=1}^m J_i^T R^T(\gamma_i) K_i R(\gamma_i) J_i \right)^{-1} \sum_{i=1}^m J_i^T F_i(\delta_i^*).$$

Provided that \hat{q} is sufficiently close to q^* to allow the approximation.

Proof: The conditions for equilibrium as shown in (4.13) are:

$$P(q - q^*) = \sum_{i=1}^m J_i^T F_i(\delta_i), \quad (4.15)$$

where $\delta_i = (\delta_i^n, \delta_i^t)$. In the vicinity of q^* we can use first order approximation to the contact forces as follows,

$$F_i(\delta_i) = F_i(\delta_i^*) - R^T(\gamma_i)K_iR(\gamma_i)(\delta_i - \delta_i^*),$$

where δ_i^* is the vector of footpad penetrations corresponding to q^* . the multiplication by $R(\gamma_i)$ and $R^T(\gamma_i)$ are used to convert the contact force and penetrations from the contact local frame to the global frame. Denote the i^{th} contact point correspond to zero penetration x_i^0 . Therefore we can write $\delta_i = x_i - x_i^0$ and $\delta_i^* = x_i^* - x_i^0$, where x_i^* is the i^{th} footpad position corresponding to q^* . Thus $\delta_i - \delta_i^*$ becomes $x_i - x_i^*$, and if x_i is close to x_i^* then $x_i - x_i^* \approx J_i(q_i - q_i^*)$. substituting these results back to (4.15) yields

$$P(q - q^*) = \sum_{i=1}^m J_i^T F_i(\delta_i^*) - J_i^T R^T(\gamma_i)K_iR(\gamma_i)J_i(q_i - q_i^*).$$

Rearranging this equation gives the equilibrium configuration

$$\hat{q} = q^* + \left(P + \sum_{i=1}^m J_i^T R^T(\gamma_i)K_iR(\gamma_i)J_i \right)^{-1} \sum_{i=1}^m J_i^T F_i(\delta_i^*).$$

Finally, note that the matrix $(P + \sum_{i=1}^m J_i^T R^T(\gamma_i)K_iR(\gamma_i)J_i)$ is invertible since P has full rank with respect to \bar{q} and $\sum_{i=1}^m J_i^T R^T(\gamma_i)K_iR(\gamma_i)J_i$ has full rank with respect to q_0 . \square

4.3.4 Linearization of Spider-Robot System About Equilibrium

Nonlinear system has equivalent stability property as the linearized system. Therefore For further analysis of the nonlinear system stability property we will analyze the stability property of the linearized system. Next we develop the terms for the linearized system. The nonlinear system as in (4.12) can be written in reduced order as:

$$\begin{aligned}\dot{p}_1 &= p_2 \\ \dot{p}_2 &= M^{-1}(p_1) \left(-B(p_1, p_2) - P(p_1 - p_1^0) - Qp_2 + \sum_{i=1}^m J_i^T(p_1)F_i(p_1) \right).\end{aligned}\tag{4.16}$$

For system of the form $\dot{p} = f(p)$ the linearized system about an equilibrium point, \hat{p} , defined as

$$\delta\dot{p} = \left. \frac{df}{dp} \right|_{p=\hat{p}} \delta p,$$

where $\delta p = p - \hat{p}$. The equilibrium point \hat{p} satisfies $f(\hat{p}) = 0$. \hat{p} can be divided to two parts $\hat{p} = (\hat{p}_1, \hat{p}_2)$. Note that in mechanical systems p_2 is the generalized velocities and therefore $\hat{p}_2 = 0$. In (4.16) all the terms in $B(p_1, p_2)$ are quadratic in the generalized velocities and vanish in the linearization. Thus the linearized system is

$$\begin{aligned}\delta\dot{p}_1 &= \delta p_2 \\ \delta\dot{p}_2 &= M^{-1}(\hat{p}_1) \left[-P + \sum_{i=1}^m \left(-J_i^T(\hat{p}_1)R^T(\gamma_i)K_iR(\gamma_i)J_i(\hat{p}_1) + D^2x_i(\hat{p}_1)F_i(\hat{p}_1) \right) \right] \delta p_1 \\ &\quad - M^{-1}(\hat{p}_1)Q\delta p_2,\end{aligned}$$

where $D^2x_i(\hat{p}_1)$ is a third order tensor and by multiplying it by the contact force $F_i(\hat{p}_1)$ we get a $nk \times nk$ matrix. rewriting the above system in matrix format yields

$$\delta\dot{p} = \begin{bmatrix} 0 & I \\ M^{-1} \left[-P - \sum_{i=1}^m \left(J_i^T R_i^T K_i R_i J_i - D^2x_i(\hat{p}_1)F_i \right) \right] & -M^{-1}Q \end{bmatrix} \delta p.$$

Another option to write this linear system is as follows

$$M\delta\ddot{q} + Q\delta\dot{q} + \underbrace{\left[P + \sum_{i=1}^m (J_i^T R_i^T K_i R_i J_i - D^2 x_i(\hat{q}) F_i) \right]}_{\tilde{K}} \delta q = 0, \quad (4.17)$$

where $\delta q = q - \hat{q}$.

General results [34, 33, 11, 49] of the stability of such systems consider the case where M, Q and \tilde{K} are symmetric matrices. In this case if Q and \tilde{K} are positive definite then the system is asymptotically stable. However in our case K_i is asymmetric and that cause the entire proportional gain, \tilde{K} , to be asymmetric, so the general result cannot be applied here. Other results on asymmetric systems [74, 28, 29, 1] analyze the system stability using symmetrization of the asymmetric matrix. Note that this symmetrization process is numeric and therefore can not give us any insight on the general conditions for the stability of the system. In the next section stability analysis of our linearized system will be considered.

4.4 Stability Analysis

In this section we analyze the equilibrium stability of the spider-robot closed loop system. Since the compliant contacts produce asymmetric stiffness matrix we first develop the condition for asymmetric linear system to be asymptotically stable. Then we apply these condition to our closed-loop system.

4.4.1 Stability of 2^{nd} -Order Asymmetric Linear Systems

Consider the following second order linear asymmetric dynamic system

$$\ddot{p} + K_v \dot{p} + K_p p = 0, \quad (4.18)$$

where $K_v \in \mathbb{R}^{n \times n}$ is symmetric positive definite matrix and $K_p \in \mathbb{R}^{n \times n}$ is asymmetric matrix, while it's symmetric part $(K_p)_s \in \mathbb{R}^{n \times n}$ is positive definite. The following Theorem states that if the skew-symmetric part of K_p is small enough and the symmetric part of K_p is positive definite then the system (4.18) is asymptotically stable.

Theorem 7 (Stability of asymmetric system) *Consider the system of (4.18). Let $\beta \in \mathbb{R}$ be the minimal eigenvalue of $K_v \in \mathbb{R}^{n \times n}$. Let $\alpha \in \mathbb{R}$ be the minimal eigenvalue of the symmetric part of $K_p \in \mathbb{R}^{n \times n}$, and let $\omega \in \mathbb{R}$ be the matrix norm² of the skew-symmetric part of K_p . Then if*

$$|\omega| < \sqrt{\alpha\beta}$$

the system is asymptotically stable.

Proof: System (4.18) can be written as a first-order linear system:

$$\frac{d}{dt} \begin{pmatrix} p \\ \dot{p} \end{pmatrix} = \underbrace{\begin{bmatrix} 0 & I \\ -K_p & -K_v \end{bmatrix}}_A \begin{pmatrix} p \\ \dot{p} \end{pmatrix}$$

For asymptotic stability it suffice to show the conditions for which the real part of each of the eigenvalues of A is negative. Let $\lambda \in \mathbb{C}$ be an eigenvalue of A with corresponding eigenvector $v = (v_1, v_2) \in \mathbb{C}^{2n}$, $v \neq 0$. Then,

$$\lambda \begin{pmatrix} v_1 \\ v_2 \end{pmatrix} = \begin{bmatrix} 0 & I \\ -K_p & -K_v \end{bmatrix} \begin{pmatrix} v_1 \\ v_2 \end{pmatrix} = \begin{pmatrix} v_2 \\ -K_p v_1 - K_v v_2 \end{pmatrix}.$$

It follows that if $\lambda = 0$ then $v = \vec{0}$, and hence $\lambda = 0$ is not an eigenvalue of A . Further, if $\lambda \neq 0$, then $v_2 = \vec{0}$ implies that $v_1 = \vec{0} \geq$. Thus, $v_1, v_2 \neq 0$ and we may

²The matrix norm is defined as $\|E\| = \max\{\|Eu\|\}$ over all vectors $\|u\| \leq 1$ [26, p. 293].

assume without loss of generality that $\|v_1\| = 1$. Using this we write

$$\lambda^2 = v_1^* \lambda^2 v_1 = v_1^* \lambda v_2 = v_1^* (-K_p v_1 - K_v v_2) = -v_1^* K_p v_1 - \lambda v_1^* K_v v_1, \quad (4.19)$$

where $*$ denotes the complex conjugate transpose. Since K_v is symmetric positive definite matrix we can write $\tilde{\beta} = v_1^* K_v v_1 > 0$. Next K_p will be written as $K_p = (K_p)_s + (K_p)_{as}$. Then $\tilde{\alpha} = v_1^* (K_p)_s v_1 > 0$, and $i\tilde{\omega} = v_1^* (K_p)_{as} v_1$, where $i = \sqrt{-1}$. Substituting these results to (4.19) yields

$$\lambda^2 + \tilde{\beta}\lambda + \tilde{\alpha} + i\tilde{\omega} = 0. \quad (4.20)$$

Note that every eigenvalue of A satisfies this equation. Therefore if we demand negative real part of the solutions of (4.20) then we assure the stability of the system (4.18). The solutions for (4.20) are:

$$\lambda_{1,2} = \frac{1}{2} \left(-\tilde{\beta} \pm \sqrt{\tilde{\beta}^2 - 4(\tilde{\alpha} + i\tilde{\omega})} \right). \quad (4.21)$$

The second term here is square root of a complex number. Consider for instance the complex number $z = a + ib$. The absolute of z is $\sqrt{a^2 + b^2}$ and it's argument is $\theta = \arctan\left(\frac{b}{a}\right)$. Then $\sqrt{z} = \pm(a^2 + b^2)^{\frac{1}{4}} \angle \frac{\theta}{2}$, and in cartesian representation $\sqrt{z} = \pm(a^2 + b^2)^{\frac{1}{4}} \left(\cos\left(\frac{\theta}{2}\right) + i \sin\left(\frac{\theta}{2}\right) \right)$. Additionally we have $\cos(\theta) = \frac{a}{\sqrt{a^2 + b^2}}$, and the trigonometric identity $\cos\left(\frac{\theta}{2}\right) = \sqrt{\frac{1 + \cos(\theta)}{2}}$. Therefore

$$\operatorname{Re}\{\sqrt{z}\} = \pm(a^2 + b^2)^{\frac{1}{4}} \left(\frac{1}{2} + \frac{1}{2} \frac{a}{\sqrt{a^2 + b^2}} \right)^{\frac{1}{2}},$$

where in our case $a = \tilde{\beta}^2 - 4\tilde{\alpha}$ and $b = 4\tilde{\omega}$. Utilizing this result to (4.21) implies that

$$\operatorname{Re}\{\lambda_{1,2}\} = \frac{1}{2} \left[-\tilde{\beta} \pm \left((\tilde{\beta}^2 - 4\tilde{\alpha})^2 + 16\tilde{\omega}^2 \right)^{\frac{1}{4}} \left(\frac{1}{2} + \frac{1}{2} \frac{(\tilde{\beta}^2 - 4\tilde{\alpha})}{\sqrt{(\tilde{\beta}^2 - 4\tilde{\alpha})^2 + 16\tilde{\omega}^2}} \right)^{\frac{1}{2}} \right].$$

In order to have $\text{Re}\{\lambda_{1,2}\} < 0$ we need

$$\tilde{\beta} > \left((\tilde{\beta}^2 - 4\tilde{\alpha})^2 + 16\tilde{\omega}^2 \right)^{\frac{1}{4}} \left(\frac{1}{2} + \frac{1}{2} \frac{(\tilde{\beta}^2 - 4\tilde{\alpha})}{\sqrt{(\tilde{\beta}^2 - 4\tilde{\alpha})^2 + 16\tilde{\omega}^2}} \right)^{\frac{1}{2}}.$$

Taking the square of both sides and then multiply the inequality by 2 gives

$$2\tilde{\beta}^2 > \left((\tilde{\beta}^2 - 4\tilde{\alpha})^2 + 16\tilde{\omega}^2 \right)^{\frac{1}{2}} \left(1 + \frac{(\tilde{\beta}^2 - 4\tilde{\alpha})}{\sqrt{(\tilde{\beta}^2 - 4\tilde{\alpha})^2 + 16\tilde{\omega}^2}} \right).$$

Rearranging this inequality results in

$$2\tilde{\beta}^2 > \left((\tilde{\beta}^2 - 4\tilde{\alpha})^2 + 16\tilde{\omega}^2 \right)^{\frac{1}{2}} + \tilde{\beta}^2 - 4\tilde{\alpha}.$$

Next we add $4\tilde{\alpha} - \tilde{\beta}^2$ to both sides and then take the square of both sides to have

$$\left(4\tilde{\alpha} + \tilde{\beta}^2 \right)^2 > \left(\tilde{\beta}^2 - 4\tilde{\alpha} \right)^2 + 16\tilde{\omega}^2.$$

Opening the brackets gives

$$16\tilde{\alpha}^2 + \tilde{\beta}^4 + 8\tilde{\alpha}\tilde{\beta}^2 > \tilde{\beta}^4 + 16\tilde{\alpha}^2 - 8\tilde{\alpha}\tilde{\beta}^2 + 16\tilde{\omega}^2.$$

Rearranging this and dividing by 16 results in

$$\tilde{\alpha}\tilde{\beta}^2 > \tilde{\omega}^2,$$

or simply

$$\sqrt{\tilde{\alpha}}\tilde{\beta} > |\tilde{\omega}|.$$

Recall that $\tilde{\beta} = v_1^* K_v v_1 > 0$, $\tilde{\alpha} = v_1^* (K_p)_s v_1 > 0$, and $i\tilde{\omega} = v_1^* (K_p)_{as} v_1$. Next we wish this inequality hold for every $\tilde{\alpha}$, $\tilde{\beta}$, and $i\tilde{\omega}$. In other words this inequality should be true for every eigenvalue λ and the associated eigenvector \vec{v} . Therefore we may bound $\tilde{\alpha}$ and $\tilde{\beta}$ by their minimal values α and β respectively. Note that

$$0 < \alpha = \lambda_{\min}((K_p)_s) = \lambda_{\min}((K_p)_s) \|v_1\|^2 \leq v_1^* (K_p)_s v_1 = \tilde{\alpha},$$

and

$$0 < \beta = \lambda_{\min}(K_v) = \lambda_{\min}(K_v) \|v_1\|^2 \leq v_1^* K_v v_1 = \tilde{\beta}.$$

Additionally we bound $\tilde{\omega}$ by it's maximal value ω as follows

$$|\omega| = \|(K_p)_{as}\| = \|v_1^*\| \|(K_p)_{as}\| \|v_1\| \geq |v_1^*(K_p)_{as}v_1| = |i\tilde{\omega}| = |\tilde{\omega}|$$

Finally we have that if $\omega < \sqrt{\alpha}\beta$ then for every $\tilde{\alpha}$, $\tilde{\beta}$, and $i\tilde{\omega}$ the inequality $\sqrt{\tilde{\alpha}\tilde{\beta}} > |\tilde{\omega}|$ holds true. This causes $\text{Re}\{\lambda\} < 0$ for every eigenvalue, λ , of A . That results with an asymptotically stable system (4.18). \square

Next we discuss the expansion of theorem 7 to the case where inertia matrix exists.

Consider the system

$$M\ddot{p} + K_v\dot{p} + K_p p = 0, \tag{4.22}$$

where all the parameters are as before except for the existence of positive definite symmetric matrix $M \in \mathbb{R}^{n \times n}$. In that case the following corollary establish the condition for the stability of (4.22).

Corollary 4.4.1 *Consider the system of (4.22). Let $\beta > 0$ be the minimal eigenvalue of $M^{-1/2}K_vM^{-1/2}$. Let $\alpha > 0$ be the minimal eigenvalue of $M^{-1/2}(K_p)_sM^{-1/2}$ and let $\omega \in \mathbb{R}$ be the matrix norm of $M^{-1/2}(K_p)_{as}M^{-1/2}$. Then if*

$$|\omega| < \sqrt{\alpha}\beta$$

the system is asymptotically stable.

Proof: We define a coordinate transformation as:

$$\tilde{p} = M^{1/2}p \text{ or } p = M^{-1/2}\tilde{p}.$$

This transformation is based on similar transformation found in [29, p. 87]. Note that the matrices $M^{1/2}$ and $M^{-1/2}$ are unique, symmetric, and positive definite. Moreover,

we have $M = M^{1/2}M^{1/2}$ and $M^{-1} = M^{-1/2}M^{-1/2}$. Substitute the new coordination back to (4.22) results in

$$M^{1/2}\ddot{\tilde{p}} + K_v M^{-1/2}\dot{\tilde{p}} + K_p M^{-1/2}\tilde{p} = 0.$$

Now we multiply this equation by $M^{-1/2}$ and have

$$\ddot{\tilde{p}} + \underbrace{M^{-1/2}K_v M^{-1/2}}_{\tilde{K}_v} \dot{\tilde{p}} + \underbrace{M^{-1/2}K_p M^{-1/2}}_{\tilde{K}_p} \tilde{p} = 0.$$

This system is exactly of the form used for theorem 7, but instead K_v and K_p we have now \tilde{K}_v and \tilde{K}_p respectively. Note that if the latter system is asymptotically stable it implies that (4.22) is asymptotically stable since they differ only by unique coordinate transformation. The rest of the proof is straight forward implementation of theorem 7. \square

4.4.2 Equilibrium Stability of k -Limbed Spider-Robot

The following theorem establishes a sufficient conditions for the local asymptotic stability of \hat{q} under the PD control law. This stability result is a key contribution of this thesis.

Theorem 8 (Spider-robot stability) *Let a k -limbed spider mechanism brace against the environment with $2 \leq m \leq k$ limbs in an equilibrium configuration $\hat{q} \in \mathbb{R}^{nk+3}$.*

Thus under PD control law (4.11), if the following three conditions,

$$\begin{aligned} \beta &= \lambda_{\min} (M^{-1/2}QM^{-1/2}) > 0 \\ \alpha &= \lambda_{\min} (M^{-1/2}(\tilde{K})_s M^{-1/2}) > 0 \\ \omega &= \|M^{-1/2}(\tilde{K})_{as} M^{-1/2}\| < \sqrt{\alpha}\beta \end{aligned}$$

*are satisfied then the zero-velocity state $(\hat{q}, 0)$ of the closed loop system (4.12) is **locally asymptotically stable**.*

Proof: We show that the linearized system about the equilibrium is asymptotically stable and conclude that the non-linear system is locally asymptotically stable. Recall from equation (4.17) the linearized system about the equilibrium as follows:

$$M\delta\ddot{q} + Q\delta\dot{q} + \tilde{K}\delta q = 0. \quad (4.23)$$

This system falls exactly to the form of systems considered in corollary 4.4.1. According to the corollary the conditions for such system to be asymptotically stable are as follows. First we need $\beta = \lambda_{\min}(M^{-1/2}QM^{-1/2})$ to be positive. Second we need $\alpha = \lambda_{\min}(M^{-1/2}(\tilde{K})_sM^{-1/2})$ to be positive. And the third condition for stability is $\omega = \|M^{-1/2}(\tilde{K})_{as}M^{-1/2}\| < \sqrt{\alpha}\beta$. \square

Next we show how and if these conditions can be satisfied by a k -limbed spider robot.

To satisfy the **first condition** we need $\lambda_{\min}(M^{-1/2}QM^{-1/2}) > 0$. As defined in subsection 4.3.3 Q is symmetric positive definite matrix. The following lemma assert that the transformation $M^{-1/2}QM^{-1/2}$ does not change the positive definiteness property of Q .

Lemma 4.4.2 *Let $M \in \mathbb{R}^{n \times n}$ be a symmetric positive definite matrix, and let $A \in \mathbb{R}^{n \times n}$ be a symmetric matrix. Thus if A is positive definite $M^{-1/2}AM^{-1/2}$ is positive definite.*

Proof: If A is positive definite then

$$v^T Av > 0 \quad \forall \vec{v} \neq 0. \quad (4.24)$$

And we need to show that

$$v^T M^{-1/2}AM^{-1/2}v > 0 \quad \forall \vec{v} \neq 0. \quad (4.25)$$

Note that since $M^{-1/2}$ is unique it is also symmetric. Therefore we can assign $\vec{u} = M^{-1/2}v$ and rewrite (4.25) as

$$u^T Au,$$

but from (4.24) we know this term is positive for $\vec{u}, \vec{v} \neq 0$. \square

To satisfy the **second condition** we need $M^{-1/2}(\tilde{K})_s M^{-1/2}$ to be positive definite. Applying lemma 4.4.2 enables us to prove that $(\tilde{K})_s$ is positive definite while positive definiteness of $M^{-1/2}(\tilde{K})_s M^{-1/2}$ is approved by the lemma. Recall from (4.17) that

$$(\tilde{K})_s = \left(P + \sum_{i=1}^m (J_i^T R_i^T K_i R_i J_i - D^2 x_i(\hat{q}_1) F_i) \right)_s.$$

K_i can be decomposed as follows,

$$K_i = (K_i)_s + (K_i)_{as}.$$

Thus the term $J_i^T R_i^T (K_i)_s R_i J_i$ is symmetric since

$$(J_i^T R_i^T (K_i)_s R_i J_i)^T = J_i^T R_i^T ((K_i)_s)^T R_i J_i = J_i^T R_i^T (K_i)_s R_i J_i,$$

and $J_i^T R_i^T (K_i)_{as} R_i J_i$ is skew-symmetric since

$$(J_i^T R_i^T (K_i)_{as} R_i J_i)^T = J_i^T R_i^T ((K_i)_s)^T R_i J_i = -J_i^T R_i^T (K_i)_{as} R_i J_i.$$

The term $D^2 x_i(\hat{q}_1) F_i$ is symmetric because of the following. $D^2 x_i(\hat{q}_1) F_i$ is the derivative of $J_i^T F_i$ with respect to q , while holding F_i constant. Now we specifically write

$$J_i^T F_i = \begin{bmatrix} \frac{\partial x_1}{\partial q_1} & \frac{\partial x_2}{\partial q_1} \\ \vdots & \vdots \\ \frac{\partial x_1}{\partial q_n} & \frac{\partial x_2}{\partial q_n} \end{bmatrix} \begin{pmatrix} f_1 \\ f_2 \end{pmatrix} = \begin{pmatrix} \sum \frac{\partial x_i}{\partial q_1} f_i \\ \vdots \\ \sum \frac{\partial x_i}{\partial q_n} f_i \end{pmatrix},$$

where for simplicity we denote here $x_i = (x_1, x_2)$ and $F_i = (f_1, f_2)$. Next we take this term's derivative as follows,

$$\frac{\partial}{\partial q} \begin{pmatrix} \sum \frac{\partial x_i}{\partial q_1} f_i \\ \vdots \\ \sum \frac{\partial x_i}{\partial q_n} f_i \end{pmatrix} = \begin{bmatrix} \sum \frac{\partial^2 x_i}{\partial q_1^2} f_i & \cdots & \sum \frac{\partial^2 x_i}{\partial q_1 \partial q_n} f_i \\ \vdots & & \vdots \\ \sum \frac{\partial^2 x_i}{\partial q_n \partial q_1} f_i & \cdots & \sum \frac{\partial^2 x_i}{\partial q_n^2} f_i \end{bmatrix}$$

It is easy to see that this matrix is symmetric. so we can conclude that

$$(\tilde{K})_s = P + \sum_{i=1}^m (J_i^T R_i^T (K_i)_s R_i J_i - D^2 x_i(\hat{q}_1) F_i).$$

Next we discuss the positive definiteness of $(\tilde{K})_s$. As in the frictionless contacts case [64, 69, 65] we show that if the grasp of the mechanism as solid body by the compliant tunnel is stable then for controller stiffness above lower bound the entire system stiffness matrix will be positive definite. Since coupling exists between each limb and the central-base but not between the limbs themselves, the term for $(\tilde{K})_s$ takes the form of

$$(\tilde{K})_s = \begin{bmatrix} \tilde{K}_{00} & \tilde{K}_{01} & \tilde{K}_{02} & \cdots & \tilde{K}_{0k} \\ \tilde{K}_{01}^T & \tilde{K}_{11} + P_1 & 0 & \cdots & 0 \\ \tilde{K}_{02}^T & 0 & \tilde{K}_{22} + P_2 & \cdots & 0 \\ \cdots & \cdots & \cdots & \cdots & \cdots \\ \tilde{K}_{0k}^T & 0 & 0 & \cdots & \tilde{K}_{kk} + P_k \end{bmatrix}.$$

Note that the 3×3 submatrix K_{00} represents the stiffness of the equilibrium posture when the mechanism is considered as a single rigid body and the tunnel represent k fingers of stiffness $(K_i)_s$ which grasp the mechanism as rigid body. The general formula for K_{00} was discussed in chapter 2 can be found in lemma 2.3.1. Let us assume for simplicity that $P_i = \sigma_i I_{n \times n}$ for $i = 1, \dots, k$, where σ_i is a positive parameter.

In order to establish lower bounds on the σ_i 's which guarantee that $(\tilde{K})_s$ is positive definite. Let $v = (v_0, v_1, \dots, v_k)$ be a vector in $\mathbb{R}^{n^{k+3}}$, such that $v_0 \in \mathbb{R}^3$ and $v_i \in \mathbb{R}^n$ for $i = 1, \dots, k$; and let $\sigma = (\sigma_1, \dots, \sigma_k)$. Then the quadratic form $v^T(\tilde{K})_s v$ can be written as:

$$v^T(\tilde{K})_s v = v_0^T \tilde{K}_{00} v_0 + 2 \sum_{i=1}^k v_0^T \tilde{K}_{0i} v_i + \sum_{i=1}^k v_i^T (\tilde{K}_{ii} + \sigma_i I) v_i.$$

Note that $v^T(\tilde{K})_s v = v_0^T \tilde{K}_{00} v_0$ when $v_i = 0$ for $i = 1, \dots, k$. Hence the positive definiteness of \tilde{K}_{00} is necessary for the positive definiteness of $(\tilde{K})_s$. Since the mechanism hold itself as a single rigid body, Lemma 2.3.1 implies that \tilde{K}_{00} has to be positive definite in order to have stable holing posture. Thus *the tunnel should stably grasp the mechanism as a single rigid body*. Let $\sigma_0 > 0$ denote the minimal eigenvalue of \tilde{K}_{00} and, for a given matrix E , let $\|E\|$ denote the matrix norm induced by the Euclidean norm³. Then $v^T(\tilde{K})_s v$ can be bounded as follows

$$v^T(\tilde{K})_s v \geq \sigma_0 \|v_0\|^2 - 2 \sum_{i=1}^k \|\tilde{K}_{0i}\| \|v_0\| \|v_i\| + \sum_{i=1}^k (\sigma_i - \|\tilde{K}_{ii}\|) \|v_i\|^2. \quad (4.26)$$

The first two summands in (4.26) can be written as follows

$$\begin{aligned} \sigma_0 \|v_0\|^2 - 2 \sum_{i=1}^k \|\tilde{K}_{0i}\| \|v_0\| \|v_i\| &= \sigma_0 \sum_{i=1}^k (\|v_0\|^2 - 2c_i \|v_0\| \|v_i\|) \\ &= \sigma_0 \sum_{i=1}^k \{(\|v_0\| - c_i \|v_i\|)^2 - c_i^2 \|v_i\|^2\}, \end{aligned}$$

where $c_i = \|\tilde{K}_{0i}\|/\sigma_0$. Substituting this expression in the quadratic form (4.26) gives:

$$v^T(\tilde{K})_s v \geq \sum_{i=1}^k \sigma_0 (\|v_0\| - c_i \|v_i\|)^2 + (\sigma_i - \|\tilde{K}_{ii}\| - \frac{1}{\sigma_0} \|\tilde{K}_{0i}\|^2) \|v_i\|^2. \quad (4.27)$$

Since $\sigma_0 > 0$, the right side of (4.27) is positive if the coefficient of $\|v_i\|^2$ is positive.

Thus we obtain the lower bound on the controller's stiffness parameters:

$$\sigma_i > \|\tilde{K}_{ii}\| + \frac{1}{\sigma_0} \|\tilde{K}_{0i}\|^2 \quad \text{for } i = 1, \dots, k. \quad (4.28)$$

³The matrix norm is defined as $\|E\| = \max\{\|Eu\|\}$ over all vectors $\|u\| \leq 1$.

Any value of the σ_i 's above these lower bounds guarantees that the matrix $(\tilde{K})_s$ is positive definite, and consequently that $M^{-1/2}(\tilde{K})_s M^{-1/2}$ is positive definite.

To satisfy the **third condition** we need $\omega = \|M^{-1/2}(\tilde{K})_{as} M^{-1/2}\| < \sqrt{\alpha}\beta$. Specifically we have

$$(\tilde{K})_{as} = \sum_{i=1}^m J_i^T R_i^T (K_i)_{as} R_i J_i,$$

and recall that

$$K_i = \begin{bmatrix} \frac{4G\sqrt{R\delta_i^n}}{1-\nu} & 0 \\ \frac{8GR\delta_i^t}{3\sqrt{R\delta_i^n}(2-\nu)} & \frac{16G\sqrt{R\delta_i^n}}{3(2-\nu)} \end{bmatrix}.$$

Substituting Walton loading path $c_i = \frac{\delta_i^t}{\delta_i^n}$ yields

$$K_i = G\sqrt{R\delta_i^n} \begin{bmatrix} \frac{4}{1-\nu} & 0 \\ \frac{8c_i}{3(2-\nu)} & \frac{16}{3(2-\nu)} \end{bmatrix}.$$

Which it's skew-symmetric part is

$$(K_i)_{as} = G\sqrt{R\delta_i^n} \begin{bmatrix} 0 & -\frac{8c_i}{3(2-\nu)} \\ \frac{8c_i}{3(2-\nu)} & 0 \end{bmatrix}.$$

Note that the maximum eigenvalue of $(K_i)_{as}$ depends on the value of $|c_i|$. Small $|c_i|$ correspond to penetrations which are more in the normal direction and consequently forces that are more normal than tangential. Moreover, small $|c_i|$ introduces small asymmetric part of K_i and help satisfy the third condition of the theorem. Thus the third condition introduce an upper bound to the sum of the $|c_i|$ s. However this is not the only condition on the $|c_i|$ s. From proposition 4.2.1 we have the following condition for $(K_i)_s$ to be positive definite:

$$|c_i| < \sqrt{\frac{12(2-\nu)}{(1-\nu)}}.$$

From (4.14) we have an upper bound on $|c_i|$ which guarantees that the contact force is within its friction cone as follows:

$$c_i^f = \frac{F_i^t}{F_i^n} = c_i \frac{2(1-\nu)}{(2-\nu)} < \mu$$

Finally, the third upper bound on $|c_i|$ is from the third condition of theorem 8

$$\|M^{-1/2}(\tilde{K})_{as}M^{-1/2}\| < \sqrt{\alpha}\beta$$

as discussed before. The selection of $|c_i|$'s value is such that it satisfies all these three upper bounds. This together with the selection of stable holding posture for the mechanism as single rigid body, and together with high enough proportional gain in the joint's controllers, are sufficient conditions for the equilibrium of the mechanism to be *locally asymptotically stable*.

4.5 Conclusion

We described a control method for spider-like robots that move quasi-statically in *frictional* tunnel environments. That completes previous results on the control of spider-like robots that move quasi-statically in *frictionless* tunnel environments [64, 65, 69]. To induce forces and torques on the spider's unactuated central-base, we used grasp theory, that determines the conditions under which the mechanism is stably grasped by the tunnel as single rigid-body. When compliance at the contacts is taken into account, stable grasp yields passive stabilization of the mechanism as a single rigid body. In addition compliant frictional contact model introduce asymmetric stiffness matrix. New results presented here show that if the symmetric part of the system is asymptotically stable and if the asymmetric part is "small" enough comparing to the symmetric part then the asymmetric system will be asymptotically stable. Using

these two results we presented a PD control law for general k -limbed spider robots. We presented an approximation for the equilibrium point of the mechanism as function of the PD target point q^* . In other words specific selection of q^* determines the equilibrium penetrations $\hat{\delta} = (\hat{\delta}_1^n, \hat{\delta}_1^t, \dots, \hat{\delta}_k^n, \hat{\delta}_k^t)$. Then we introduced three inequalities in $\hat{\delta}, P$, and $|c_i| = |\delta_i^t/\delta_i^n|$. We showed that P should be selected stiff enough, and $|c_i|$ should be selected small enough. The bounds for P and $|c_i|$ has been computed analytically. Moreover, we showed that the amount of normal penetration δ_i^n does not change the stability property of the system, but it does affects the convergence path. Note that this result is consistent with previous results on spider robot control in frictionless environments. Here as there we showed the existence of a lower bound on the controller proportional gain, and in both cases we need the mechanism to be stably grasped by the tunnel as a single rigid body.

Chapter 5

Experimental Results

In this chapter we describe the experimental setup and summarize the results of the spider robot motion in a tunnel built in our laboratory. The experiments were conducted using our 12 DOF spider-robot. The main goal of these experiments is to verify the PCG, the control algorithms, and the related simulation results.

5.1 Experiments Setup

Kinematic analysis of the robot motion shows that three links and three joints for each limb are required [59]. However, when operating in a congested environment, additional degree of freedom is required in order to increase maneuverability while retaining a manageable mechanism complexity. The spider robot therefore consists of four links and four joints for each limb.

Two key dimensions of the robot affect the PCG algorithm: the central body and the total limbs' length. The central body is a thick block that contains three driving motors and some electronics. The robot radius denoted as R is the length

of a fully stretched limb measured from the center of the base to the limb's footpad. The choice of R affects the ability of the robot to reach desired footholds along the tunnel walls. Based on the tunnel dimension the robot radius chose to be 77.2cm with a base dimension of 14cm (from the center of the base to the limb's first joint).

To minimize inter-link interference, the robot limbs work in two distinct planes, upper plane and lower plane. The upper plane limbs never interfere with the lower plane limbs (except for a possible interference of the passive supports, discussed below). The resulting design allows simultaneous motion of the three limbs with minimal inter-link interference. The robot moves in a horizontal two dimensional tunnel. However, vertical gravitational forces may generate a torque that can tip the robot out of the horizontal plane. To prevent tilting during locomotion, the central body and each limb are equipped with a supporting mechanism consists of a planar air bearing. While preventing possible tilt, the planar bearings generate only small undesired friction forces between the robot and the horizontal plan on which is operates.

Each limb is actuated by 4 different motors proportional to the required torque. The first joint (closest to the central body) is equipped with the biggest motor and the footpad joint is equipped with the smallest motor. Optical encoders are attached to each joint, providing accurate angle measurements regardless of any backlash. Motion is controlled using MEI controllers that enable synchronized motion of all limbs. Figure 3.1 shows the spider-robot.

The experimental setup includes the spider robot, a planar tunnel with piecewise linear walls constructed of 5 linear segments. The configuration of the walls is such that it provides various geometric features for different types of motion such as parallel walls, diverging walls and converging walls. The walls are made of transparent stiff plastic (Plexiglas) coated with medium rough sand paper. A lower bound on the

friction coefficient between the robot's footpads and the walls is 0.5. As mentioned in the previous section, the robot is travelling on a horizontal plan using air bearing supports, reducing the friction between the robot and that plan to low values. All walls are perpendicular to the plan and can produce large enough reaction forces required for the robot motion.

5.2 Experimental Results

The PCG algorithm is applied off-line before motion starts and trajectories for all 12 actuators are being constructed and stored in the controller. The output of the PCG algorithm is a series of foothold positions. These foothold positions are marked and numbered on the tunnel walls in Figure 5.1. The series of robot's steps along the tunnel is presented in Figure 5.2 as a path in the contact c-space. Before starting the experiments the tunnel walls were marked according to the desired foothold positions.

The experiment starts with the calibration process outside the tunnel, followed by controlled motion in which the robot positions itself at the starting point. When motion starts, all actuators are synchronized frame-by-frame while actual position of each joint is continuously recorded. This data is then used for motion analysis.

Although cameras are being used during the experiments, the visual data is *not* incorporated into the motion control. Not using feedback on the central base position and orientation requires a close match between the planned trajectory and the actual motion. In that case the system is open-loop with respect to the central base configuration, and deviation from the desired trajectory may result in contact loss between one or more of the footpads and the walls. However, the system is locally robust to errors in the central base configuration. This robustness is due to the fact that footpads

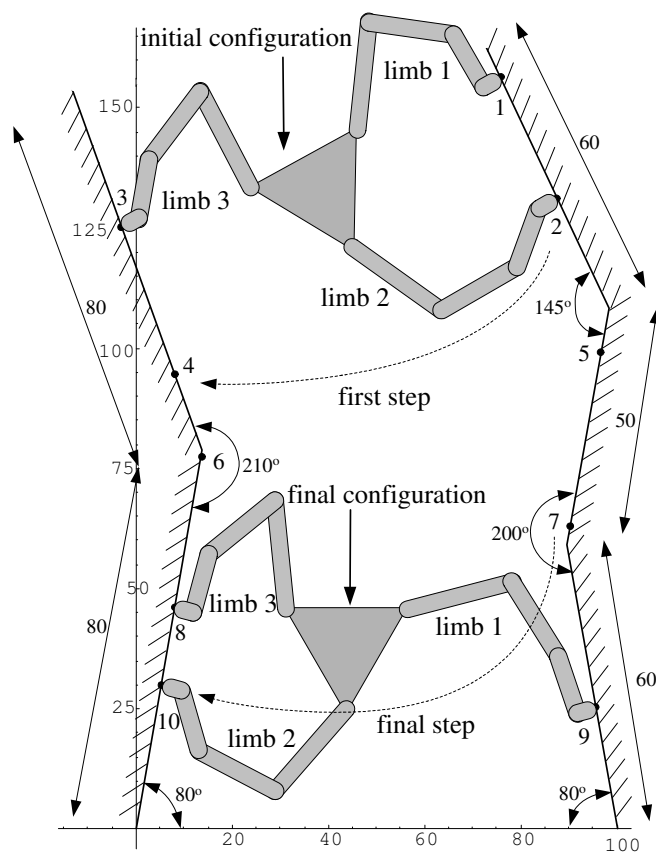


Figure 5.1: The tunnel environment used for the experiment, and the sequence of foothold positions generated by the PCG algorithm numbered from 1 to 10.
 המנהרה ששימשה לניסוי, וסידרת נקודות האחיזה אשר יוצה ע"י אלגוריתם PCG.

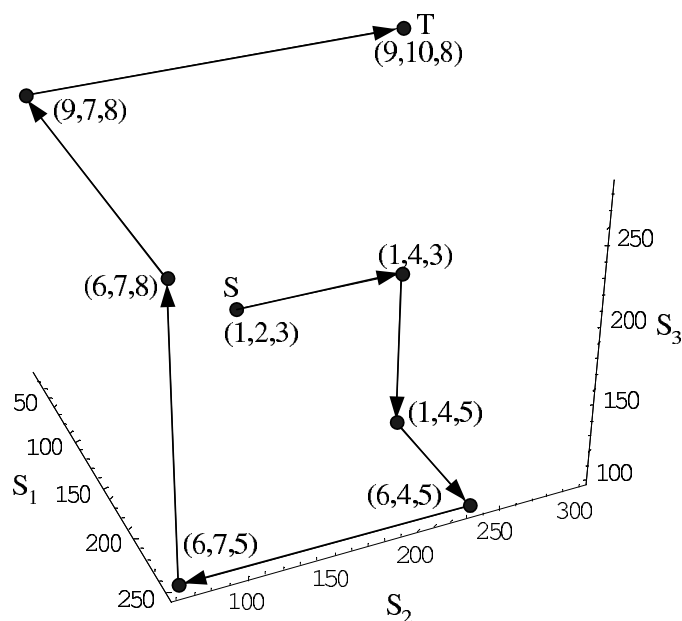


Figure 5.2: The shortest path from S to T along the edges of the sub-cube graph in contact c-space. In every node (step) along the path it is marked the foothold point on the tunnel of (limb 1, limb 2, limb 3).

המסלול הקצר ביותר מ- S ל- T לאורך קשתות גרף תת-התיבות במרחב קונפיגורציות המגע. בכל צומת (צעד) מסומנות נקודות האחיזה בצורה (רגל 1, רגל 2, רגל 3).

are aimed to points *inside* the tunnel walls to apply positive contact forces. Foothold location is locally robust because the nominal contact point is the center of contact independent cube. Without visual or other absolute feedback mechanism the robot cannot converge to the nominal trajectory, similar to odometric errors of wheeled vehicles that increase unboundedly. But if the robot do not diverge far enough from the nominal trajectory then motion can still be conducted due to the local robustness property.

To bound the contact forces between the robot and tunnel walls, and to reduce electromagnetic interferences, current of all actuators is limited to 3A. Speed and acceleration of all actuators is also limited to $4.5 \frac{deg}{sec}$ and $4.5 \frac{deg}{sec^2}$ respectively. This is required in order to prevent large inertial forces that may interrupt our motion. Low speed and low acceleration motion is more accurate. This accuracy is needed to prevent the central-base of the robot from diverging far from the predesigned trajectory. Moreover, high accelerations of the center of mass of the robot demands large contact forces. For example if we wish to accelerate the robot's center of mass by $0.01 \frac{m}{sec^2}$ we need a net forward force of $24 * 0.01 = 0.24 N$, where the robot mass is $24 Kg$. Consider the case where the robot hold itself between two parallel walls (Figure 5.3) such that the line connecting the two foothold positions form a 25° angle with the horizontal line. The coefficient of friction is 0.5 and $\alpha = Arctan(0.5) = 26.565^\circ$. A given contact forces f_1 and f_2 are initially antipodal to form an equilibrium grasp. The force can rotate not more than 1.565° without braking the friction cone constraint. By rotating both contact forces by that angle we produce $2f_i \sin(1.565^\circ)$ net forward force. So, to produce $0.24 N$ net forward force we need initial contact force of $4.4 N$. And if we wish to increase the acceleration to $0.05 \frac{m}{sec^2}$ we need initial contact force of at least $22 N$ which is relatively high. Note that this computation does not

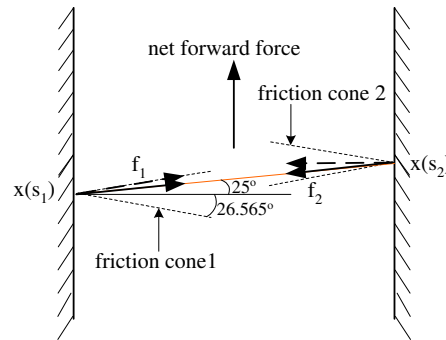


Figure 5.3: Illustration that shows how net forward force is produced by the contact forces.

תרשים המראה כיצד נוצר כוח קדימה ע"י כוחות המגע.

take into account the friction forces in the planar bearing that demands additional forward force.

In our experiments no force or torque feedback is being used, and motion is controlled entirely by decentralized PD controllers with feedback on the joints angles.

Figure 5.4 shows a full motion of the robot from one end of the tunnel to the other end. This figure presents the entire robot configuration history during motion from S to T . In the first row of graphs in the figure the x, y and θ coordinates of the central-base are presented, in every other row the joints angles of every limb is presented. The leftmost graph shows the angle of the inner joint while the rightmost graph shows the angle of the distal joint. Total trajectory length measured as the y coordinate of the central base is $1.5m$ and total motion time is 33 minutes. This low speed results from the overall current limit which reduced the voltage to the DC motors. However, the low speed enabled very accurate motion along the pre-designed path without any feedback on the central base position and orientation. This accuracy of the motion can be seen in the motion graphs as very small deviations between the desired and the actual paths. A considerable large deviation from the predesigned

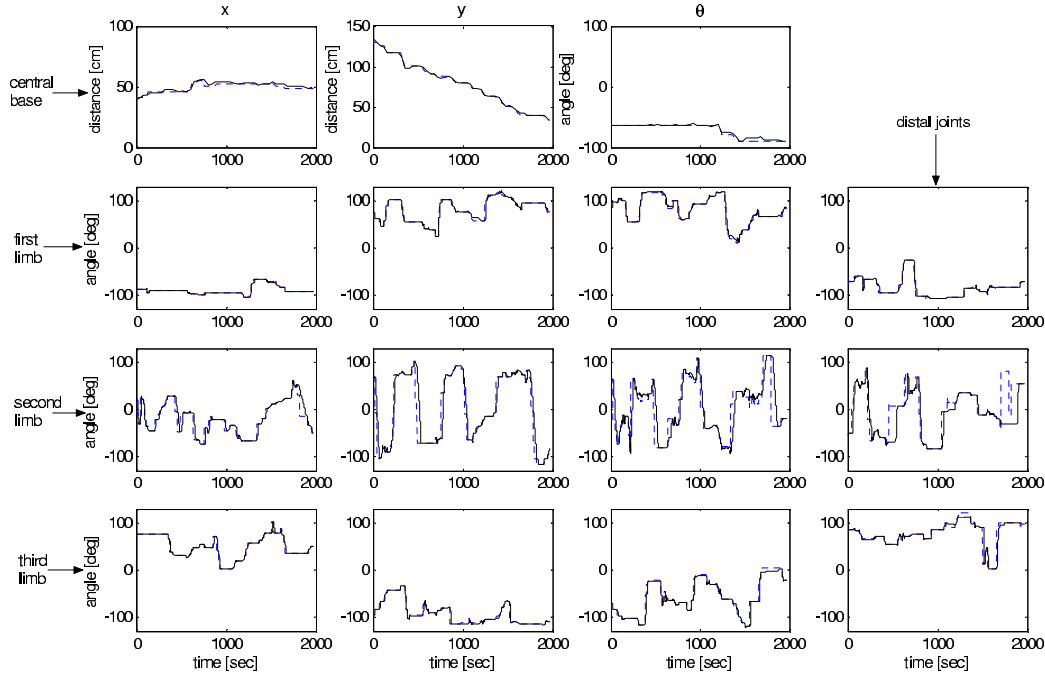


Figure 5.4: Measurements of the spider configuration parameters during the experiment. The desired path for every joint is indicated by dashed lines and the solid lines are the actual measurements.

מדידות של פרמטרי הקונפיגורציה של הרובוט במהלך הניסוי. המסלול הרצוי מסומן ע"י קו מקווקו והמדידות בפועל מתוארות ע"י קו רציף.

path happened during the few last minutes of motion in the distal link of the second limb. This can be explained as follows, the distal joint did not succeeded to reach it's desired angle before contacting the tunnel's wall. After contacting the tunnel and applying force on the tunnel the distal motor, which is the smallest motor, did not have enough torque to reach it's desired angle. This angle was corrected only when the limb brake contact with the wall and move the the next foothold position. Last, Figure 5.5 presents snapshots from the video of the robot motion. The full video is also available to download from our website at <http://www.technion.ac.il/~robots/>.

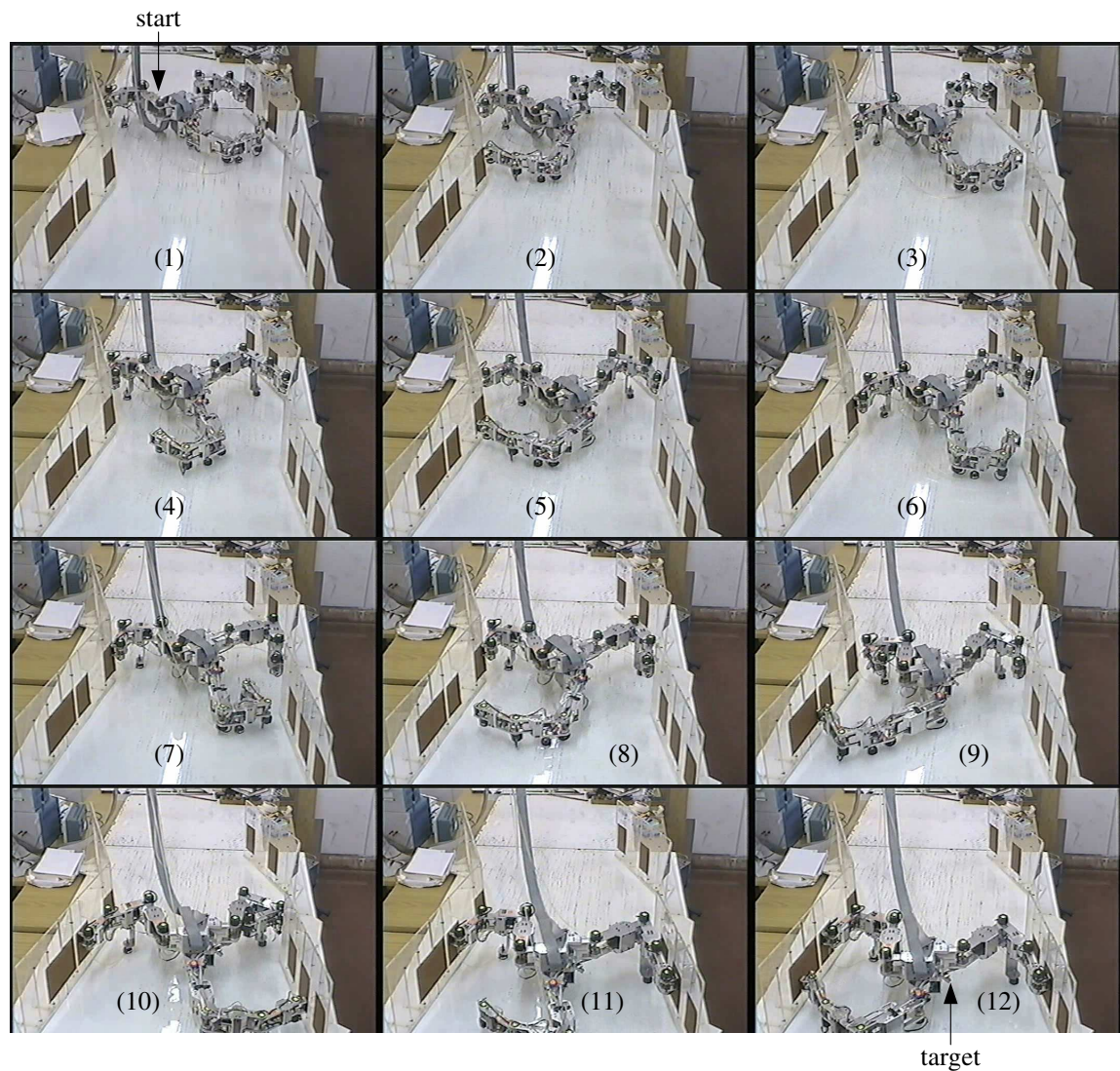


Figure 5.5: Snapshots from the video showing the spider robot motion in the tunnel.
תמונות מסרט הוידאו המראה את רובוט-העכביש נע לאורך המנהרה.

Chapter 6

Conclusion

This work deals with the navigation and control of a planar spider robot in $2D$ -tunnel environments. The spider-robot moves quasi-statically by bracing with two limbs against the environment while moving its free limb to a new foothold position. Note that during this motion the spider is free to change its internal configuration as long as the holding footpads will not change their relative configuration. In this case under the conditions of theorem 8 local asymptotic stability of the spider is guaranteed. A necessary condition for the stability of the mechanism is that tunnel stably grasp the spider as a single rigid body. Therefore in chapter 2 we investigate the case of rigid body grasped by compliant fingers. In this case we analyzed the condition for asymptotic stability of the rigid body; we found the basin of attraction of the object's equilibrium; and we characterized the set of external wrenches that can be applied on the object without destruct its stability. These results has been verified experimentally.

In chapter 3 we presented an algorithm, named PCG, to select the sequence of foothold positions along the tunnel. The PCG algorithm approximates the collection

of feasible 3-limb postures by maximal cubes. The algorithm next partitions the cubes into sub-cubes and defines a graph whose nodes are sub-cubes and whose edges represent feasible motion of a limb between any 3-limb postures. A shortest path search on the resulting graph generates a 3-2-3 gait sequence that moves the robot from start to target using minimum number of foothold exchanges.

In chapter 4 we introduced a decentralized PD controller for the robot. we developed the robot's dynamic equations. In order to express the contact forces in these equation a compliant contact model has been used. From the contact forces model we derived the contact stiffness matrix. We showed that this matrix is asymmetric. Since the overall linearized system is asymmetric a general new result on the stability of asymmetric second order linear systems has been developed. This result is based on the idea of considering a stable symmetric system and then adding the asymmetric part. If the asymmetric part is small enough it will not destruct the stability of the system. This result was implemented on the spider-robot system to give the stability conditions. It was shown the following three conditions for the asymptotic stability of the mechanism. First, the entire mechanism should be stably grasped as a single rigid body by the tunnel. Second, the proportional gain of the controller must be above a certain lower bound. Third, each contact force should be inside it's friction cone and close enough to the normal direction.

Experimental results demonstrate motion of the spider along the tunnel, while selecting it's foothold positions by the PCG algorithm. The controller's gain was tuned high enough to meet the requirements of theorem 8. The significance of these experiments is to first verify the theoretical results developed here, and second to show that these results are applicable to a real walking machine.

Future extensions of this research may take the following directions. First,

current work (by E. Rimon and Y. OR) is concerned with the inclusion of gravity. Especially we would like to rotate the horizontal table supporting the robot and take off the upper part of the tunnel. This will give us a two dimensional walker over one dimensional terrain.

Second, an on-line navigation algorithm may be developed to overcome errors during the motion. This algorithm has to use localization system such as a visual system mounted on top of the tunnel or a laser scanner mounted on the central base of the robot.

Third, an additional work may be done in handling the case of reconstructing stable holding posture after loosing necessary contact with the tunnel. As for now if a necessary contact is lost the spider is hanging in the tunnel unable to continue walking. This work can be combined with an on-line navigation algorithm.

Fifth, In the future we may want to extend this work to a three-dimensional spider robot moving in three dimensional tunnels. It seems that most of our theoretic work can be straight forward implement on *3D*-spiders.

Sixth, one may want to develop spider-robot in various size scales. Sizes of spider-robots may be from few millimeters for motion within blood vessels in a human body to few meters for motion in large tunnels or piping systems.

Seventh, a major extension of this work or even a new research should be in the field of dynamic walk. In this field the robots exploit the inertial forces caused by it's own motion to help him conduct the full desired motion.

Appendix A

Additions for Force Closure Grasps

A.1 Conditions for Force Closure with Compliant Contacts

Proof sketch of Proposition 2.2.1: Let \mathcal{N} be a small neighborhood of configurations about q_0 . As \mathcal{B} 's configuration varies in \mathcal{N} , the contact forces vary in a neighborhood about the contact forces of the initial grasp. Since the initial grasp is non-marginal, by a continuity argument all contact forces generated by varying \mathcal{B} 's configuration in \mathcal{N} still lie in their respective friction cones. (This statement holds true even when the location of some contact points changes due to local rolling of \mathcal{B} .)

Next we establish that any external wrench in a neighborhood about the origin can be balanced by feasible contact forces. When \mathcal{B} is at a configuration $q \in \mathcal{N}$, the net wrench generated by the contacts is given by the negated gradient $-\nabla U(q)$. Consider now the gradient $\nabla U(q)$ as a mapping from configuration space to wrench space. By assumption $\nabla U(q_0) = 0$. According to the Inverse Function Theorem, ∇U maps an open neighborhood about q_0 to an open neighborhood about the zero wrench

if the derivative of ∇U at q_0 , $D^2U(q_0)$, is non-singular. Since q_0 is a non-degenerate local minimum of U , $D^2U(q_0)$ is non-singular as required.

Finally we establish that \mathcal{B} would automatically settle at a configuration where the contact forces balance the external wrench acting on \mathcal{B} . Let \mathbf{w}_{ext} denote a fixed external wrench acting on \mathcal{B} . The dynamics of \mathcal{B} is governed by the equation: $M(q)\ddot{q} + B(q, \dot{q}) = -\nabla U(q) + \mathbf{w}_{ext}$. (The contacts also apply damping forces which we ignore for simplicity.) The external influences on \mathcal{B} can be written as the negated gradient of a composite potential function: $\Phi(q) = U(q) - \mathbf{w}_{ext} \cdot q$. A general result concerning the dynamics of mechanical systems states that the flow of a damped mechanical system governed by a potential function Φ is attracted to the local minima of Φ [34]. We have already shown that for every \mathbf{w}_{ext} in a neighborhood about the origin there exists a configuration q_1 such that $\nabla\Phi(q_1) = 0$. The equilibrium point q_1 is a stable attractor if it is a local minimum of Φ i.e., if $D^2\Phi(q_1) > 0$. But $D^2\Phi(q) = D^2U(q)$, and the entries of $D^2U(q)$ vary continuously with q . Since the eigenvalues of a matrix vary continuously with its entries, $D^2U(q)$ remains positive definite in a neighborhood of q_0 . By shrinking \mathcal{N} if necessary, we conclude that q_1 is a local minimum of Φ , and \mathcal{B} would automatically settle at q_1 . □

A.2 Computation of the Grasp Stiffness Matrix

In this appendix we compute the two formulas for $D^2U(q)$ which appear in Lemma 2.3.1. To begin with, $U(q) = \sum_{i=1}^k U_i(q)$ where $U_i(q)$ is the elastic energy induced by the i^{th} active-compliance contact. Using the linear compliance law (2.4), the elastic

energy induced by the i^{th} contact is:

$$U_i(q) = \frac{1}{2}(X_i(r_i^0, q) - x_i^0)^T K_i(X_i(r_i^0, q) - x_i^0) - F_i^0 \cdot (X_i(r_i^0, q) - x_i^0),$$

where $x_i = X_i(r_i^0, q) = R(\theta)r_i^0 + d$. The first derivative of U_i is: $DU_i(q) = -DX_{r_i}(q)^T F_i(q)$, where $F_i(q) = F_i^0 - K_i(x_i(q) - x_i^0)$. The second derivative of U_i is:

$$D^2U_i(q) = DX_{r_i}^T(q)K_iDX_{r_i}(q) - D^2X_{r_i}(q)^T F_i(q). \quad (\text{A.1})$$

Recall that $[u \times]$ is the 3×3 skew-symmetric matrix satisfying $[u \times]v = u \times v$ for all $v \in \mathbb{R}^3$. Then $DX_{r_i}(q) = [I, (-\boldsymbol{\rho}_i) \times]$. The second derivative, $D^2X_{r_i}(q)$, is a vector-valued symmetric bilinear function. To obtain a formula for $D^2X_{r_i}(q)$, we compute the derivative of $DX_{r_i}(q)$ along a configuration-space trajectory $q(t)$. The velocity of \mathcal{B} along $q(t)$ is denoted $\dot{q} = (v, \omega)$, where v and ω are \mathcal{B} 's linear and angular velocities. Since $\boldsymbol{\rho}_i = R(\theta)r_i^0$, $\frac{d}{dt}DX_{r_i}(q(t)) = [0, (-\dot{R}r_i^0) \times] = [0, (\boldsymbol{\rho}_i \times \omega) \times]$. The action of this derivative on the force F_i is: $(\frac{d}{dt}DX_{r_i}(q(t)))^T F_i = \begin{pmatrix} 0 \\ (\boldsymbol{\rho}_i \times \omega) \times F_i \end{pmatrix}$. Using a triple cross-product identity, we obtain that $(\boldsymbol{\rho}_i \times \omega) \times F_i = [(\boldsymbol{\rho}_i \cdot F_i)I - \boldsymbol{\rho}_i F_i^T] \omega = -[F_i \times][\boldsymbol{\rho}_i \times] \omega$. On the other hand, the chain rule implies that $\frac{d}{dt}DX_{r_i}(q(t)) = (D^2X_{r_i}(q))\dot{q}$. Hence the action of $D^2X_{r_i}(q)$ on F_i is given by the following matrix:

$$D^2X_{r_i}(q)^T F_i = \begin{bmatrix} 0 & 0 \\ 0 & -([F_i \times][\boldsymbol{\rho}_i \times])_s \end{bmatrix}.$$

Substituting for $DX_{r_i}(q)$ and $D^2X_{r_i}(q)^T F_i$ in (A.1) and summation $D^2U(q) = \sum_{i=1}^k D^2U_i(q)$ gives formula (2.5) for 3D grasps. In the 2D case, we evaluate each $D^2U_i(q)$ along a velocity vector $\dot{q} = (v, \omega)$ such that $v = (v_x, v_y, 0)$ and $\omega = (0, 0, \omega_z)$. In particular, $[\boldsymbol{\rho}_i \times] \omega = \omega_z J \boldsymbol{\rho}_i$ where $J = \begin{bmatrix} 0 & 1 \\ -1 & 0 \end{bmatrix}$, and $[F_i \times][\boldsymbol{\rho}_i \times] \omega = (\boldsymbol{\rho}_i \cdot F_i) \omega_z$. When these

terms are substituted into $D^2U_i(q)$ and the sum $D^2U(q) = \sum_{i=1}^k D^2U_i(q)$ is taken, formula (2.6) is obtained.

Appendix B

Details of the PCG Algorithm

This appendix contains two details of the PCG algorithm. First we describe the necessary modification to the algorithm when a cell contains two or three possibly overlapping convex sets of feasible 3-limb postures. Since each convex set is approximated individually by p maximal cubes, it is possible that two maximal cubes originating from different convex sets would overlap. However, each cube still has its own unique orientation vector. The partitioning of the maximal cubes into sub-cubes proceeds as before. The edges between sub-cubes are assigned a weight of unity or zero according to the following two cases. If the two sub-cubes connected by the edge are disjoint, the edge is assigned a *unit* weight as before. In the second case the edge connects two copies of the same sub-cube. We represent the two sub-cubes as distinct nodes, and assign *zero* weight to the edge connecting the two sub-cubes. Note that zero-weight edges provide important pathways in the sub-cube graph. Rather than representing a physical limb lifting and re-placement, these edges represent a freedom of the algorithm to select among more than one limb for its next step.

The following lemma asserts that motion of a limb between two reachable 3-limb

postures along an edge satisfies the reachability constraint.

Lemma B.0.1 *Consider two reachable 3-limb postures. If two limbs and their footpad positions are common to both postures, there exists a path that takes the third limb between the two postures such that the three footpads are continuously reachable along the path.*

The lemma generalizes as follows. If two k -limb postures share at least two limbs and their contacts, there exist a path for the remaining $k-2$ limbs between the two postures such that all k footpads are continuously reachable along the path.

Proof: The minimum-radius discs containing the two triplets of foothold positions necessarily overlap, since two foothold positions are common to both postures. The radius of the two discs is bounded by R , since the two triplets of foothold positions are reachable. It follows that any motion of the third limb between its two footholds such that its footpad lies in the union of the two discs guarantees that the three footpads, one moving and two stationary, are continuously reachable along the path.

□

References

- [1] S. Adhikari. On symmetrizable systems of second kind. *Journal of Applied Mechanics*, 67:797–802, December 2000.
- [2] A. Bicchi. On the problem of decomposing grasp and manipulation forces in multiple whole-limb manipulation. *Int. J. of Robotics and Autonomous Systems*, 13(4):127–147, 1994.
- [3] A. Bicchi. On the closure properties of robotic grasping. *The International Journal of Robotics Research*, 14(4):319–334, Aug. 1995.
- [4] A. Bicchi. Hands for dexterous manipulation and robust grasping: A difficult road toward simplicity. *IEEE Trans. on Robotics and Automation*, 16(6):652–662, Aug. 2000.
- [5] J.-D. Boissonnat, O. Devillers, L. Donati, and F. P. Preparata. Motion planning for spider robots. In *IEEE Int. Conf. on Robotics and Automation*, pages 2321–2326, 1992.
- [6] J.-D. Boissonnat, O. Devillers, and S. Lazard. Motion planning of legged robots. *SIAM J. of Computing*, 30:218–246, 2000.

-
- [7] S. P. Boyd and C. H. Barratt. *Linear Controller Design*. Prentice Hall, NJ, 1991.
- [8] N. Brook, M. Shoham, and J. Dayan. Grasping and walking finger manipulation of objects using a four-fingered hand. *Annals of the CIRP*, 42.
- [9] G.S. Chirikjian and J.W. Burdick. Design and experiments with a 30 degree-of-freedom hyper-redundant robot. In *IEEE Int. Conf. on Robotics and Automation*, pages 3:113–117, 1993.
- [10] W. Cho, D. Tesar, and R. A. Freeman. The dynamics and stiffness modeling of general robotic manipulator systems with antagonistic actuation. In *IEEE Int. Conf. on Robotics and Automation*, pages 1380–1387, 1989.
- [11] N. G. Chtayev. *The Stability of Motion*. Pergamon Press, London, 1961.
- [12] F. H. Clarke. *Optimization and Nonsmooth Analysis*. SIAM Publication, 1990.
- [13] M. R. Cutkosky and I. Kao. Computing and controlling the compliance of a robotic hand. *IEEE Transactions on Robotics and Automation*, 5(2):151–165, April 1989.
- [14] S. Dubowsky, C. Sunada, and C. Marvoidis. Coordinated motion and force control of multi-limbed robotic systems. *Autonomous Robots*, 6:7–20, 1999.
- [15] H. Elci, R. W. Longman, and M. Shoham. Planar three-finger manipulation of objects with a dextrous robot hand. *American Institute of Aeronautics and Astronautics*, pages 1061–1071, 1990.

-
- [16] W. M. Faucette. A geometric interpretation of the solution of the general quartic polynomial. *The American Mathematical Monthly*, 103(1):51–57, January 1996.
- [17] D.G. Flom. Dynamic mechanical losses in rolling contacts. In J.B. Bidwell, editor, *Rolling Contact Phenomena*, pages 97–112. Elsevier, 1962.
- [18] B. Goodwine and J. W. Burdick. A general method for motion planning for quasi-static legged robotic locomotion and finger gaiting. *IEEE Transactions on Robotics and Automation (to appear)*.
- [19] E. Guy. Navigation algorithm for plan spider robot in smooth intermittent–linear tunnel. Master’s thesis, Technion - Israel Institute of Technology, Haifa Israel, March 2003.
- [20] H. Hanafusa and H. Asada. Stable prehension by a robot hand with elastic fingers. In *Proc. 7th Int. Symp. Industrial Robots*, pages 384–389, 1977.
- [21] H. Hertz. On the contact of elastic solids. In *Miscellaneous Papers by H. Hertz (1882)*. Macmillan, London, 1896.
- [22] S. Hirose and O. Kunieda. Generalized standard foot trajectory for a quadruped walking vehicle. *The Int. J. of Robotics Research*, 10(1):2–13, 1991.
- [23] S. Hirose and A. Morishima. Design and control of a mobile robot with an articulated body. *The Int. J. of Robotics Research*, 9(2):99–114, 1990.
- [24] N. Hogan. Impedance control: An approach to manipulation—part i, part ii, part iii. *ASME J. Dynamic Syst., Measure., Control*, 107:1–24, 1985.

- [25] J. Hong, G. Lafferriere, B. Mishra, and X. Tan. Fine manipulation with multifinger hands. In *IEEE Int. Conf. on Robotics and Automation*, pages 1568–1573, 1990.
- [26] R. A. Horn and C. R. Johnson. *Matrix Analysis*. Cambridge University Press, Orlando, Fla., 1985.
- [27] W. S. Howard and V. Kumar. On the stability of grasped objects. *IEEE Transactions on Robotics and Automation*, 12(6):904–917, Dec. 1996.
- [28] K. Huseyin. *Vibrations and Stability of Multiple Parameter Systems*. Noordholl International Publishers, The Netherlands, 1978.
- [29] D. J. Inman. *Vibration with Control Measurement and Stability*. Prentice-Hall, Inc, Englewood Cliffs, NJ., 1989.
- [30] F. Jen, M. Shoham, and R.W. Longman. Lyapunov stability of force-controlled grasps with a multi-fingered hand. *The International Journal of Robotics Research*, 15(2):137–154, April 1996.
- [31] K. L. Johnson. *Contact Mechanics*. Cambridge University Press, 1985.
- [32] J. R. Kerr and B. Roth. Analysis of multi-fingered hands. *The International Journal of Robotics Research*, 4(4), Winter 1986.
- [33] D. E. Koditschek. Strict global lyapunov function for mechanical system. In *American Control Conference*, pages 1770–1775, Atlanta, Georgia, June 1988.
- [34] D. E. Koditschek. The application of total energy as a lyapunov function for mechanical control systems. In *J. Marsden, Krishnaprasad, and*

- J. Simo, editors, Control Theory and Multibody Systems, AMS Series in Contemporary Mathematics, 97:131–158, 1989.*
- [35] P. R. Kraus and V. J. Kumar. Compliant contact models for rigid body collisions. In *IEEE Int. Conf. on Robotics and Automation*, pages 1382–1387, Albuquerque, New Mexico, April 1997.
- [36] P. R. Kraus, V. J. Kumar, and P. Dupont. Analysis of frictional contact models for dynamic simulation. In *IEEE Int. Conf. on Robotics and Automation*, pages 976–981, Leuven, Belgium, May 1997.
- [37] J. K. Lee and S. M. Song. Path planning and gait of walking machine in an obstacle-strewn environment. *J. Robotics Systems*, 8:801–827, 1991.
- [38] S. Leveroni and K. Salisbury. Reorienting objects with a robot hand using grasp gaits. In *7th International Symposium on Robotics Research*, pages 2–15, 1995.
- [39] Q. Lin, J. W. Burdick, and E. Rimon. Computation and analysis of compliance in grasping and fixturing. In *IEEE Int. Conf. on Robotics and Automation*, pages 93–99, 1997.
- [40] A. Madhani and S. Dubowsky. Motion planning of mobile multi-limb robotic systems subject to force and friction constraints. In *IEEE Int. Conf. on Robotics and Automation*, pages 233–239, 1992.
- [41] D. W. Marhefka and D. E. Orin. Gait planning for energy efficiency in walking machines. In *IEEE Int. Conf. on Robotics and Automation*, pages 474–480, 1997.

- [42] X. Markenscoff, L. Ni, and C. H. Papadimitriou. The geometry of grasping. *The Int. Journal of Robotics Research*, 9(1):61–74, 1990.
- [43] T. McGeer. Powered flights, child’s play, silly wheels and walking machines. In *IEEE Int. Conf. on Robotics and Automation*, pages 1592–1597, 1989.
- [44] J. Milnor. *Morse Theory*. Princeton University Press, Princeton, NJ, 1963.
- [45] R. D. Mindlin. Compliance of elastic bodies in contact. *ASME Journal of Applied Mechanics*, 16:259–268, 1949.
- [46] B. Mishra. Workholding. In *IEEE/RSJ International Conference on Intelligent Robots and Systems*, pages 53–57, 1991.
- [47] D. J. Montana. Contact stability for two-fingered grasps. *IEEE Transactions on Robotics and Automation*, 8(4):421–230, 1992.
- [48] J. J. Moré and T. S. Munson. Computing mountain passes. Technical Report ANL/MCS-P957-0502, Mathematics and Computer Science Division, Argonne National Laboratory, <http://www-unix.mcs.anl.gov/~more/papers/>, May 2002.
- [49] R. M. Murray, Z. Li, and S. S. Sastry. *A Mathematical Introduction to Robotic Manipulation*. CRC Press, Boca Raton, FA, 1994.
- [50] Y. E. Nesterov and A. S. Nemirovsky. *Interior Point Polynomial Methods in Convex Programming: Theory and Applications*. Springer Verlag, New York, 1992.

- [51] W. Neubauer. Spider-like robot that climbs vertically in ducts or pipes. In *IEEE/RSJ/GI International Conference on Intelligent Robots and Systems*, pages 2:1178–1185, 1994.
- [52] V.-D. Nguyen. Constructing force-closure grasps. *The Int. Journal of Robotics Research*, 7(3):3–16, 1988.
- [53] V.-D. Nguyen. Constructing stable grasps. *The Int. Journal of Robotics Research*, 8(1):27–37, 1988.
- [54] L. Nirenberg. Variational and topological methods in nonlinear problems. *Bulletin of the AMS*, 4(3):267–302, May 1981.
- [55] F. Pfeiffer, T. Rossmann, N. Bolotnik, F. Chernousko, and G. Kostin. Simulation and optimization of regular motions of a tube-crawling robot. *Multibody System Dynamics*, 5:159–184, 2001.
- [56] J. Ponce and B. Faverjon. On computing three-finger force closure grasps of polygonal objects. *IEEE Trans. on Robotics and Automation*, 11(6):868–881, 1995.
- [57] J. Ponce, D. Stam, and B. Faverjon. On computing two-finger force closure grasps of curved 2D objects. *The International Journal of Robotics Research*, 12(3):263–273, 1993.
- [58] E. Rimon, S. Shoval, and A. Shapiro. Design of a spider-like robot for motion with quasistatic force constraints. In *IEEE Int. Conference on Robotics and Automation*, Detroit, MI, May 1999.

- [59] E. Rimon, S. Shoval, and A. Shapiro. Design of a quadraped robot for motion with quasistatic force constraints. *Autonomous Robots*, 10:279–296, May 2001.
- [60] T. Roassmann and F. Pfeiffer. Control and design of a pipe crawling robot. In *13th World Congress of Automatic Control*, San Francisco, USA, 1996.
- [61] J. K. Salisbury. *Kinematic and Force Analysis of Articulated Hands*. PhD thesis, Dept. of ME, Stanford University, 1982.
- [62] J. Savall, A. Avello, and L. Briones. Two compact robots for remote inspection of hazardous areas in nuclear power plants. In *Proceedings of IEEE International Conference on Robotics and Automation*, pages 1993–1998, 1999.
- [63] Y. Shan and Y. Koren. Design and motion planning of a mechanical snake. *IEEE Trans. on Systems Man and Cybernetics*, 23(4):1091–1100, 1993.
- [64] A. Shapiro. Design and control of a planar spider robot. Master’s thesis, Technion - Israel Institute of Technology, Haifa Israel, October 1999.
- [65] A. Shapiro, E. Rimon, , and S. Shoval. Immobilization based control of spider robots in tunnels environments. *The International Journal of Robotics Research*, 20(3):209–227, March 2001.
- [66] A. Shapiro and E. Rimon. Pcg: A foothold selection algorithm for spider robot locomotion in 2d tunnels. In *IEEE Int. Conference on Robotics and Automation*, Taipei, Taiwan, September 2003.

- [67] A. Shapiro, E. Rimon, and J. W. Burdick. Passive force closure and its computation in compliant-rigid grasps. In *IEEE/RSJ Int. Conference on Intelligent Robots and Systems*, Maui, Hawaii, November 2001.
- [68] A. Shapiro, E. Rimon, and J. W. Burdick. Passive force closure and its computation in compliant-rigid grasps. Tech. report, <http://www.technion.ac.il/~robots>, July 2001.
- [69] A. Shapiro, E. Rimon, and S. Shoval. Immobilization based control of spider robots in tunnels environments. In *IEEE Int. Conference on Robotics and Automation*, Seoul, Korea, May 2001.
- [70] A. Shapiro, E. Rimon, and S. Shoval. Computation and experiments of passive force closure in compliant-rigid grasps. In *The 29th Israel Conference on Mechanical Engineering*, Haifa, Israel, May 2003.
- [71] S. Shoval, E. Rimon, and A. Shapira. Design of a spider robot for motion with quasistatic force constraints. In *IEEE Int. Conf. on Robotics and Automation*, pages 1377–1383, 1999.
- [72] N. Simaan and M. Shoham. Stiffness synthesis of a variable geometry planar robot. In *The 8th International Symposium on Advances in Robot Kinematics. Included in Advances In Robot Kinematics: Theory and Application*, J. Lenarcic and F. Thomas, Eds. Kluwer Academic, 2002.
- [73] T. J. Stone, D. S. Cook, and B. L. Luk. Robug iii - the design of an eight legged teleoperated walking and climbing robot for disordered hazardous environments. *Mechanical Incorporated Engineer*, 7(2):37–41, 1995.

-
- [74] O. Taussky. Positive definite matrices and their role in the study of the characteristic roots of general matrices. *Adv. Math.*, (2):175–186, 1968.
- [75] O. Taussky. The role of symmetric matrices in the study of general matrices. *Linear Algebra and Its Applications*, (2):147–153, 1972.
- [76] J. C. Trinkle. On the stability and instantaneous velocity of grasped frictionless objects. *IEEE Transactions on Robotics and Automation*, 8(5):560–572, Oct 1992.
- [77] K. van der Doel and D. K. Pai. Performance measures for locomotion robots. *J. of Robotic Systems*, 14(2):135–147, 1997.
- [78] K. Walton. The oblique compression of two elastic spheres. *J. Mech. Phys. Solids*, 26:139–150, 1978.
- [79] Y. Wei and B. Goodwine. Stratified motion planning on non-smooth domains with application to robotic legged locomotion and manipulation. In *IEEE Int. Conference on Robotics and Automation*, pages 3546–3551, 2002.
- [80] T. Yoshikawa. Passive and active closure by constraining mechanisms. *J. of Dynamic Systems, Measurement, and Control*, 121 (3-4):418–424, 1999.

תכן ובקרת רובוט עכביש אוטונומי
לתנועה במנהרות דו-ממדיות

אמיר שפירא

תכן ובקרת רובוט עכביש אוטונומי לתנועה במנהרות דו-ממדיות

חיבור על מחקר

לשם מילוי חלקי של הדרישות לקבלת תואר
דוקטור לפילוסופיה

אמיר שפירא

הוגש לסנט הטכניון — מכון טכנולוגי לישראל

אוקטובר 2003

חיפה

תשרי תשס"ד

חיבור על מחקר נעשה בהדרכת פרופסור אילון רימון
בפקולטה להנדסת מכונות

הכרת תודה

הנני אסיר תודה לפרופ' אילון רימון על עזרתו והנחייתו המסורה בכל שלבי המחקר. ברצוני להודות לפרופ' רימון על הידע הרב שהעניק לי ועל תמיכתו ועידודו במהלך השתלמותי.

ברצוני להודות לדוקטור שרגא שובל על עזרתו הרבה ועל עצותיו המועילות במהלך תכנון ובניית רובוט העכביש ובמהלך ביצוע הניסויים. ברצוני להודות לזיהר אור על אין-ספור שיחות ודיונים פוריים. תודה לזאב הרש-קוביץ מבית המלאכה בבנין אנרגיה על יצור והרכבת רובוט-העכביש. תודה לעובדי בית המלאכה בבנין ייצור על בניית מתקן הניסוי לניסויי האחיזות. לבסוף, תודה למשפחתי האהובה להורי דוד וסילבי, לאישתי חיה, ולבני אלעד אביחי ואוריאל על תמיכתם ועידודם לאורך כל הדרך.

אני מודה לטכניון ולקרן ע"ש סלים ורחל בנין, מפעל הסטיפנדיות לחינוך בע"מ, המגבית היהודית המאוחדת - הפדרציה, ניו יורק, המשרד הישראלי,

על התמיכה הכספית הנדיבה בהשתלמותי

העבודה מוקדשת להורי דוד וסילבי שפירא לאישתי חיה ולבני אלעד

אביחי ואוראל.

תוכן ענינים

1	תקציר באנגלית
2	רשימת סמלים
7	1 הקדמה
11	1.1 סיכום תרומות המחקר
14	2 קבוצת סגור הכוחות של אחיזות מבוקרות לינארית
14	2.1 הקדמה
16	2.2 הגדרה גיאומטרית של אחיזות בסגור כוחות
17	2.2.1 טרמינולוגיה של אחיזות המערבות מגע עם חיכוך
18	2.2.2 חזרה על אחיזות בסגור כוחות אקטיבי
19	2.2.3 סגור הכוחות באחיזות עם מגעים גמישים
22	2.3 סגור הכוחות של אחיזות עם אצבעות גמישות
22	2.3.1 איפיון של קבוצת סגור הכוחות
26	2.3.2 קבוצת סגור הכוחות בהנחת חוק גמישות לינארי
27	2.4 אנליזת יציבות גלובלית
27	2.4.1 נקודות שיווי המשקל של האובייקט האחוז
29	2.4.2 איפיון איזורי היציבות

38	אלגוריתם לבדיקת שיוך נקודה לאגן התכנסות	2.4.3
39	סגור הכוחות עבור אצבעות בעלות פרופיל כלשהו	2.5
40	תיאור הבעיה והצגה מתימטית שלה	2.5.1
44	נקודת שיווי המשקל המקורית כאשר מאפשרים גילגול	2.5.2
46	יציבות לגילגול של נקודת שיווי המשקל	2.5.3
49	תוצאות סימולציות וניסויים	2.6
49	מערכת הניסוי	2.6.1
50	ניסוי המאמת את קבוצת סגור הכוחות היציבה	2.6.2
55	ההשפעה של כוחות לחיצה התחלתיים שונים על היציבות	2.6.3
58	סיכום	2.7
60	PCG אלגוריתם לבחירת נקודות אחיזה	3
60	הקדמה	3.1
65	אחיזות תלת-רגליות חוקיות	3.2
70	הקמירות של קבוצת האחיזות התלת-רגליות החוקיות	3.3
70	הקמירות של קבוצת האחיזות החוקיות	3.3.1
72	קמירות של בעיית הקירוב ע"י קוביות	3.3.2
75	אלגוריתם PCG	3.4
83	בחירת מספר התיבות המקסימליות	3.5
83	קישוריות בין קבוצות קמורות	3.5.1
84	בחירת הקונפיגורציה היחסית של התיבות המקסימליות	3.5.2
85	אלגוריתם לבדיקת מספר התיבות המקסימליות	3.5.3
86	תוצאות סימולציה	3.6
88	סימולציה של אלגוריתם PCG	3.6.1
93	ההשפעה של מספר התיבות המקסימליות על אורך המסלול	3.6.2

95	סיכום	3.7
98	בקרה של רובוט עכביש	4
98	הקדמה	4.1
100	מודל מגע גמיש	4.2
103	מטריצת הקשיחות של המגע	4.2.1
107	חוק הבקרה	4.3
107	הדינמיקה של רובוט עכביש בעל k -גפיים	4.3.1
109	חוק הבקרה	4.3.2
110	נקודת שיווי משקל של מערכת רובוט העכביש	4.3.3
113	לינאריזציה של מערכת רובוט העכביש בנקודת שיווי-משקל	4.3.4
114	אנליזת יציבות	4.4
114	יציבות מערכות לינאריות אסימטריות	4.4.1
119	יציבות נקודת שיווי-משקל של רובוט-עכביש בעל k -גפיים	4.4.2
125	סיכום	4.5
127	תוצאות ניסויים	5
127	מערכת הניסוי	5.1
129	תוצאות הניסוי	5.2
136	סיכום ומסקנות	6
139	תוספות לאחיזות בסגור כוחות	א
139	תנאים לסגור כוחות עבור אחיזות עם מגעים גמישים	א.1
140	חישוב מטריצת הקשיחות של האחיזה	א.2
143	פרטי אלגוריתם PCG	ב

רשימת איורים

1.1	שני דורות של רובוט העכביש. (a) רובוט עכביש 4-רגלי המסוגל לנוע במ-נהרות ללא חיכוך, ו-(b) רובוט עכביש 3-רגלי המסוגל לנוע במנהרות עם חיכוך.	9
2.1	(a) יד מרובת אצבעות אוחזת אובייקט. (b) רובוט מרובה גפיים נאחז כנגד דפנות מנהרה.	15
2.2	סימונים בסיסיים לאחיזות המערבות מגעים עם חיכוך.	18
2.3	תרשים סכימטי של תנועת הגלגול בין אצבע i לאובייקט.	40
2.4	תרשים סכימטי של הכוחות הפועלים על אצבע i במהלך תנועת גילגול.	49
2.5	מערכת הניסוי לאחיזות דו-אצבעיות	50
2.6	מדידת קבועי הקפיצים. הנקודות הן המדידות בפועל, והקו הוא תוצאה של רגרסיה לינארית.	51
2.7	תרשים סכימטי של מהלך הניסוי המראה את כיווני הפעלת הכוחות על האובייקט.	52
2.8	(a) קבוצת הקונפיגורציות בהן האובייקט יציב ו-(b) וקבוצת סגור הכוחות היציבה עבור הניסוי הראשון.	52
2.9	הכוח המקסימלי הנמצא בקבוצת סגור הכוחות היציבה שניתן להפעיל על האובייקט בכל זווית של הפעלת הכוח. הקו מציין תוצאה אנליטית ואילו הנקודות נמדדו בניסוי.	53

- 2.10 הכוחות והמומנטים שהופעלו על האובייקט מוצגים במרחב הכוחות והמומנטים. 54
- 2.11 תרשים סכימטי של מערכת הניסוי המראה כיצד הופעל מומנט טהור על האובייקט האחוז. 55
- 2.12 המומנט החיצוני המקסימלי הניתן להפעלה על האובייקט מול כוח הל-חיצה ההתחלתי. הקו מתאר את המומנט המחושב והנקודות מתארות את המומנט שנמדד בניסוי. 56
- 2.13 קבוצת סגור הכוחות היציבה מוצגת במרחב הכוחות והמומנטים עבור כוחות לחיצה התחלתיים שונים. 57
- 3.1 מבט על של רובוט עכביש תלת-רגלי הנע בתוך מנהרה מישורית. 64
- 3.2 (a) רובוט תלת-רגלי במנהרה מישורית, ו-(b) ופרמטריזציה של מרחב קונ-פיגורציות המגע שלו. 66
- 3.3 (a) אחיזה תלת-רגלית חוקית, (b)-(c) המכילה שתי אחיזות דו-רגליות שונות. 68
- 3.4 הדיסק המינימלי המכיל את שלושת נקודות האחיזה כאשר Δ הוא (a) משולש חד-זווית, ו-(b) משולש כהה-זווית. 72
- 3.5 (a) שלוש תיבות במרחב קונפיגורציות המגע, ו-(b) וחלוקה הדדית שלהן ע"י המישורים המפרידים. 76
- 3.6 אילוסטרציה דו-מימדית המראה את ההשפעה של מספר התיבות המקסימ-ליות על אורך המסלול. 87
- 3.7 תנוחות שיווי-משקל דו-רגליות במישור (s_i, s_j) . 88
- 3.8 אוסף כל התנוחות התלת-רגליות החוקיות במרחב קונפיגורציות המגע. 89
- 3.9 קירוב באמצעות חמש תיבות של התנוחות התלת-רגליות החוקיות בתא $I_1 \times I_6 \times I_1$. 91
- 3.10 אוסף 270 התיבות המקסימליות המקרבות את התנוחות התלת-רגליות החוקיות. 91

3.11	המסלול הקצר ביותר מ-S ל-T לאורך קשתות גרף תת-התיבות במרחב
92	קונפיגורציות המגע.
3.12	המנהרה אשר שימשה לסימולציות, וסידרת נקודות האחיזה אשר יוצרה
94	ע"י אלגוריתם PCG
4.1	החדירה ההדדית בין כף הרגל של רובוט העכביש ודופן המנהרה.
4.2	הצגה סכמטית של הקשרים הגיאומטריים עבור תזוזות אינפיניטימליות
104	מהחדירה הנומינלית.
5.1	המנהרה ששימשה לניסוי, וסידרת נקודות האחיזה אשר יוצה ע"י אלגור-
130	יתם PCG.
5.2	המסלול הקצר ביותר מ-S ל-T לאורך קשתות גרף תת-התיבות במרחב
	קונפיגורציות המגע. בכל צומת (צעד) מסומנות נקודות האחיזה בצורה
131	(רגל 1, רגל 2, רגל 3).
5.3	תרשים המראה כיצד נוצר כוח קדימה ע"י כוחות המגע.
5.4	מדידות של פרמטרי הקונפיגורציה של הרובוט במהלך הניסוי. המסלול
134	הרצוי מסומן ע"י קו מקוקו והמדידות בפועל מתוארות ע"י קו רציף.
5.5	תמונות מסרט הוידאו המראה את רובוט-העכביש נע לאורך המנהרה.

תקציר

מזה זמן רב מפתחים בעולם מכונות הולכות. היתרון של מכונה הולכת על פני רכב גלגלי הנו בעיקר בתוואי שטח לא מובנה בו דרושה עבירות גבוהה. הבעיה המרכזית עמה מתמודדים מפתחי המכונות ההולכות היא כיצד לשמור על יציבות הרובוט במהלך התנועה. מטרת המחקר הנה פיתוח רובוט עכביש בעל גפיים לזחילה במנהרות. במחקר זה פותחה גישה ייחודית לפתרון הבעיה ע"י בחירת צורת הליכה בה הרובוט נאחז בשיווי-משקל כנגד דפנות המנהרה. בעבודה קודמת בנושא הנחנו כי דפנות המנהרה חלקות ונעזרנו בתיאורית הקיבוע של Rimon and Burdick לשם קביעת מספר הזרועות המינימלי הדרוש לרובוט, ולשם הוכחת יציבות האחיזה. אולם, ההנחה שדפנות המנהרה חלקות היא מחמירה מהסיבה הבאה. כאשר לא קיים חיכוך הרובוט לא יוכל להתקדם בתוך מנהרה בעלת גיאומטריה פשוטה במיוחד כמו למשל שתי דפנות מקבילות. מסיבה זו בחרנו בעבודה זו להניח כי דפנות המנהרה אינן חלקות, ולכן נוכל לנצל את כוחות החיכוך במגעיים לתועלת תנועת הרובוט. תנועת הרובוט נוצרת עקב כוחות הריאקציה שהסביבה מפעילה על הרובוט, ותכנון מסלול התנועה מותנה בכך שהרובוט יאחז עצמו בשיווי-משקל במהלך תנועתו. בצורת התנועה האמורה העכביש עדיין חופשי להניע את החוליות הפנימיות שלו. מטרת עבודה זו היא לכן פיתוח אלגוריתם תנועה ובקרה לרובוט עכביש מישורי הנע בסביבה של מנהרות. על הרובוט להיות בעל מספר גפיים מינימלי אשר עדיין יאפשרו לו התקדמות יציבה לאורך המנהרה תחת ההנחות הבאות. ראשית אנו מניחים כי כל רגל רשאית לגעת בסביבה רק באמצעות החוליה האחרונה שלה הנקראת כף הרגל. על כפות הרגליים לא

מותקנות כריות ואקום, והן רשאיות רק לדחוף כנגד הסביבה. שנית, הרובוט ינוע בתוך מנהרה מישורית דו-מימדית בעלת דפנות לינאריות למקוטעין.

היות ובחרנו צורת הליכה בה הרובוט נאחז בשיווי-משקל כנגד דפנות המנהרה אנו נדרשים בשלב ראשון לאפיין אחיזות שיווי-משקל. לכן נרצה לאפיין את תחום שיווי המש-קל של אובייקט האחוז ע"י מספר אצבעות כך שקיים חיכוך במגעים בין האצבעות לאובי-יקט. כאשר, אנו מעוניינים לאפיין את תחום שיווי המשקל הן במרחב קונפיגורציות האובי-יקט והן במרחב הכוחות והמומנט החיצוני המופעלים עליו. אולם, אנו מעוניינים לחקור רק אחיזות פסיביות בהן האובייקט נאחז בתחילה ע"י אצבעות בעלות קשיחות מסוימת. בהמשך מפעילים כוח ומומנט חיצוני על האובייקט אולם מערכת הבקרה לא מפעילה כוח נוסף ע"י האצבעות מעבר לכוח שנוצר עקב תזוזת נקודת המגע וקשיחות האצבע. במצב זה ובמידה שמטריצת הקשיחות של האחיזה הינה חיובית האובייקט יתכנס לנקודת שיווי משקל חדשה אותה איפיינו וכמו כן חישבנו את גבולות אגן ההתכנסות של אותה נקודת שיווי משקל. לשם איפיון נקודות שיווי המשקל השתמשנו בתיאוריית מורס. תוצאות אלו ישמשו בהמשך לקביעת התנאים ליציבות הרובוט הנאחז כנגד דפנות המנהרה.

בהמשך, פיתחנו אלגוריתם לבחירה אוטומטית של נקודות המגע על דפנות המנהרה. אלגוריתם זה מאפשר למצוא רצף של נקודות אחיזה העומדות בשני התנאים הבאים. התנאי הראשון הוא שנקודות האחיזה יצרו אחיזת שיווי-משקל. התנאי השני הוא שה-נקודות יהיו בתוך טווח ההגעה של הרובוט. תכנון רצף נקודות האחיזה מתבצע במרחב קונפיגורציות המגע. באמצעות שיטות תכנות קמורות מתבצע קירוב של האיזורים המותרים במרחב קונפיגורציות המגע בעזרת תיבות. לאחר מכן מתבצעת חלוקה הדרגתית של התיבות המשרה מבנה נתונים של גרף בו כל תת-תיבה היא צומת ואם ניתן לעבור מתת-תיבה אחת לשנייה אז קיימת קשת. לבסוף מתבצע חיפוש של מסלול קצר ביותר בגרף למציאת רצף של נקודות אחיזה לאורך המנהרה.

נדון כעת בבעיית הבקרה של הרובוט. לעכביש k זרועות אשר לכל אחת מהן n דרגות חופש ממונעות. הגוף-המרכזי מוסיף שלוש דרגות חופש נוספות. כלומר לעכביש יש בסך

הכל $kn + 3$ דרגות חופש, מתוכן רק kn ממונעות. אולם, העכביש אינו מערכת תת-ממונעת. זאת משום שכאשר העכביש נאחז כנגד דפנות המנהרה הזרועות האוחזות כנגד הדפנות מציבות אילוצים קינמטיים אשר למעשה מאלצים את העכביש לנוע ביריעה שממדה קטן מ- kn בעיית הבקרה היא אילו מומנטים יש להפעיל ב- kn מנועי העכביש על מנת להביא את כל $kn + 3$ משתני הקונפיגורציה של העכביש אל המיקום הדרוש כך שבסיום התנועה העכביש ימצא שוב על היריעה. בפרט אנו מעוניינים ליצור כוחות ומומנטים מושרים על הגוף-המרכזי על מנת להביא אותו אל המיקום והאוריינטציה הרצויים.

שיטת הבקרה אותה ישמנו מתבססת על אחיזת העכביש בשיווי-משקל יציב ע"י דפנות המנהרה. כאשר כפות-רגלי העכביש נשארות בתנוחה בה מושגת אחיזת שיווי-משקל יציבה של העכביש ביחס לסביבתו, כוחות הריאקציה הנוצרים עקב הגמישות הטבעית של החומרים ועקב כוחות החיכוך במגעם יפעלו כדי לייצב את המכניזם כגוף-קשיח אחד. לכן שיטת הבקרה אותה יישמנו מתבססת על הרכיבים האקטיביים והפסיביים הבאים. הרכיב האקטיבי הוא הנעה של מפרקי הרובוט הממונעים בצורה המבטיחה כי כפות הרגליים האוחזות תשארנה נייחות אחת ביחס לשנייה. בצורה זו מנקודת המבט של המנהרה העכביש מתנהג כגוף-קשיח אחד במשך כל התנועה. נציין כי למרות דרישה זו אנו עדיין חופשיים להניע את הגוף-המרכזי ואת הרגל החופשית לאורך כל מסלול תנועה רצוי, כאשר התנאי היחידי על מסלול התנועה הוא שכפות הרגליים האוחזות תשארנה נייחות אחת ביחס לשנייה. הרכיב הפסיבי של הבקרה מסתמך על כוחות הריאקציה הנוצרים ע"י דפנות המנהרה. כוחות אלו פועלים על כפות-הרגליים האוחזות על מנת להשאיר את העכביש כגוף-קשיח אחד באותו מיקום ואוריינטציה. במילים אחרות, דפנות המנהרה וכוחות החיכוך בנקודות המגע יבטלו אוטומטית כל כוח אינרציאלי מספיק קטן הנוצר ע"י החלקים הנעים של העכביש. בסיום התנועה כאשר הרגל החופשית תגיע ליעדה הכוחות האינרציאליים אשר נבעו מתנועתה יתאפסו, וכפות-הרגליים האוחזות תתיצבנה בדיוק במיקומן ההתחלתי.

לאחר שיש בידינו את חוק הבקרה של הרובוט נבחן את יציבות מערכת החוג הסגור

סביב נקודת שיווי המשקל של העכביש. בשלב זה אנו ממדלים את כוחות המגע ע"י מודל מגע גמיש הנותן קשר ישיר בין כוח המגע לבין תזוזת נקודת המגע. קשר זה מתאפיין ע"י מטריצת קשיחות אותה פיתחנו. מטריצה זו מתאפיינת בכך שהיא אינה סימטרית. בנוסף מצאנו תנאי המביא לכך שהחלק הסימטרי של מטריצת הקשיחות של המגע יהיה חיובי. אסימטריות זו גורמת לכך שגם הלינאריות של מערכת החוג-הסגור של העכביש היא לא סימטרית. לכן כדי לבחון את יציבות הרובוט בסביבת נקודת שיווי-משקל פיתחנו תיאוריה חדשה לבחינת יציבות מערכות אסימטריות לינאריות מסדר שני. תיאוריה זו מתבססת על ההשערה שכאשר נבחן מערכת סימטרית יציבה ולאחר מכן נוסיף לה "מעט" אסימטריות זה לא אמור לפגום ביציבות הכוללת של המערכת. על בסיס השערה זו פיתחנו (והוכחנו את נכונותה אנליטית) חסם עליון על כמות אי-הסימטריות אשר ניתן להוסיף למערכת מבלי לפגוע ביציבותה.

לסיום, הדגמנו בפועל את יישום התאוריות שפותחו באמצעות ניסויים. ניסויים אלו בוצעו באמצעות הדור השני של רובוט העכביש אשר פותח במעבדתנו. רובוט זה הינו רובוט עכביש מישורי תלת-רגלי ההולך בתוך מנהרה זו מימדית. הניסויים מסתכמים בסרט ווידאו, אשר ניתן להורידו מאתר המעבדה לניווט רובוטים, המראה תנועה שלמה של הרובוט מתחילת המנהרה ועד סופה. במהלך תנועה זו הרובוט מבוקר באמצעות שיטת הבקרה שפיתחנו ובוחר את נקודות האחיזה באמצעות אלגוריתם PCG.